# Physical and Biological Processes at the Middle Atlantic Bight Shelf-Break Front

by

Andrew Joseph Hirzel

B.S., University of Miami, 2013

Submitted to the Department of Earth, Atmospheric, and Planetary Sciences in partial fulfillment of the requirements for the degree of

Doctor of Philosophy

at the

MASSACHUSETTS INSTITUTE OF TECHNOLOGY

and the

WOODS HOLE OCEANOGRAPHIC INSTITUTION

February 2023



Author . . . . . .

Joint Program in Oceanography, Applied Ocean Science & Engineering
Massachusetts Institute of Technology
& Woods Hole Oceanographic Institution
January 11, 2023

Certified by . . . . . .

Dr. Dennis J. McGillicuddy, Jr.
Senior Scientist, Applied Ocean Physics & Engineering
Woods Hole Oceanographic Institution
Thesis Supervisor

Accepted by . . . . . .

Dr. Jesús G. Pineda
Chair, Joint Committee for Biological Oceanography
Woods Hole Oceanographic Institution

# Physical and Biological Processes at the Middle Atlantic Bight Shelf-Break Front

by

Andrew Joseph Hirzel

Submitted to the Department of Earth, Atmospheric, and Planetary Sciences
on January 11, 2023, in partial fulfillment of the requirements for the degree of
Doctor of Philosophy

## Abstract

The Middle Atlantic Bight (MAB) is a highly productive ecosystem, supporting several economically important commercial fisheries. Chlorophyll enhancement at the MAB shelf-break front has been observed only intermittently, despite numerous studies that suggest persistent upwelling at the front. High resolution cross-frontal transect crossings were collected from three two-week cruises in April 2018, May 2019, and July 2019. Chapter 2 focused on applying a novel method of classifying planktonic images taken by a Video Plankton Recorder to enable processing of the large volumes of data collected with the instrument. Chapter 3 investigated cross-frontal trends by temporally averaging in both Eulerian and frontally-aligned coordinates. For April 2018, transient chlorophyll enhancement was seen at the front in individual transects and within the frontally-aligned mean transect, but not within the Eulerian mean transect. The Eulerian mean for May 2019 showed chlorophyll enhancement as a result of frontal eddies, which were further explored in chapter 4. No frontal enhancement was observed in July 2019. The frontal eddies observed in May 2019 were simulated using an idealized model, which showed that upwelling occurred within both of the frontal eddies, despite having opposite rotational directions. This result was consistent with nutrient enhancement observed within the centers of both eddies. Biological enhancement within each eddy was observed, which may have been a result of advection from source waters and/or a local response to upwelled nutrients. The influence of frontal variability and frontal eddies on nutrients and plankton at the front argues for the necessity for 3-D models to fully explain frontal behavior and its effects on biological responses.

Thesis Supervisor: Dr. Dennis J. McGillicuddy, Jr.
Title: Senior Scientist, Applied Ocean Physics & Engineering
Woods Hole Oceanographic Institution

## Acknowledgements

Science is a collaborative effort – and so too did many people contribute to this thesis. Above all others, thank you to Dennis McGillicuddy for being my adviser. You have been indispensable in every step of my thesis and always encourage me to strive for excellence. Thank you to Heidi Sosik and Weifeng (Gordon) Zhang as well for all of your aid throughout my chapters. I have been extraordinarily lucky to work closely with all three of you.

Thank you to Team VPR for making me feel welcome, especially Philip Alatalo and Hilde Oliver. You all have been nothing but helpful, on land and at sea.

This work was completed as part of the Shelfbreak Productivity Interdisciplinary Research Operation at the Pioneer Array (SPIROPA) project, and I thank all of you for your aid over the years. I am grateful for your positivity and support. Operation of the Pioneer Array by the National Science Foundation's Ocean Observatories Initiative is also greatly appreciated.

Last but certainly not least, thank you to my family and friends, both local and distant. Your kind thoughts and actions never cease to warm my heart.

The research in this thesis was supported by the National Science Foundation (OCE-1657803) and the Dalio Foundation. Support from the WHOI Academic Programs Office is gratefully acknowledged.

# Table of Contents

# List of Figures

## Chapter 2



## Chapter 3

## Chapter 4



# List of Tables

# Chapter 1

## Introduction

Located in the Northwest Atlantic, the Middle Atlantic Bight shelf-break front separates two water masses: cold, fresh continental shelf water inshore and warm, salty Slope Sea water offshore. Elevated chlorophyll levels have been detected at the front using remote sensing (e.g., Ryan *et al.*, 1999a) and *in situ* observations (e.g., Marra *et al.*, 1990), reflecting a highly productive shelf-break region (Marra *et al.*, 1990; Ryan *et al.*, 1999b). There are a variety of processes that can enhance chlorophyll at the front. When nutrients are in abundance in the early spring, Ekman re-stratification can relieve light limitation in phytoplankton, causing enhancement of chlorophyll at the front (Oliver *et al.,* 2022). At other times of year, when nutrients are depleted in the euphotic zone, chlorophyll enhancement can potentially result from several mechanisms of upwelling at the front. Multiple upwelling mechanisms can potentially support frontal chlorophyll enhancement, including bottom boundary layer convergence and detachment (e.g., Gawarkiewicz and Chapman, 1992; Houghton and Visbeck, 1998; Houghton *et al.,* 2006), upwelling of waters from the offshore interior (Zhang *et al*., 2011), and upwelling driven by instabilities within the shelf-break front (Zhang and Gawarkiewicz*,* 2015). Upwelling provided by these mechanisms ranges from tens of cm $d^{-1}$ (Zhang *et al*., 2011) to tens of m $d^{-1}$ (Zhang and Gawarkiewicz*,* 2015) depending on the mechanism.

Despite evidence for the co-occurrence of chlorophyll enhancement and upwelling at the shelf-break front, the relationship between the two is poorly understood, increasing the difficulty of estimating productivity of this region. A 2-D model by Zhang *et al.* (2013) suggested that upwelling may not result in a substantial increase in chlorophyll at the front because of increased grazing by zooplankton. In an *in situ* study, Hales *et al.* (2009b) observed evidence of upwelling

without a substantial increase in phytoplankton at the base of the euphotic zone. Measured nutrient and light levels should have been sufficient to enhance phytoplankton and there was no evidence of an increase in zooplankton grazers to account for the lack of a phytoplankton enhancement, making these findings difficult to reconcile with models.

The high variability associated with the shelf-break front may also obfuscate trends of chlorophyll enhancement. The dynamics of the frontal region have been described by multiple climatologies (Linder and Gawarkiewicz, 1998; Loder *et al.*, 2001; Zhang *et al.*, 2011), all of which show that the physical, biological, and chemical attributes of the shelf-break front vary significantly in both time and space. These variabilities can be partially attributed to the plethora of both internal and external forcings acting upon the shelf-break front, ranging from frontal meanders (Pickart, 1999) and frontally generated submesoscale eddies (Gawarkiewicz *et al.*, 2001) to Gulf Stream warm core rings (Ryan *et al*., 2001) and, in rare instances, meanders of the Gulf Stream (Gawarkiewicz *et al.*, 2018). Averaged satellite chlorophyll measurements show highly variable distributions between years (Saba *et al*., 2015), at least partially due to the variability at the shelf-break front.

This thesis aims to use a combination of high-resolution cross-frontal surveys, satellite imagery, and model output to explore the impact of the MAB shelf-break front on planktonic communities. *In situ* observations were collected over the course of three cruises, during which a cross-frontal transect was sampled repeatedly. As part of this observational activity, two Video Plankton Recorders (VPRs) were used to quantify mesoplankton abundance. These VPRs substantially increased the spatial and temporal resolution of frontal surveys compared to previous studies. The plethora of VPR images required a novel method for analysis. Chapter 2 describes adaption of a convolutional neural network for classifying VPR images, which was

then applied in successive chapters. Chapter 3 combines data from all three cruises and satellite measurements to investigate plankton distributions at the shelf-break front. These cruises spanned the months of April 2018, May 2019, and July 2019, representing a unique opportunity to observe two springtime periods and one summertime period – contrasting seasonal and interannual variability. We then investigate how our results relate to the earlier hypotheses raised regarding transient frontal enhancement. Chapter 4 describes in greater detail the impact of two frontal eddies seen in May 2019 on planktonic distributions. Both eddies appeared to contain upwelling and potential biological response *in situ*, while rotating opposite directions. These results are further explored using an idealized 3D model of the frontal region. In sum, these chapters serve to further our understanding of how the shelf-break front impacts biological communities.

# Chapter 2

# Quantitative Imaging: Convolutional Neural Networks and the Video Plankton Recorder

## 2.0 Abstract

Modern imaging technology has enabled increasingly ambitious efforts to quantify planktonic populations. However, this has led to an additional problem: how can the resulting data be efficiently processed? This study presents a novel application of a Convolutional Neural Network (CNN) architecture to one such instrument, the Video Plankton Recorder (VPR). The VPR is towed behind a vessel at 10 knots, during which it completes an undulation from the surface to a depth of 100m every few kilometers. Physical parameters and video frames are collected concurrently, with up to 30 video frames captured each second. Regions Of Interest (ROIs) are then selected from each video frame based on edge detection and brightness. In water with high planktonic abundance, such as the Middle Atlantic Bight, this can result in such a large number of ROIs that manual classification is not feasible. During a single cruise (TN368), 3 million ROIs were collected within a two-week period. A subset of roughly 20 thousand ROIs spanning 31 categories were manually classified and then used to train three CNN instances, with approximately 90% overall accuracy. The resulting CNN classifiers were then applied to the entire dataset. A subset of classified ROIs was manually inspected to assess the performance of the CNN, correctly estimating one diatom category and underestimating three others. All four diatom categories showed clear geographic variations that matched physical parameters.

## 2.1 Introduction

Video Plankton Recorders (VPR) have combined in situ planktonic imaging with physical and bio-optical sensor data for the past 30 years (Davis *et al.,* 1992). Individual VPRs have been deployed around the world, such as Georges Bank (Norrbin *et al.,* 1996), the North Atlantic (Davis and McGillicuddy, 2006), Norwegian fjords (Basedow *et al.,* 2013), the Ross Sea (Smith *et al.,* 2017), and the Middle Atlantic Bight (Oliver *et al.,* 2021). As a towed instrument, the VPR can be used to quickly sample the upper ocean at high vertical and horizontal resolution (e.g., Davis *et al.,* 1992). However, this high sampling ability comes with a challenge: millions of planktonic images may be collected over the course of a single cruise. How can this data be efficiently processed?

Early VPR images were automatically classified using Support Vector Machines and co-occurrence matrices, yielding accuracies of around 70% for seven input taxa (Hu and Davis, 2005). Computing hardware advances, particularly in parallel graphics processing unit (GPU) based processors, have instead shifted classification techniques towards deeper Convolutional Neural Networks (CNNs) (Krizhevsky *et al.,* 2012; Lumini and Nanni, 2019). CNNs are now widely used to automatically classify planktonic images with both greater accuracy and greater taxonomic diversity (e.g., Bochinski *et al.,* 2018; Cheng *et al.,* 2019; González *et al.,* 2019; Lee *et al.,* 2016; Luo *et al.,* 2018). This study investigates the use of a CNN to process VPR data collected south of the Middle Atlantic Bight shelf-break front. This dataset encompasses a number of challenges ideal for evaluating CNN-based classification: over 3 million object-containing images were collected during the two-week cruise and sampling revealed intermittent diatom hotspots of high ecological interest. Diatom concentrations were highly variable spatially,

inconsistently overlapping with intense patches of marine snow that impacted image quality throughout the cruise, further increasing the complexity of the dataset.

Related CNN architectures as used in this study have been tested previously using Imaging FlowCytobot (IFCB) planktonic images (Orenstein *et al.,* 2015; González *et al*., 2019). However, the IFCB is an imaging-in-flow cytometer, while the VPR images objects undisturbed in the water column. This difference in instrumental design yields several key differences in images obtained by each instrument. In imaging-in-flow cytometers, including the IFCB, particles are imaged as they pass through a flow cell. Hydrodynamic focusing and optical geometry are configured to ensure that individual targets are in the focal plane for imaging (Olson and Sosik, 2007). This approach has advantages for image quality and consistency, but the flow cell geometry constrains the maximum particle size (~150 μm) and sample throughput. In comparison, the VPR images objects directly in the water column, imaging objects 100 μm – 1 cm at a rate of approximately 0.5 L $s^{-1}$ (Davis *et al.,* 2005). Objects are imaged as full field of view video frames and then identified and separated in post-processing. The distance between an object and the camera is not fixed with the VPR, nor are objects guaranteed to be fully within the field of view when imaged. This permits individual objects to be out of focus, to be fractionally imaged, or to overlap and obscure other objects. These challenges are particularly well represented within a diatom bloom, where diatom chains are of sufficient density to cover entire video frames making conventional image analysis difficult to impossible.

The objective of this paper is threefold: to utilize CNN architecture to classify VPR data, to test a new method for more precise bloom quantification, and to obtain realistic and precise geographical distributions of the target diatom hotspots. Together, these objectives will provide a new framework for processing previously challenging VPR datasets.

## 2.2 Materials and procedures

*2.2.1 Image collection*

Images were collected aboard R/V Thomas G. Thompson cruise TN368 (July 6-19, 2019). VPR deployments occurred roughly 200 km south of Massachusetts, US, repeatedly traversing the shelf-break front. Two VPRs were used in this study: the Digital Autonomous Video Plankton Recorder (DAVPR, from SeaScan Inc.) and the Video Plankton Recorder II (VPRII, from SeaScan Inc.) (Figure 2.1). The DAVPR was attached to a CTD rosette and includes a Seabird Electronics Inc. CTD (SBE 49 FastCat), fluorometer (FLNTURTD-4620), and synchronized video camera and xenon strobe (Davis *et al.,* 2004). The VPRII consists of a towed body, containing a Seabird Electronics Inc. CTD (SBE 49 FastCat), oxygen sensor (SBE 43), fluorometer (ECO FLNTU-4050), ECO Triplet (ECO BBFL2-123), PAR (photosynthetically active radiation; Biospherical Instruments Inc. QCP-200L), and synchronized video camera and xenon strobe (Davis *et al.,* 2005). The VPRII was towed at 10 knots (5.1 m $s^{-1}$), undulating between depths of 5m and 100m approximately every 6 minutes. Plankton video for the DAVPR and VPRII was recorded at 20 Hz and 30 Hz respectively. DAVPR video frame dimensions were 1392 x 1040 pixels (~10 x 7 x 25 mm volume imaged) and VPRII video frame dimensions were 1380 x 1034 pixels (~20 mm x 15mm x 23 mm volume imaged). Individual video frames from both instruments were passed through object identification software to identify "regions of interest" (ROIs), which were then saved to disk with a time-stamp naming convention (Davis *et al.,* 2004). Approximately 140,000 DAVPR ROIs and 3,700,000 VPRII ROIs were collected during this cruise.

*2.2.2 CNN training set*

All DAVPR ROIs were manually annotated to construct the CNN training set. Annotated ROIs were vetted based on image quality before addition to the training set. A maximum of 5,000 ROIs and a minimum of 20 ROIs were used to create each category. 20,102 ROIs total were used in the training set, representing a total of 31 morphologically distinct categories. Diatom abundance within diatom hotspots were of sufficient density to cause bloom ROIs to be visually distinct from non-bloom ROIs, so two diatom bloom composite categories were added to the training set (Figure 2.1). Both of these categories represent ROIs that contained more than one diatom chain within the same ROI. “Diatom bloom without marine snow” is a composite category containing ROIs with multiple diatom rods and/or diatom coils. “Diatom bloom with marine snow” contains marine snow and a mixture of diatom rods and/or diatom coils. Training set ROIs for both composite categories were specifically chosen when diatom rods and coils were most abundant to test whether the CNN architecture used could correctly distinguish between bloom and non-bloom conditions. ROI classifications were all unique.

*2.2.3 CNN overview*

The CNN architecture chosen uses Inception v3 (Szegedy et al., 2016) as its core framework. In addition to the IFCB, similar Inception v3 based CNN architectures have also been successfully applied to other instruments, such as the Plankton Camera (Campbell *et al*., 2020) and HoloSea (MacNeil *et al*., 2021). Briefly explained, the base architecture of Inception v3 was originally trained on over a million images from the ImageNet database. Our training set was input into the supplied architecture to tailor the broad classification solution to our specific dataset. ROIs were first resized to 299 x 299 grayscale pixels to meet Inception v3 input criteria,

with ROI aspect ratio maintained and blank edge space filled with the average pixel value of all pixels in randomly selected ROIs. Twenty percent of training set ROIs were randomly chosen and removed prior to training for later validation purposes. The withheld ROIs were not used for creating a classifier. CNN classifiers are created by passing the remaining training set ROIs through a series of repeating layers. Feature identification occurs in 'convolutional layers', during which input data are convolved using convolutional filters. In parallel to later convolution layers are 'pool layers', which subsample created feature maps to reduce overfitting. After each set of convolution and pooling layers, feature maps are concatenated, after which feature extraction repeats. Shallower layers of the CNN identify features roughly equivalent to edge and contour detection, while deeper layers contain features such as shapes. These deeper layers achieve increased complexity by combining features identified on earlier layers to be more pertinent to the input training set. Earlier features may also be discarded if deemed no longer relevant, such as if a deeper layer causes the shallower layer to be redundant. At the end, all concatenated feature maps are merged in a 'fully connected layer'. This final layer is then used to generate a classifier.

This entire process was repeated over multiple iterations to yield multiple individual classifiers using the same original training set. These classifiers differed from each other based on information from the previous classifier being used to help create the following classifier, as well as due to stochastic elements. Stochasticity was introduced by randomizing the order in which training ROIs were presented within each iteration, as well as whether a given ROI was flipped along its x or y axis. ROIs were flipped to increase ROI variation within a category. Although training of the CNN classifier has a stochastic element, classification results for each classifier are deterministic.

The best iteration was determined by minimizing cross-entropy loss. Cross-entropy loss quantifies the logistic likelihood of whether input ROIs will be classified as one category or another. The cross-entropy loss was calculated using withheld training ROIs. Loss initially decreased with additional iterations, as classifiers learned to distinguish categories. Cross-entropy loss of withheld ROIs later increased as classifiers overfit to the training set. Choosing the iteration of minimum loss yielded the most accurate classifier while still preventing overfitting. Iterations were created for half again as many iterations as the present best iteration to ensure the minimum loss had been reached, with a minimum of 14 total iterations. The best iteration after both criteria were met was the final output classifier. One output classifier was created for each instance of training, for a total of three output classifiers used in this study. Each instance had independent stochastic elements, resulting in different final output classifiers between instances. All instances were created from identical training sets and withheld identical ROIs for validation.

*2.2.4 ROI annotation using a threshold*

ROI classifications were returned as the probabilities of a given ROI lying within each category. Ideally, a single category for a ROI had a drastically higher probability than all others, which would then make it simple to classify that ROI as the category with the highest probability. However, sometimes a given ROI had several categories with relatively high probabilities and no clear primary categorical classification. Imposing a probability threshold, a cutoff that a category probability must surpass to be classified as that category, has been shown to improve classifier accuracy by eliminating these cases (e.g., Brownlee *et al*., 2016; Luo *et al.,* 2018). For our study, a ROI whose highest probability category failed to surpass the target

threshold was placed in a category named ‘unknown’. As such, a threshold value of zero would classify every ROI as the category with the highest probability and the unknown category would be empty. Setting the threshold higher ensures that there are fewer false positives at the expense of having more false negatives. In order to minimize false positives and negatives, the threshold was determined by using linear regressions to compare CNN ROI classifications to their manually annotated classifications. This was done for both withheld training ROIs and a subset of VPRII ROIs (described below). Thresholds were tested from 0 to 100%, in intervals of 5%.

### *2.2.5 CNN evaluation with manually annotated VPRII ROIs*

Each CNN instance was run on manually annotated VPRII ROIs to evaluate accuracy and select the threshold described above in relation to the targeted diatom hotspots. Forty time intervals were selected throughout the cruise to represent areas of varying diatom abundance, including both diatom hotspots and areas with few diatoms. Two hundred ROIs were manually annotated for each time interval, for a total of 8,000 ROIs. ROIs were selected so that they were representative of all common categories. These ROIs spanned all levels of quality and focus, including completely out of focus ROIs.

## 2.3 Assessment

### *2.3.1 Evaluation based on withheld training set ROIs*

Withheld training ROIs were insensitive to changing threshold value for most categories (4 diatom categories: Supplemental Figure 2.1). The highest probability category for the majority of ROIs had a value of over 0.9, and so classification results were mostly unaffected by changes to the threshold value below 0.9. As such, an arbitrary threshold criterion of 0.5 was used for all

categories. This value was chosen so that the most likely category had a majority of the overall probability for a ROI (>50%) rather than just a plurality. Approximately 3% of withheld ROIs were classified as unknown using a threshold of 0.5 compared to zero ROIs classified as unknown using a threshold of 0.

All three CNN instances performed well on withheld training ROIs, as evidenced by the predominance of the diagonal of the confusion matrix (Figure 2.2), which reflects the true positive rates (TPRs) for each category (TPR = true positive / (true positive + false negative). Marine snow, out-of-focus, and diatom coils had consistently high TPRs of >90% for all instances. TPR varied predominantly based on number of training ROIs, with categories with over 1,000 training set ROIs and between 200 and 1,000 training set ROIs having TPRs mostly above 80% and 60%, respectively. The range of TPRs among the three classifier instances was small for categories with over 200 training set ROIs. Categories with less than 200 training set ROIs showed much larger uncertainty between instances, with TPRs between instances within a category performing anywhere from roughly equal to significantly worse than that of categories with more training ROIs (e.g., Decapod Larvae TPR, 1: 20%, 2: 60%, 3: 80%). These trends are expected, as larger categories with more training ROIs provide a better representation of the category-specific variability that can be captured in 2-D imagery (e.g., morphology, orientation, etc.) and thus have lower uncertainty compared to categories with fewer training ROIs. Introduction of a threshold did not appear to affect the relationship between category training ROI number and uncertainty when compared to the results with a threshold of zero (Supplemental Figure 2.2). Categories with more training ROIs were less affected by the introduction of a threshold than those with fewer training ROIs.

Instance accuracy was measured using $F_1$ score ($F_1$=2*(precision*recall) / (precision + recall); precision = true positive / (true positive + false positive); recall = true positive / (true positive + false negative)). Overall instance accuracy was determined by taking the weighted average $F_1$ scores of all categories in an instance, with weighting being determined by the number of training ROIs within a category. This was done to limit variability introduced by minor categories. The weighted $F_1$ scores for each instance were similar (1: 89.93%, 2: 91.11%, 3: 89.80%), indicating that all three instances were comparable overall. Individual $F_1$ scores (Figure 2.3) mirrored the trends in TPR discussed above, with increasing $F_1$ with increasing number of training ROIs within a category. Most categories with over 200 training set ROIs had $F_1$ scores above 80%. Lowering the threshold from 0.5 to 0 lowered the overall weighted $F_1$ scores for each classifier (1: 88.69%, 2: 90.02%, 3: 88.88%) by approximately 1%.

Diatom categories were of particular interest in this study, given their importance to the planktonic ecosystem in this region and diatom hotspots in our dataset. The accuracies of diatom classifications were roughly comparable to other categories with approximately the same number of input training ROIs, with diatom rods and coils being comparable to categories with over 1,000 training ROIs and both bloom categories being comparable to categories with between 200 and 1,000 training ROIs. Diatom rods and coils both performed better than the diatom bloom composite categories (Figure 2.4). Diatom concentration estimates for diatom rods and diatom coils were both roughly within ±10% of the true concentration, with both diatom bloom categories predicted to underestimate or overestimate their true concentrations by up to 40%. All four diatom categories were mostly true positive, excepting instance 1 of diatom bloom without marine snow, which contained false positives from other diatom categories.

*2.3.2 Evaluation based on independent data*

Manually annotated VPRII ROIs showed greater sensitivity to threshold value than withheld training ROIs (4 diatom categories: Figure 2.5). Most categories had constant $R^2$ values for threshold values less than 0.6 and declining $R^2$ values at threshold values higher than 0.6. Diatom coils and diatom bloom without marine snow showed this pattern, while diatom rods were more similar to withheld training ROI categories with constant $R^2$ values below 0.9. Diatom bloom with marine snow $R^2$ values dropped from around 0.5 across threshold values for withheld ROIs to $R^2$ values of near zero using VPRII ROIs. Since $R^2$ values for a threshold value of 0.5 were unaffected and no more optimal threshold value presented itself, we chose to continue using a threshold value of 0.5. Classification as unknown increased compared to withheld ROIs (1: 19%, 2: 8%, 3: 15%).

TPRs of all categories were lower for manually annotated VPRII ROIs (Figure 2.6) compared to that of withheld training ROIs. Diatom rods and out-of-focus were the only categories with TPRs above 60% for all instances. For most categories, out-of-focus and unknown combined make up over 50% of total ROI classification. The next most common source of false negatives was marine snow. Diatom rods were the only diatom category predicted to be roughly similar to the true concentration (Figure 2.7), overestimating by approximately 15-35%. The other three diatom categories were predicted to underestimate concentrations (30% or less of true concentrations). Both bloom categories fared worse than diatom coils, with each having at least one instance with final concentrations predicted to be an order of magnitude smaller than the true concentration. For both diatom rods and diatom coils, the percentages of overestimation converged with increasing numbers of manually annotated ROIs available at the

time points of evaluation (Supplemental Figure 2.3). Diatom bloom categories showed greater variation and did not appear to converge with increased number of manually annotated ROIs.

Spatial patterns in CNN classified VPRII ROIs reflected salinity and chlorophyll measurements (Figure 2.8) with no major qualitative differences in distribution between instances (Supplemental Figure 2.4). Peak concentrations differed only slightly for diatom rods (Instance 1=8505 $L^{-1}$, 2=9419 $L^{-1}$, 3=10192 $L^{-1}$), with greater variation for diatom coils (Instance 1=913 $L^{-1}$, 2=1665 $L^{-1}$, 3=1622 $L^{-1}$), diatom bloom without marine snow (Instance 1=4580 $L^{-1}$, 2=821 $L^{-1}$, 3=3395 $L^{-1}$), and diatom bloom with marine snow (Instance 1=946 $L^{-1}$, 2=1665 $L^{-1}$, 3=291 $L^{-1}$). These differences among categories and CNN instances are consistent with the TPR results discussed above (Figure 2.7). Diatom distributions matched with regions of high chlorophyll, with diatom bloom categories having narrower peaks in the center of peak chlorophyll concentrations. This was expected to occur since diatom bloom conditions should only be present at regions of sufficiently dense diatom concentrations.

## 2.4 Discussion

This paper used the same dataset as that of Oliver *et al.* (2021), which presents a formation mechanism for the diatom hotspots discussed herein. VPR results are discussed in Oliver *et al*. (2021) only in terms of 'relative abundance' due to the challenges with quantitative analysis in these complex waters. Oliver *et al.* (2021) focused their discussion solely on the abundant diatom rod category. In this study, we have demonstrated a more quantitative analysis across multiple categories. The geographical distribution of diatom rods presented in Oliver *et al.* (2021) have been confirmed by our results above. Additionally, the diatom bloom categories identified regions of exceptionally high diatom abundance more accurately than using peak

diatom rod concentrations. This increased accuracy was true even with our underestimation of true diatom bloom abundance.

Enumeration of precise diatom abundance within diatom hotspots remains difficult. Concentrations within this paper are more precisely shown as ROIs per liter, rather than number of diatoms per liter. For non-bloom categories, such as diatom rods and coils, there typically was only one diatom chain within a ROI, such that ROIs $L^{-1} \approx$ diatom chains $L^{-1}$. Diatom bloom ROIs by definition had more than one diatom chain per ROI, ranging from 2 to several dozen. The absolute diatom concentration can be defined as the sum of individual diatom rods and coils plus those within bloom categories. This concentration could then be estimated with our results by computing the average number of individual diatom rods and coils within bloom ROIs and then multiplying all bloom ROIs by this scalar. A similar approach has been applied to colonies of *Phaeocystis antarctica* in the Ross Sea (Smith *et al.,* 2017) and *Phaeocystis pouchetti* on the New England Continental Shelf (Smith *et al.,* 2021).

Overall, internal CNN classifier accuracy assessed on withheld ROIs improved compared to previous VPR methodologies (e.g., Hu and Davis, 2005) and was comparable to the current accuracies of similarly sized training sets (e.g., Bochinski *et al,* 2019; Campbell *et al.,* 2020; MacNeil *et al.* 2021). Our threshold value was low compared to previous studies, 0.5 compared to greater than 0.7 (Brownlee *et al*., 2016; Campbell *et al*., 2020; Luo *et al*., 2018). However, each of these studies reported roughly 20% of images discarded by their respective threshold values, which roughly matches the number of ROIs classified as unknown for VPRII ROIs. Accuracy of VPRII ROIs was worse than that of withheld ROIs, with most misclassified ROIs being instead classified as out of focus. This was possibly caused by a lack of VPRII ROIs, especially VPRII out of focus ROIs, within the training set. Future work will include VPRII

ROIs within the training set, but this is unlikely to fully resolve the misclassification. The classifier instances within this study already have more true positive ROIs than false positive ROIs for all diatom categories, indicating that our classifications are already accurate qualitatively. Reduction of false negatives is needed to quantitively measure any diatom category other than diatom rods. Two potential additional measures would be to include out of focus ROIs within the training set or to apply a focusing algorithm to sharpen ROIs, but neither method consistently results in increases to CNN classifier accuracy (Pei *et al.,* 2019). The effect of addition of additional training set ROIs will be addressed in future work. Nevertheless, we have shown that our current CNN methodology is sufficiently accurate to characterize diatom hotspots observed within the Slope Sea, both herein and in Oliver *et al.* (2021).

## 2.5 Figures

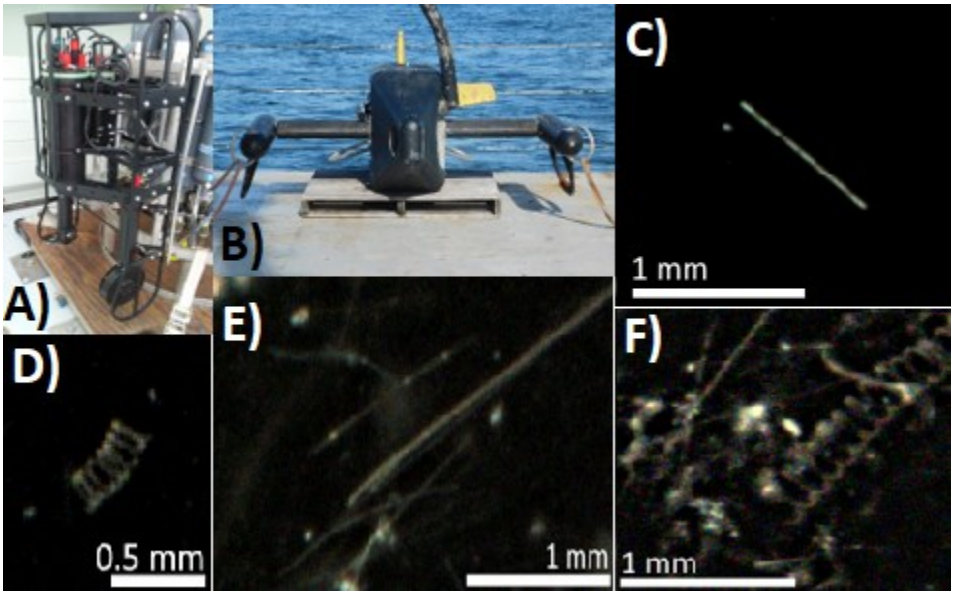


Figure 2.1: A) The DAVPR mounted on the rosette. B) The towed Video Plankton Recorder II, immediately prior to deployment. C-F) Example training ROIs for diatom rods (C), diatom coils (D), diatom bloom without marine snow (E), and diatom bloom with marine snow (F).

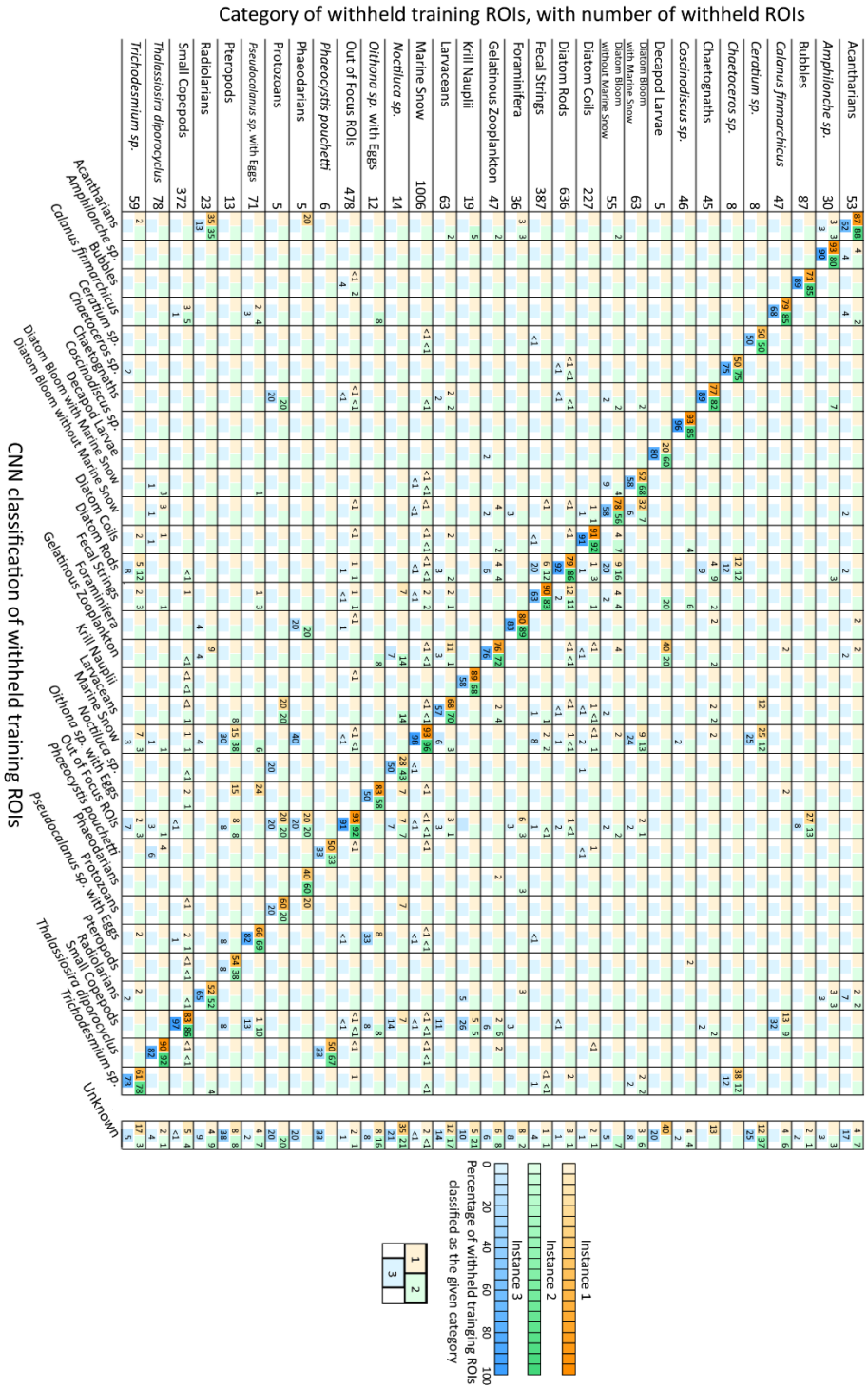


Figure 2.2: Confusion matrix showing the classification of withheld training ROIs by all three instances (three colors within each cell). Categories on the left are positive, with categories on the bottom being conditional positive. Numbers within the cells are the percentage of withheld ROIs classified as that category. Cells along the diagonal show the true positive rate and cells off of the diagonal show the false negative rate. Unknown is a diagnostic category for ROIs that did not meet the threshold criterion of 0.5.

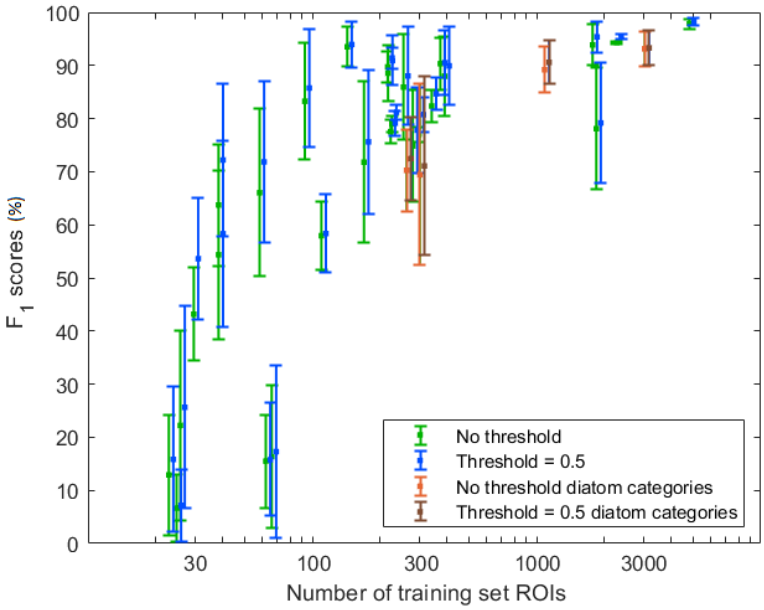


Figure 2.3: Mean and standard deviation of $F_1$ scores (%) for the three classifier instances plotted against number of ROIs in the training set for each category. $F_1$ score statistics for classifier instances without a threshold (green) are offset slightly to the left of those with a threshold of 0.5 (blue) to improve clarity. Diatom categories from left to right: diatom bloom with marine snow, diatom bloom without marine snow, diatom coils, and diatom rods.

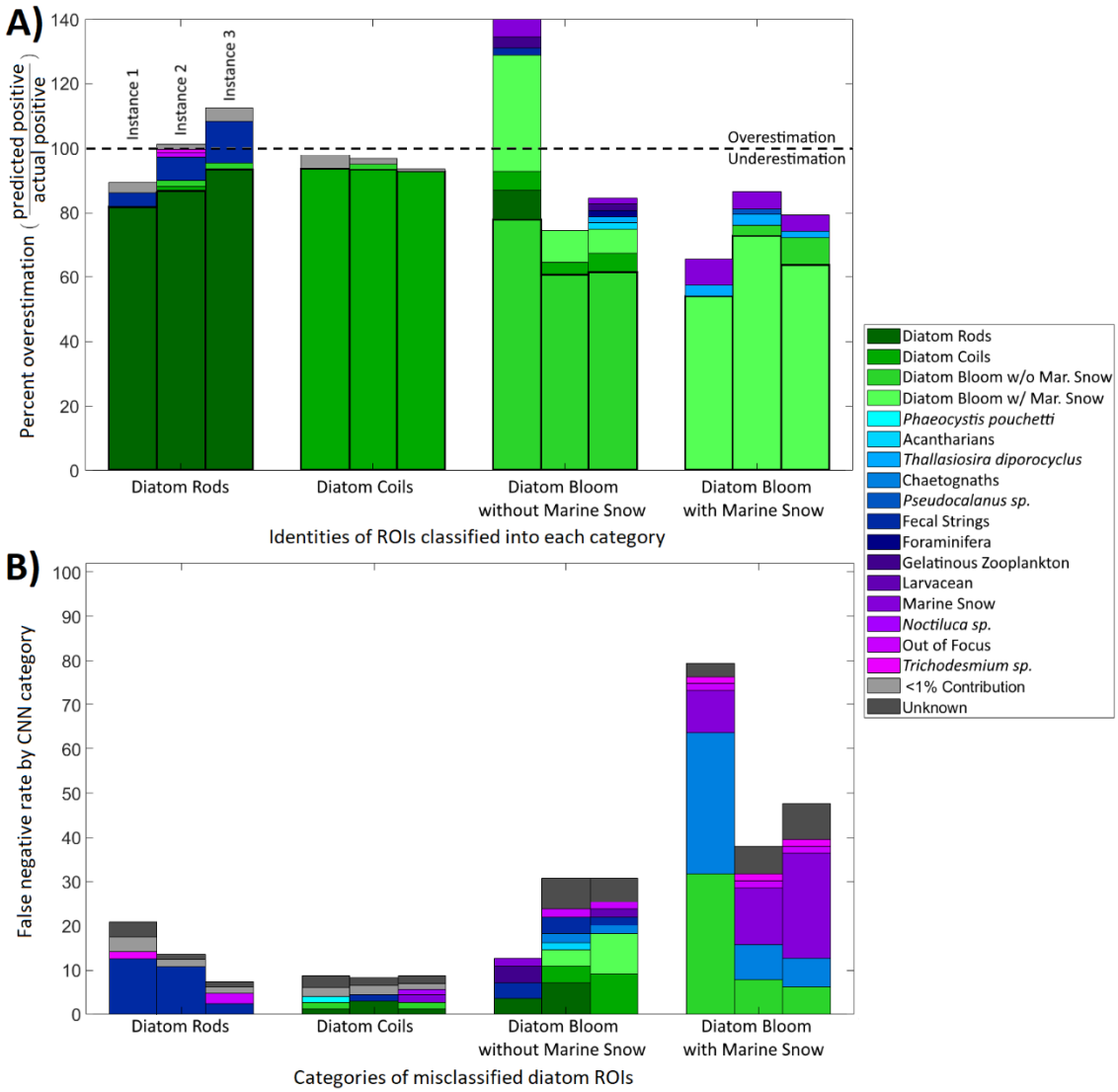


Figure 2.4: A) Percent overestimation and underestimation of withheld training ROIs by CNN classification for the diatom categories. The bold outlined bar is the true positive rate. Other bars are false positives standardized by the number of withheld ROIs within the specified diatom categories. Colors refer to the manual classification of a ROI. B) False negative rate by manually annotated category for withheld ROIs. Colors refer to the CNN classification of a ROI. Categories are assigned the same colors in A and B (e.g., diatom rods are dark green in both cases).

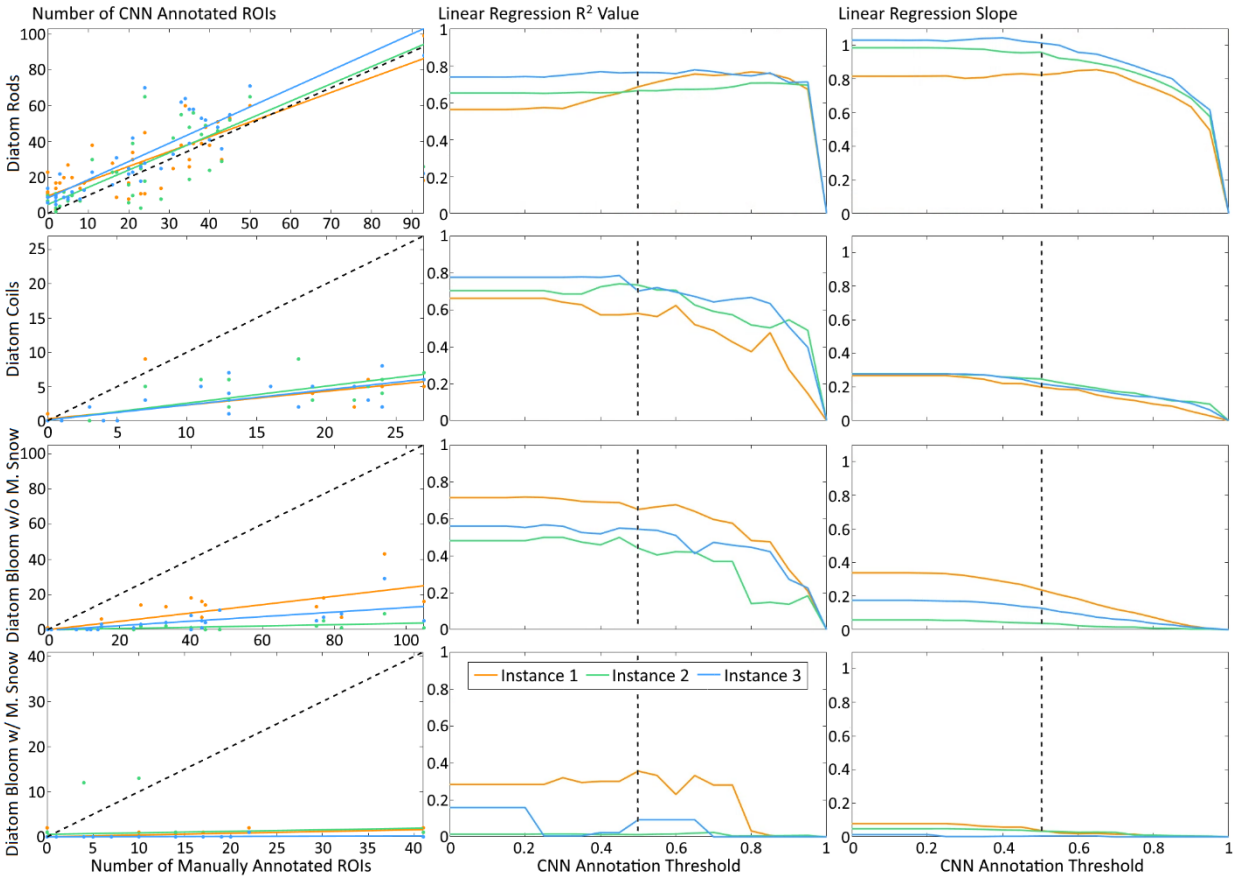


Figure 2.5: CNN classification of manually annotated VPRII ROIs for each diatom category. The left column compares CNN classification counts with the number of manually annotated ROIs within each subset of 200 ROIs. The solid lines are the linear regressions of these points for each instance. The black dashed line is 1:1. For the left column, a threshold cutoff of 0.5 was used for classification. The middle and right columns show the linear regression $R^2$ values and slopes respectively, as they depend on choice of threshold. The dotted vertical line is at 0.5 threshold.

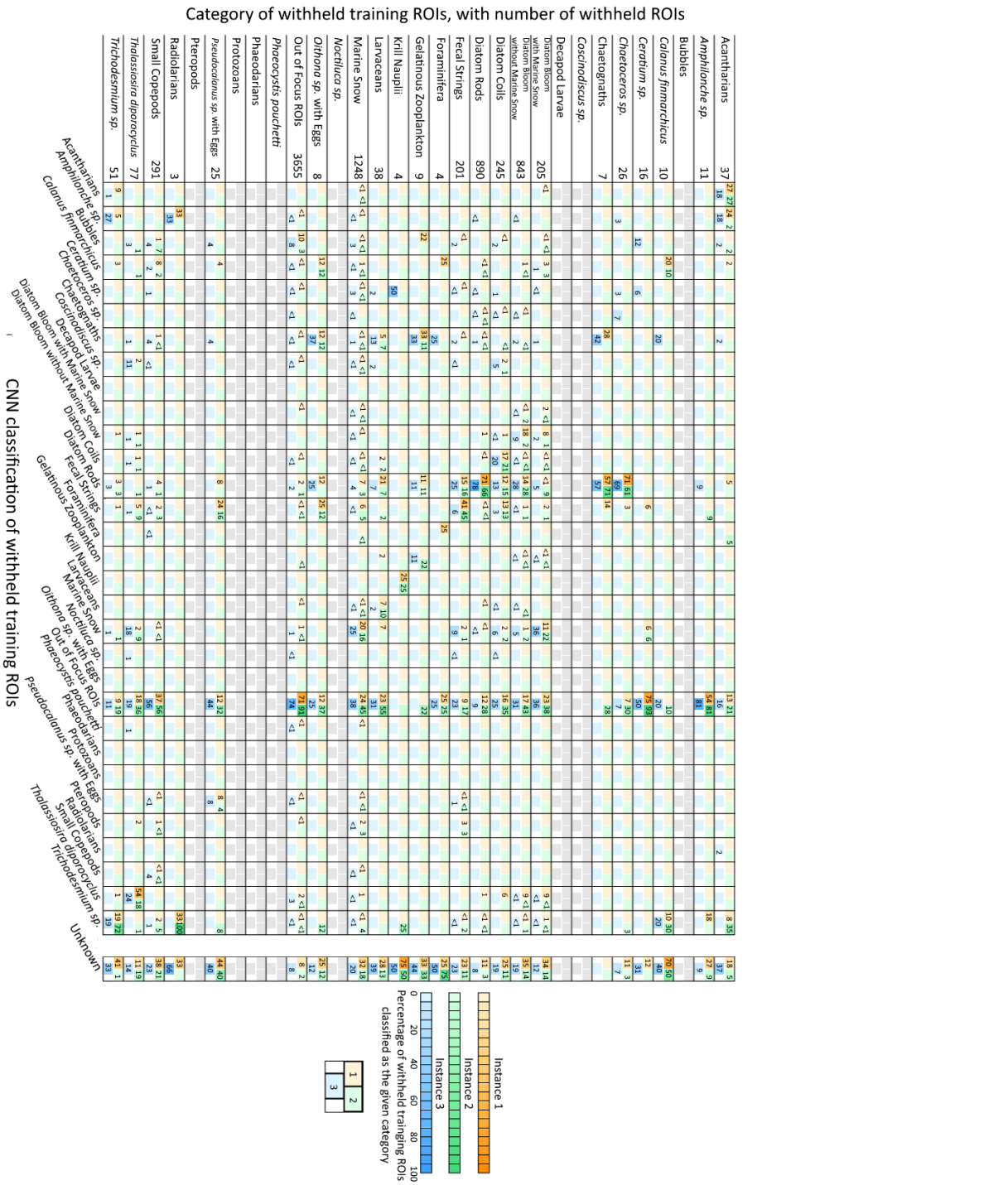


Figure 2.6: Confusion matrix showing the classification of manually annotated VPRII ROIs by all three instances (three colors within each cell) using a threshold of 0.5. Categories on the left are positive, with categories on the bottom being conditional positive. Numbers within the cells are the percentage of VPRII ROIs classified as that category. Cells along the diagonal show the true positive rate and cells off of the diagonal show the false negative rate. Unknown is a diagnostic category for ROIs that did not meet threshold criteria. Grayed out categories were not present within the selected subset of VPRII ROIs.

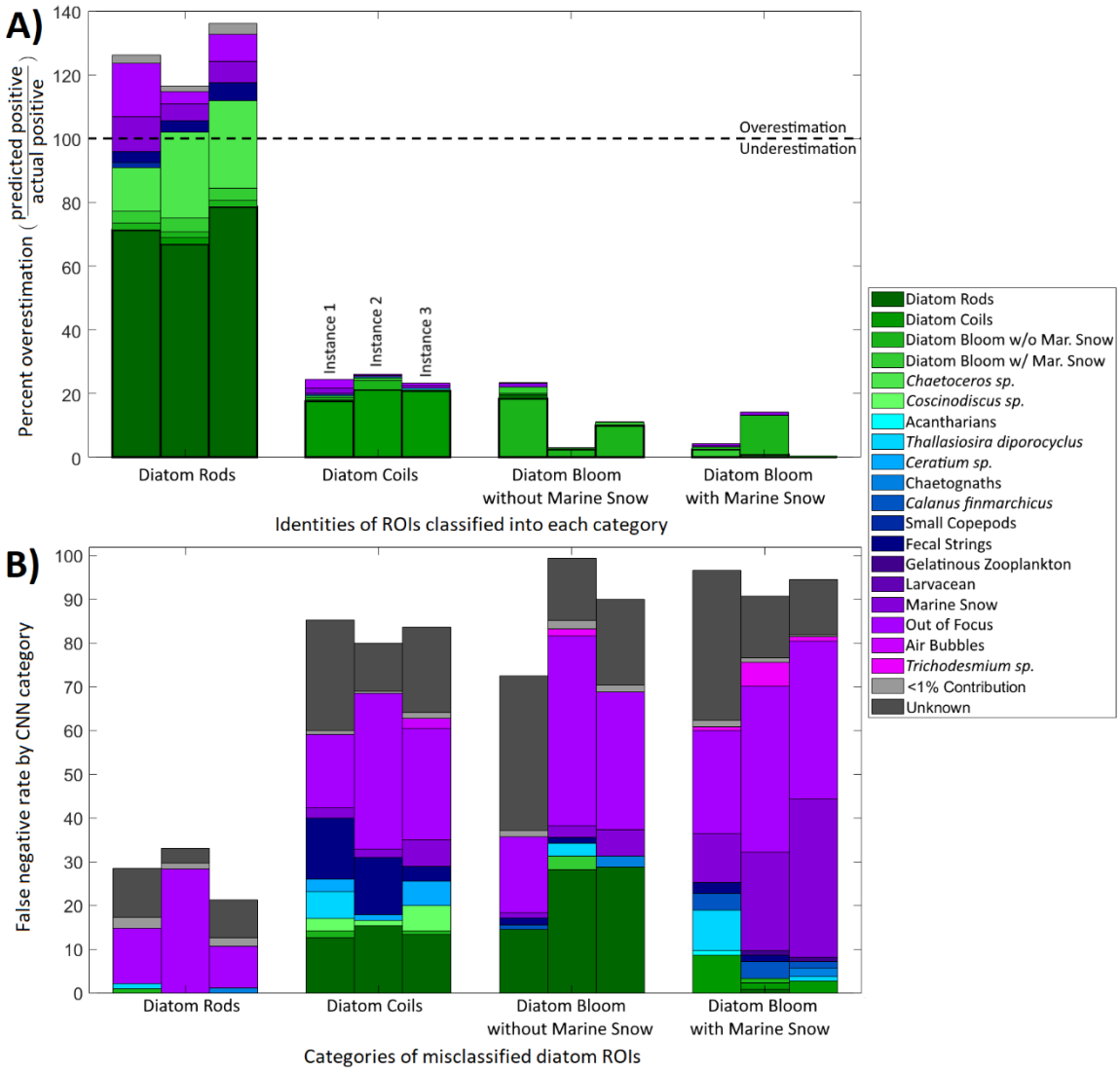


Figure 2.7: A) Percent overestimation and underestimation of manually annotated VPRII ROIs by CNN classification for the diatom categories. The bold outlined bar is the true positive rate. Other bars are false positives standardized by the number of withheld ROIs within the specified diatom categories. Colors refer to the manual classification of a ROI. B) False negative rate by manually annotated category for VPRII ROIs. Colors refer to the CNN classification of a ROI. Categories are assigned the same colors in A and B (e.g., diatom rods are dark green in both cases).

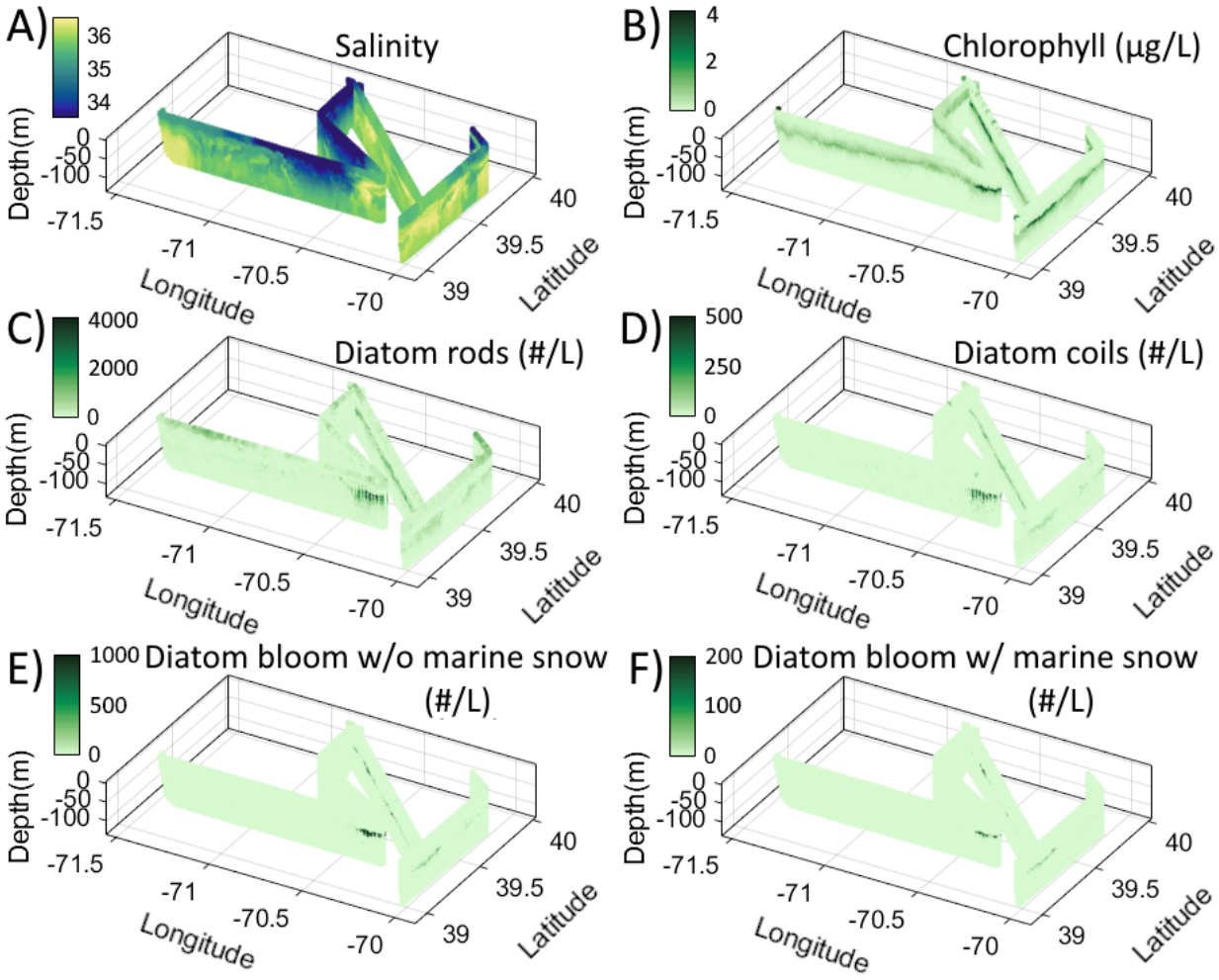


Figure 2.8: VPRII diatom category distributions and sensor information. A and B are from the onboard CTD and ECO Triplet respectively. C-F are full distributions of the above VPRII tows for each diatom category as classified by Instance 1.

## 2.6 Supplemental Figures

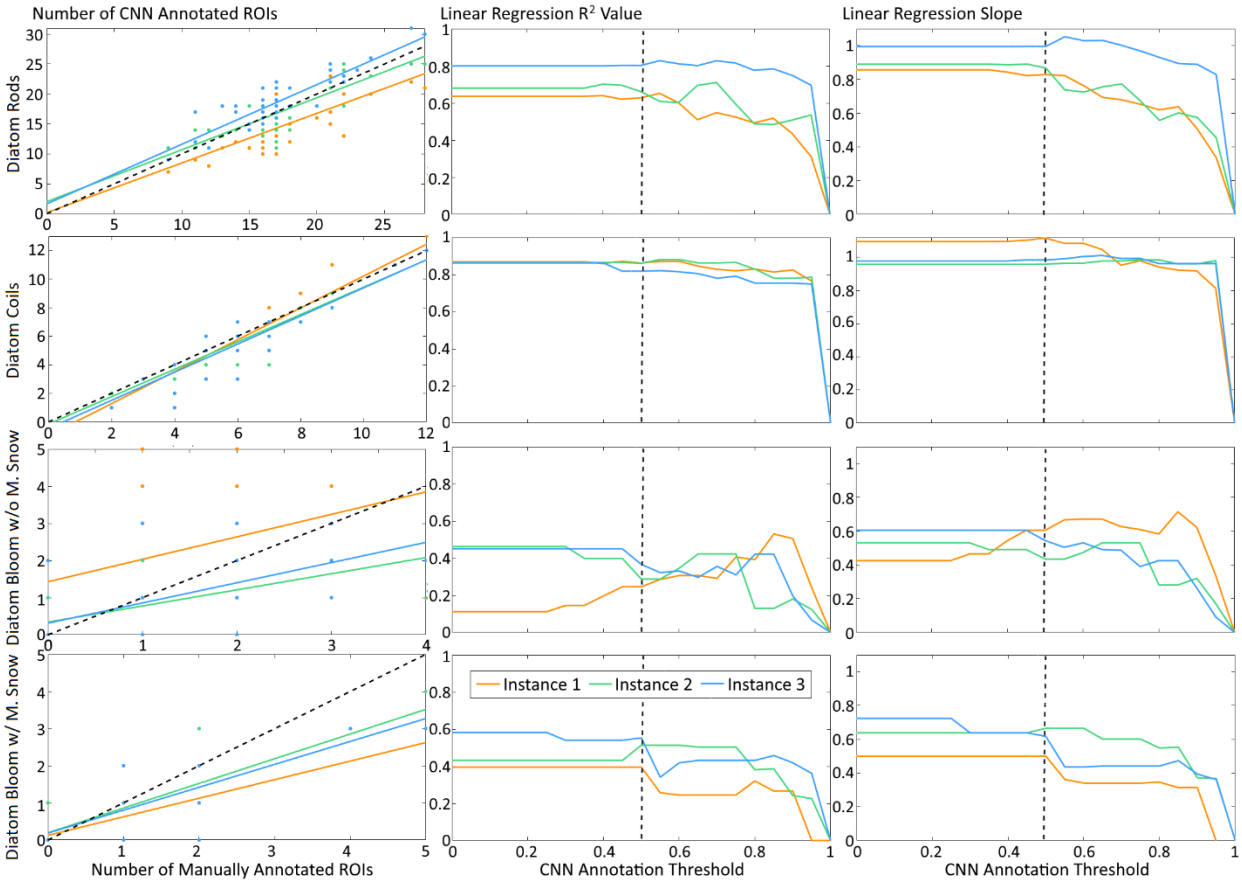


Supplemental Figure 2.1: CNN classification of withheld training ROIs for each diatom category. The left column compares CNN classification counts with the number of manually annotated ROIs within each subset of 100 ROIs. The solid lines are the linear regressions of these points for each instance. The black dashed line is 1:1. For the left column, a threshold cutoff of 0.5 was used for classification. The middle and right columns show the linear regression $R^2$ values and slopes respectively, as they depend on choice of threshold. The dotted vertical line is at 0.5 threshold.

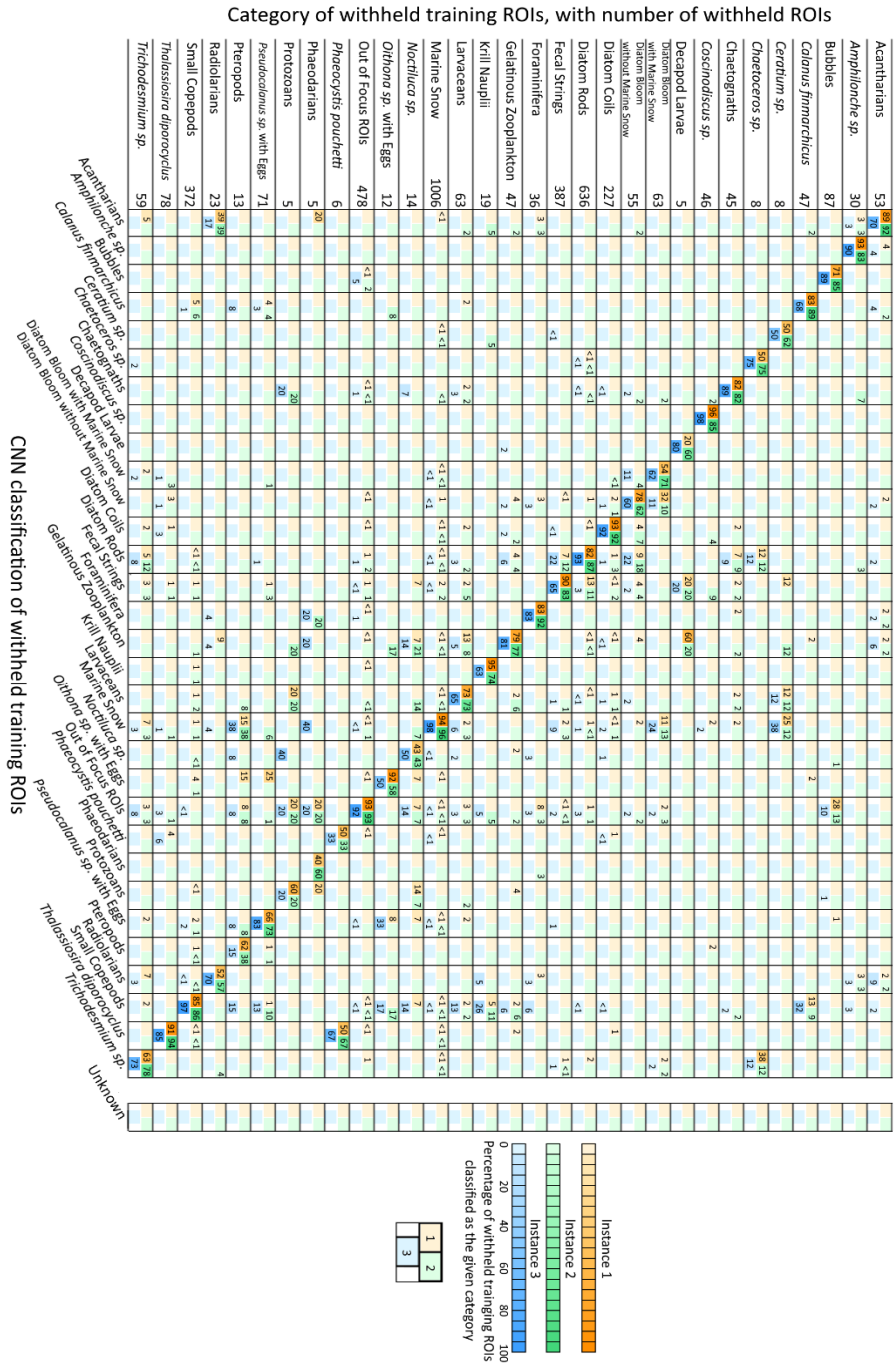


Supplemental Figure 2.2: Confusion matrix showing the classification of withheld training ROIs by all three instances (three colors within each cell) using a threshold criterion of 0. This makes all unknown counts identically 0. Categories on the left are positive, with categories on the bottom being conditional positive. Numbers within the cells are the percentage of withheld ROIs classified as that category. Cells along the diagonal show the true positive rate and cells off of the diagonal show the false negative rate.

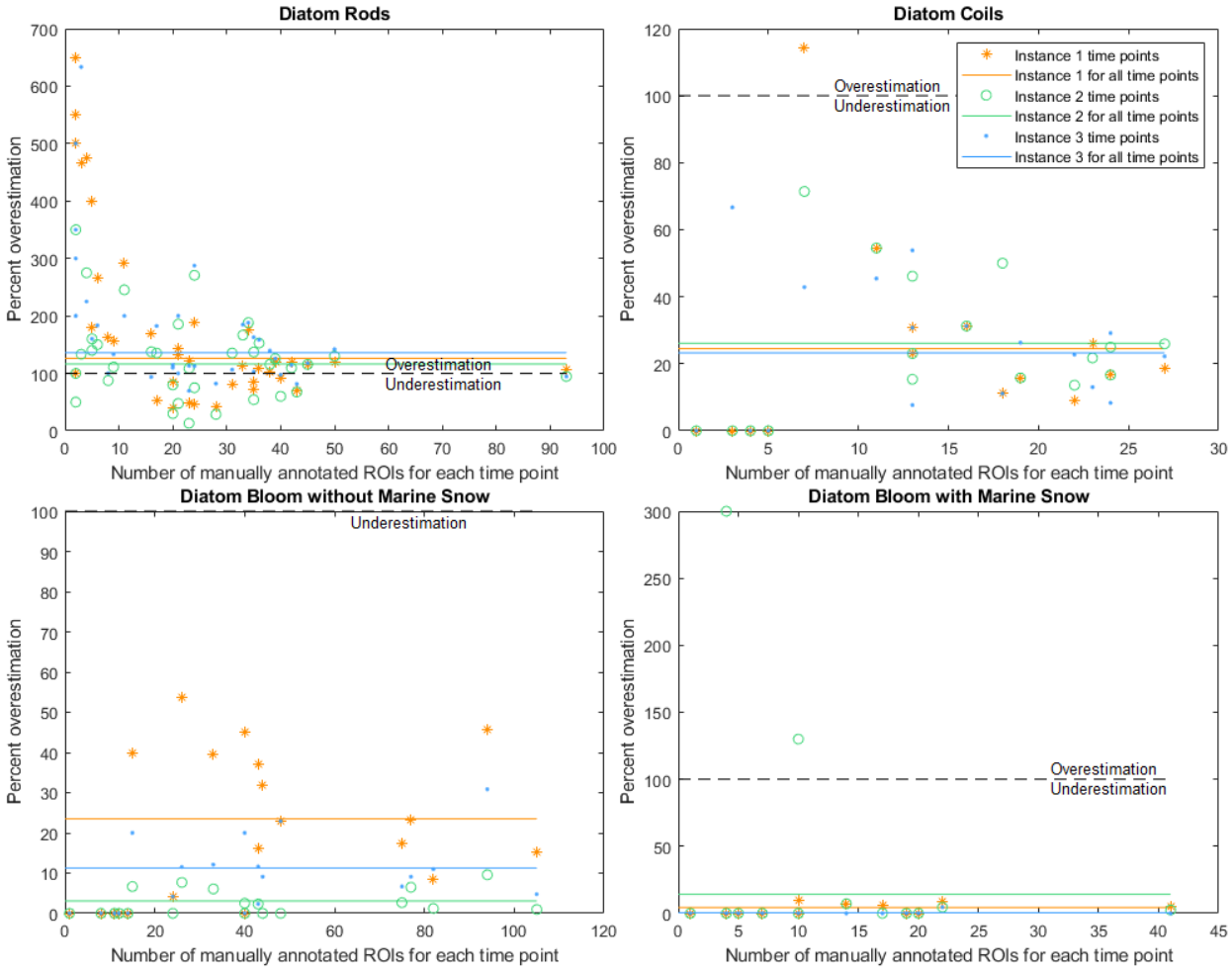


Supplemental Figure 2.3: Percent overestimation for the 40 time points of manually annotated VPRII ROIs for each diatom category. Overlaid on each plot are the percent overestimation values shown in Figure 2.7 for each category and classifier. Note that time points where there were no manually annotated ROIs belonging to that category are not shown due to the percent overestimation for those points being undefined.

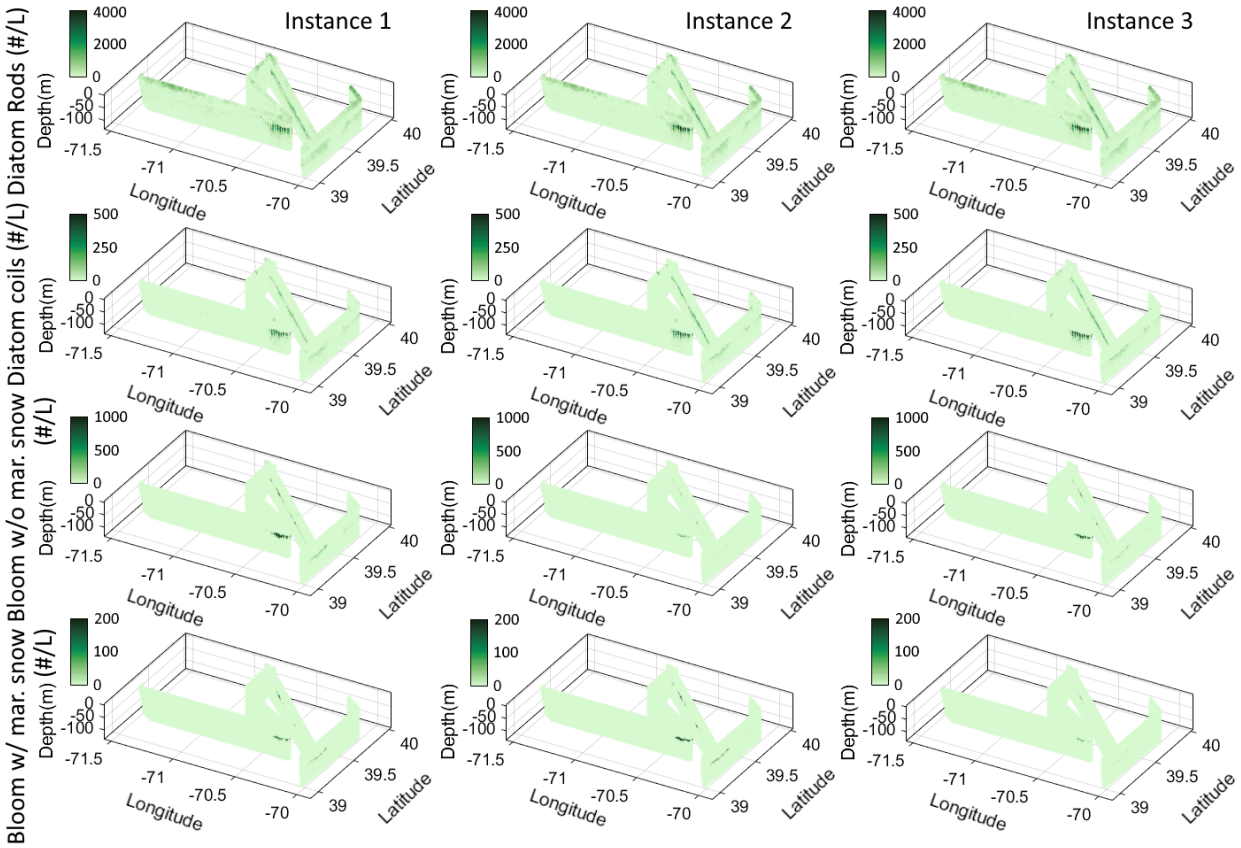


Supplemental Figure 2.4: VPRII diatom category predicted distributions for all instances. Columns are instances 1-3 and rows are each of the four diatom categories.

# Chapter 3

## High Resolution Analysis of Plankton Distributions at the Middle Atlantic Bight Shelf-Break Front

### 3.0 Abstract

The Middle Atlantic Bight (MAB) is a highly productive ecosystem, supporting several economically important commercial fisheries. Chlorophyll enhancement at the MAB shelf-break front has been observed only intermittently, despite numerous studies that suggest persistent upwelling at the front. High resolution cross-frontal transects were collected from three two-week cruises in April 2018, May 2019, and July 2019. Mesoplankton distributions at the front were measured with a Video Plankton Recorder equipped with hydrographic and bio-optical sensors. Each of the three cruises had distinctly different frontal characteristics, with low variability in frontal position in April 2018 and higher variability in May and July 2019 due to frontal eddies and a Gulf Stream warm core ring, respectively. Eulerian means of all transect crossings within each cruise did not show frontal chlorophyll enhancement in April 2018 or July 2019, despite individual crossings showing chlorophyll enhancement in April 2018. Transformation of the April 2018 data into a cross-frontal coordinate system revealed a weak enhancement of chlorophyll and small copepods at the front. Mean frontal chlorophyll enhancement was observed in May and was associated with enhancement in the periphery of a frontal eddy rather than upwelling at the front itself. None of the planktonic categories observed were enhanced at the front in the cross-shelf mean distribution, though diatom chains and small copepods were more abundant inshore of the front, particularly in May and July 2019, as well as within the center of a frontal eddy in May. The high variability of the MAB frontal region

obscured the impact of ephemeral frontal enhancement in mean observations of April 2018, while frontal eddies contributed to chlorophyll enhancement in mean observations of May 2019. The influence of both argues for the necessity for 3-D models rather than idealized 2-D models to explain frontal behavior and its effects on biological responses.

## 3.1 Introduction

The Middle Atlantic Bight (MAB) ranks amongst the most productive ecosystems in the world (O'Reilly and Bush, 1984), resulting in commercial fishing that contributes substantially to the regional economy (Sherman *et al.,* 1996). The MAB occupies a broad continental shelf in the Northwest Atlantic, stretching from Georges Bank to Cape Hatteras. Within the MAB, cold and fresh water on the shelf is separated from offshore warm and salty water by a shelf-break front. Climatological conditions of the frontal region have been described by multiple studies (Linder and Gawarkiewicz, 1998; Loder *et al.*, 2001; Zhang *et al.*, 2011), all of which show that the physical, biological, and chemical attributes of the shelf-break front vary significantly in both time and space. Such variabilities may come from internal or external forcing and occur over broad and fine spatial scales. Frontal meanders may have different hydrodynamic balances between meander troughs and their successive crests (Pickart, 1999). Frontal-generated submesoscale eddies (Gawarkiewicz *et al.*, 2001), Gulf Stream warm core rings (Ryan *et al*., 2001), and, in rare instances, meanders of the Gulf Stream (Gawarkiewicz *et al.*, 2018) may interact with the shelf-break front, changing its physical and biological characteristics. The high variability within and surrounding the shelf-break front poses a unique challenge in understanding its hydrographic and ecological properties, the latter of which can be influenced by both bottom-up (*i.e.,* nutrient supply) and top-down (*i.e.*, grazing) controls.

Elevated chlorophyll levels have been detected at the front from remotely sensed (e.g., Ryan *et al.*, 1999a) and *in situ* (e.g., Marra *et al.*, 1990) observations. There are a variety of processes that can enhance chlorophyll at the front. When nutrients are in abundance in the early spring, Ekman re-stratification can relieve light limitation in phytoplankton, causing enhancement of chlorophyll at the front (Oliver *et al.,* 2022). At other times of year, when nutrients are depleted in the euphotic zone, chlorophyll enhancement can potentially result from several mechanisms of upwelling at the front. The first mechanism is upwelling flow associated with convergence of the inshore bottom boundary layer at the foot of the front, which then detaches from the sea floor and rises toward the surface along frontal isopycnals. Bottom boundary layer convergence and detachment have been both modelled for the MAB (e.g., Gawarkiewicz and Chapman, 1992; Chapman and Lentz, 1994) and observed directly in the MAB (e.g., Houghton and Visbeck, 1998; Houghton *et al.*, 2006). Upwelling rates are typically 10 m $day^{-1}$ (Barth *et al.,* 1998; Benthuysen *et al.,* 2014; Houghton and Visbeck, 1998; Houghton et al., 2006), though some estimate vertical velocities in excess of 20 m $day^{-1}$ (Gawarkiewicz *et al.*, 2001; Pickart, 2000). A second proposed mechanism is upwelling of waters from the offshore interior. From a climatologically based 2-D model, Zhang *et al.* (2011) showed that mean flow within the surface and bottom boundary layers is predominantly offshore, due to the influence of mean wind stress and bottom Ekman layer dynamics respectively. These offshore flows are balanced by interior onshore flow parallel to the seafloor, causing mean upward motion of offshore waters with speeds of tens of cm $d^{-1}$ to a few m $d^{-1}$ depending on the season (Zhang *et al*., 2011). A third mechanism is driven by instabilities within the shelf-break front. Frontal meanders create mesoscale and submesoscale patches of high relative vorticity, positive or negative, on either side of the shelf-break front (Zhang and Gawarkiewicz*,* 2015), which can

result in upwelling of tens of meters per day, similar to rates estimated by the first mechanism. None of these mechanisms are mutually exclusive – events of chlorophyll enhancement seen at the front could result from a combination of these mechanisms of nutrient supply.

Despite evidence for the co-occurrence of chlorophyll enhancement and upwelling at the shelf-break front, the relationship between the two is poorly understood. A 2-D model by Zhang *et al.* (2013) suggested that upwelling may not result in a substantial increase in chlorophyll at the front because of increased grazing by zooplankton. Alternatively, the high variability of the shelf-break front may have obscured chlorophyll enhancement in the 2-D means of the observations (Zhang *et al*., 2013). In an *in situ* study, Hales *et al.* (2009b) observed bottom boundary layer detachment without a substantial increase in phytoplankton at the base of the euphotic zone. Despite measured nutrient and light levels that should have been sufficient to enhance phytoplankton growth, there was no evidence of an increase in zooplankton grazers to account for the lack of a phytoplankton increase, making these findings difficult to reconcile with models.

The objective of this paper is to address the apparent discrepancy between bottom-up stimulation of productivity via upwelling and the lack of chlorophyll and planktonic enhancement at the shelf-break front. Our observational approach consists of repeated, high resolution surveys across the front, extending into the adjacent shelf and Slope Sea waters. These surveys will be used to measure frontal enhancement or lack thereof, as well as cross-frontal planktonic assemblages, in order to better understand the base of the food web of this commercially important region.

## 3.2 Methodology

Our chosen study site was a section of the MAB south of Cape Cod and Nantucket Shoals, Massachusetts. Our measurements were located along the same transect (Figure 3.1) currently used for the Northeast U.S. Shelf Long-term Ecological Research (NES-LTER), near the Ocean Observatories Initiative Pioneer Mooring Array (Gawarkiewicz *et al.*, 2018). We sampled the transect approximately every other day for the duration of three two-week cruises (*R/V Neil Armstrong* AR29, 16-28/04/2018; *NOAAS Ronald H. Brown* RB19-04, 12-25/05/2019; *R/V Thomas G Thompson* TN368, 5-18/07/2019). Transect stations were 7 km apart, with the farthest inshore and offshore stations having depths of 64 m and 1882 m, respectively. This station placement and sampling frequency covers the typical location of the front between the 100-m and 200-m isobaths (Hales *et al*., 2009a) and can capture the passing of frontal meanders of ~15 km amplitude and 4-day period (Gawarkiewicz *et al.,* 2004).

Station profiles were measured by a Seabird SBE 911+ (conductivity, temperature, and pressure) and a WetLabs FLNTURTD fluorometer (chlorophyll fluorescence) mounted upon a rosette. Seawater samples were taken at discrete depths with 24 10-L Niskin bottles mounted on the rosette. Nitrate, phosphate, and silicate concentrations in samples were processed in the Woods Hole Oceanographic Institution Nutrient Analytical Facility. Plankton were imaged with a Digital Auto Video Plankton Recorder (DAVPR, from SeaScan Inc.) mounted upon the CTD rosette. The DAVPR included a Seabird Electronics Inc. CTD (SBE 49 FastCat), fluorometer (FLNTURTD-4620), and synchronized video camera and xenon strobe (Davis *et al.,* 2004). Both CTD and DAVPR measurements were averaged into 1-m depth bins. DAVPR video frame frequency and dimensions were 20 Hz and 1392 x 1040 pixels. The volume imaged was ~10 x 7 x 25 mm. Plankton were extracted from video frames as “regions of interest” (ROIs) with object

identification software and were saved with a time-stamp naming convention (Davis *et al.,* 2004). For April 2018, ROIs were extracted with stricter criteria (*e.g.,* higher sobel threshold, higher focus kernel size) due to the presence of a *Phaeocystis pouchetii* bloom in the region (Smith *et al.*, 2021), which caused video frames to contain an abundance of out-of-focus *P. pouchetii* colonies in the background of video frames. The stricter criteria were applied for all of AR29, which resulted in lower overall category concentrations than other cruises as relatively fewer ROIs were extracted. Trends in category distribution did not appear to change based on ROI extraction criteria when tested with less stringent criteria. ROIs were manually annotated to the highest level of taxonomic identification possible based on imagery alone. Herein we focus our analysis on the most abundant categories: diatom chains and small copepods.

### *3.2.1 Frontal Detection and Alignment*

The shelf-break front is a highly dynamic region with changing hydrodynamic characteristics. For ease of comparison, we used the convention of earlier studies (e.g., Linder and Gawarkiewicz, 1998) considering the 34.5 isohaline as a metric for the location for the shelf-break front. Eulerian means were calculated from station casts by averaging measurements taken at the same station and within the same 1-m depth bins. Variability between transects was calculated by taking the standard deviation of the measurements averaged to create the Eulerian mean transects.

Frontal position often varied between successive transects. In such cases, computing an Eulerian mean averaged by station could smooth out and obscure patterns that might be located near the front. Previous studies have accounted for frontal movement by converting to a cross-frontal coordinate system. Cross-frontal coordinates place the position of the front as the origin,

with locations onshore being negative and locations offshore being positive. Averaging under this coordinate system thus preserves relative location from the front. One major difference between the cross-frontal coordinate system used in this study and that of previous studies was that the entire vertical profile of the front was considered when converting to cross-frontal coordinates, rather than using the head (e.g., Hales *et al.*, 2009b) or foot (e.g., Linder and Gawarkiewicz, 1998; Zhang *et al.,* 2013) of the front. To achieve that, transect data were first bilinearly interpolated onto a horizontal grid of 1-km resolution for each 1-m depth bin. This artificial increase of the cross-shelf horizontal resolution of the station transect data from 7 km to 1 km ensured consistent resolution among all the transects. For the purpose of plotting, the location of the 34.5 isohaline at each depth was defined as the origin for each depth, such that distance from the front was determined as = Original Position – Position of the 34.5 Isohaline. Essentially, the frontal 34.5 isohaline was realigned vertically. This method retained the horizontal (cross-shelf) position of all data points relative to the front for all transects when averaging, regardless of the frontal structure.

## 3.3 Results

### *3.3.1 Transect Eulerian Means*

The Eulerian mean transect for each cruise was constructed by spatially averaging 10 transect crossings in April 2018, 6 crossings in May 2019, and 7 crossings in July 2019 (Figure 3.2) without performing frontal alignment.

April 2018 had the weakest vertical stratification of the three cruises. During that period, nitrate, phosphate, and silicate were all relatively abundant throughout the water column, with the highest surface concentrations of all three cruises. Surface nitrate depletion ($< 0.1$ μmol $L^{-1}$)

only occurred at the farthest inshore stations above a patch of high chlorophyll (>20 mg $m^{-3}$). This patch originated from a regional bloom of *P. pouchetii*, with the bulk of this bloom advecting into our transect from its origin on Nantucket Shoals (Smith *et al.*, 2021).

May 2019 had increased vertical stratification compared to April 2018. During May 2019, mid-depth chlorophyll maxima were present throughout the transect, with nitrate, phosphate, and silicate concentrations decreasing near the surface. Surface nutrient depletion was highest offshore for all three nutrients. Surface nitrate was also fully depleted at stations farthest inshore of the front, cooccurring with a decline in phosphate and silicate. Surface chlorophyll was higher in May 2019 (~3.5 mg $m^{-3}$) than in April 2018 (~2 mg $m^{-3}$), excepting the *P. pouchetii* affected waters inshore in 2018. The highest chlorophyll within the May 2019 Eulerian mean was located just inshore of the shelf-break front (4.4 mg $m^{-3}$).

July 2019 showed the greatest vertical stratification, due to the formation of a seasonal thermocline with a shallow mixed layer. Chlorophyll maxima in July 2019 were located below the warm surface mixed layer. Nitrate, phosphate, and silicate were all depleted in the surface throughout the transect, with full nitrate depletion above 30 m depth. The warmer layer extended deeper offshore and a deeper euphotic zone offshore resulted in deeper chlorophyll maxima and deeper nutrient depletion in that area.

### *3.3.2 Frontal Variability in Eulerian Means*

Variability in cross-shelf position of the front head (surface expression) was greater than that of the front foot on the seafloor for all cruises (Figure 3.3, top row). April 2018 had the least variability in frontal position overall and the sharpest gradient between shelf and Slope Sea waters, as reflected by the most vertical isohalines. Salinity variability in April 2018 (Figure 3.3,

middle row) had peak values in the surface layer, corresponding to the cross-shelf motion of the front head. Note that some of the variability on the offshore end resulted from the influence of a Gulf Stream warm core ring in the last few transect crossings (Supplemental Figure 3.1). Chlorophyll variability in April 2018 (Figure 3.3, bottom row) was primarily associated with the inshore *P. pouchetii* bloom and not with the front.

In contrast, July 2019 had the highest salinity variability and the greatest change in frontal position among the three cruises (Figure 3.3, rightmost column). Salinity variability was highest south of approximately 40° N and within the upper 50 m, due to shelf water being advected offshore in a streamer associated with a Gulf Stream warm core ring for the first half of the cruise (Figure 3.4) (Zhang *et al*, in press). This streamer maintained the physical properties of shelf water in the upper 50 m of the water column, extending the offshore end of shelf waters to south of 39.5° N and out of range of our transect. After the streamer passed, the shelf-break frontal structure was restored and the front head returned to approximately 40° N. The mean position of the foot of the front in July 2019 was also located farthest inshore of all cruises, making the mean frontal slope the least steep in July. Chlorophyll variability was highest in waters offshore of the front at approximately 50 m (Figure 3.3). This was associated with a deep chlorophyll maximum (Figure 3.2) driven by a water mass intrusion of Gulf Stream origin. Described in more detail by Oliver *et al*. (2021), this chlorophyll enhancement was observed when high-salinity (>35.6), high nutrient deep Gulf Stream water was lifted into the euphotic zone. The time-averaged imprint of this phenomenon is manifested as a chlorophyll maximum at 50 m located at 39.9°N (Figure 3.2). Individual transect crossings, *e.g.,* year-day 195, had salinities above 36 co-located with chlorophyll maxima (Supplemental Figure 3.2).

Unlike both April 2018 and July 2019, May 2019 showed little salinity variability at the mean location of the head of the shelf-break front or offshore (Figure 3.3). Peak salinity variability was instead inshore of the front, in waters above the foot of the front. This pattern was the result of frontal eddies that were present in all transect crossings in May 2019 (Figures 3.5, 3.6). The first three crossings were influenced by Eddy A (Figure 3.6, first three rows) and the later three were influenced by Eddy B (Figure 3.6 last three rows).

Eddy A began as a filament of warm and salty water from the southeast, which separated cold and fresh shelf waters to the north of the slope water filament from a filament of cold and fresh waters to the south (Figures 3.5, 3.6). Subducted shelf waters are present at roughly 50 m at the deepest point of the shelf filament, extending southwards. Surface chlorophyll in both filaments was approximately equal to background shelf chlorophyll for year-days 133 and 135, both in satellite imagery and *in situ* observations. By year-day 137, both filaments elongated and spiraled towards eddy center (Figure 3.5 upper right). Subducted shelf waters were no longer coherent by year-day 137, with only remnants visible. Chlorophyll was enhanced in the frontal eddy relative to surrounding waters (Figure 3.6 third row), although the enhancement was less evident in satellite imagery (Figure 3.5 upper right). After moving off of the transect (year-days 141), Eddy A had transitioned into a frontal eddy and was no longer discernable from surrounding slope waters.

Eddy B was composed primarily of shelf water, with a core of cold, fresh cold pool water surrounded by slightly saltier and warmer waters more characteristic of shelf waters close to the front. All waters of Eddy B had salinities less than 34.5. Eddy B was characterized by a ring of chlorophyll enhancement around its periphery, which persisted for three ship-based crossings of the eddy. A thin lens of shelf water covering Eddy B (Figure 3.6, last two rows) prevented

precise identification of Eddy B in satellite imagery (Figure 3.5, year-days 143 and 145), but the patterns in SST and surface chlorophyll are indicative of the eddy's presence. For example, a filament of warmer water was advected around the eastern flank of Eddy B on year-days 143 and 145. Surface chlorophyll was marginally higher in satellite imagery in association with both water masses around the periphery of Eddy B. No major changes in hydrographic properties or chlorophyll were evident over the duration that Eddy B was observed.

Neither eddy appeared to be unique; many such eddies occurred at and near the front during May 2019 as well as in other years. Satellite imagery for year-day 142 in particular showed several eddy-like features in close proximity to our transect line (Figure 3.7). Eddies A and B are discussed above, along with two additional eddies, C and D. All four eddies appear to represent similar phenomenology at varying ages with local patches of chlorophyll enhancement.

### *3.3.3 Planktonic Observations*

ROIs from DAVPR observations were manually annotated into 31 categories, with three planktonic categories constituting over 90% of the total distribution of planktonic ROIs (Figure 3.8). *P. pouchetii* comprised approximately three quarters of the total and diatom chains and small copepods comprised 10% each. Most other individual planktonic categories typically contributed less than 1%. The high *P. pouchetii* abundance came almost entirely from April 2018, with the vast majority coming from the inshore regional bloom mentioned earlier. Since *P. pouchetii* had little presence at the front, we focus here primarily on the remaining two common taxa, diatom chains and small copepods. Individuals of both categories were roughly the same size (approximately 1 mm).

Mean distributions of diatom chains and small copepods showed complex relationships with mean hydrographic and chlorophyll distributions (Figure 3.9). Abundance of both categories was lowest in April 2018 and higher in May and July 2019, although this may reflect the stricter criteria used for ROI extraction for April 2018. Diatoms and small copepods were abundant inshore in April 2018, near the *P. pouchetii* bloom. Diatom chains were also abundant offshore in April 2018 to a lesser extent. The offshore enhancement co-occurred with the slightly higher offshore mean chlorophyll concentrations compared to shelf concentrations outside the *P. pouchetii* bloom (Figure 3.2). Neither category was enhanced during the transient episodes of frontal chlorophyll enhancement in individual transect crossings (Supplemental Figure 3.3).

The mean distribution of diatom chains in May 2019 (Figure 3.9) shared some qualitative similarities with mean chlorophyll (Figure 3.2). However, the peak in diatom chains occurred one station farther inshore than that of the peak in chlorophyll, within a region of relatively lower mean chlorophyll. Small copepod abundance showed no mean enhancement at the front. Both mean diatom and small copepod abundances were highest in May 2019 at the two stations farthest inshore.

No mean enhancement in either diatoms or small copepods was seen at the front in July 2019, compared to abundances further inshore and offshore (Figure 3.9). July mean diatom distributions generally corresponded with mean chlorophyll distributions, with peak diatom chain concentrations for this study (>1000 diatoms $L^{-1}$, Supplemental Figure 3.5) observed in association with offshore Gulf Stream intrusions. Concentrations on our transect were similar in magnitude to those reported by Oliver *et al.* (2022) within Gulf Stream intrusions southeast of our transect. Like in May 2019, diatoms and small copepods in July 2019 were both abundant in mean observations at stations farthest inshore of the front. However, in July 2019 the peak mean

diatom concentrations were located below the mixed layer, co-occurring with peak mean chlorophyll, while the peak in small copepods were instead located within the surface mixed layer.

The variability observed in May 2019 provided an opportunity to examine synoptic relationships between hydrography, chlorophyll, diatom, and small copepod distributions (Figure 3.10). While chlorophyll on year-days 133 and 135 was roughly constant throughout Eddy A (Figure 3.6, right column, first two rows), diatom chains and copepods were enhanced in shelf waters around the periphery of the eddy. Nutrients were present in near-surface waters within the interior of Eddy A without significant increases in chlorophyll or diatom chains. Eddy B had chlorophyll enhancement around the periphery (Figure 3.6), while diatom chains and small copepods were enhanced in the center of the eddy, as were nutrient concentrations (Figure 3.9).

### *3.3.4 Frontal Alignment*

Our frontal alignment methodology was designed to correct for variations in frontal position under the condition that the location of the front can be clearly and unequivocally identified with the 34.5 isohaline metric. This was possible in April 2018 due to the high horizontal stratification between inshore and offshore waters. May and July 2019 contained frequent obstructions, primarily in the form of frontal eddies and a warm core ring streamer respectively, making head-to-foot frontal alignment impractical. As mentioned previously, April 2018 individual transects contained patches of highly transient chlorophyll enhancement, which were present on either side of the front. Frontal alignment of April 2018 measurements yielded slightly higher concentrations of mean chlorophyll and small copepods inshore of the front

(Figure 3.11). However, in neither case was this enhancement more than one standard deviation from the mean of surrounding surface waters.

## 3.4 Discussion

Our Eulerian mean measurements found no mean chlorophyll, diatom, or small copepod enhancement at the front in April 2018 and July 2019. This is not a surprising conclusion for July 2019, where chlorophyll, diatoms, and small copepods were primarily abundant in association with the offshore Gulf Stream intrusions or inshore, away from the front. However, several transect crossings in April 2018 showed chlorophyll enhancement at the front (Supplemental Figure 3.1). For example, year-day 108 showed particularly strong chlorophyll enhancement as a result of wind-driven Ekman restratification (Oliver *et al*., 2022). Enhancement also occurred on opposites sides of the front, in close succession. Chlorophyll measurements at the front were highest in shelf waters on year-day 110 and highest in slope waters on year-day 111 (Supplemental Figure 3.1). None of these ephemeral chlorophyll enhancements in April 2018 show up in Eulerian mean observations (Figure 3.2). However, averaging with a frontally-aligned coordinate system shows enhancement of chlorophyll at the front (Figure 3.11), along with small copepods. Thus, in this particular case, frontal movement and variability obscured frontal enhancement in the Eulerian mean observations. Diatom chains were not abundant within the transient frontal chlorophyll enhancements observed in April 2018 (Supplemental Figure 3.3). At least one ephemeral frontal chlorophyll enhancement, that of year-day 108, was associated with an enhancement of nanoplankton, which are too small to be imaged by the DAVPR (Oliver *et al.*, 2022). Nitrate, phosphate, and silicate were available in surface waters at

the front throughout April 2018, despite decreases in concentration inshore and offshore. This extended nutrient availability could be due to upwelling.

May 2019 had chlorophyll enhancement at the front and this enhancement is attributed to frontal eddies. Nutrients were present in near-surface waters within the interior of both eddies, indicative of upwelling (Figure 3.10). The interior of Eddy A did not contain significant increases in chlorophyll or diatom chains, perhaps because upwelling had occurred recently in the eddy core, and insufficient time had passed for the biological response. Subsequent surface chlorophyll enhancement within Eddy A on year-days 141 and 142 support this hypothesis (Figures 3.5, 3.7).

Eddy B had chlorophyll enhancement around its periphery (Figure 3.6), while diatom chains and small copepods were enhanced in the center of the eddy. This corresponded with notable increases in nitrate, phosphate, and silicate within the center of Eddy B, which is suggestive of a recent upwelling event. The coincidence of diatom chains and small copepods could be indicative of a community shift as a result of grazing on smaller phytoplankton by copepods, leaving the larger diatom chains sampled by the DAVPR to flourish. Another possibility is that rapidly growing diatoms responded most quickly to the upwelled nutrients, and copepods aggregated there (perhaps through vertical migration) to graze on them. Yet another possibility is that the high concentrations of diatoms and small copepods reflect the community composition of their source waters in the cold pool (see chapter 4). In any case, the lower chlorophyll within the center of Eddy B despite diatom chain enhancement implies that diatom chains were a small component of the total chlorophyll and/or a had a higher carbon:chlorophyll ratio than other types of phytoplankton.

Surface underway observations in May 2018 made with flow cytometry and Imaging FlowCytobot (IFCB) (see Figure 5.12 in Archibald 2021) documented higher total biovolume concentrations of both picoplankton and nanoplankton in front waters (defined as 34-35 salinity) compared to shelf (<34) concentrations, at the same location as we saw enhancement in mean chlorophyll (Figure 3.2). Most of the subsurface chlorophyll enhancements associated with Eddy B are likely not visible in these surface observations. However, year-day 137 had surface chlorophyll enhancement at the front, as did year-day 144, though chlorophyll on that day was primarily located at depth (Figure 3.6). Neither of these high chlorophyll patches were associated with high diatom chain abundance (Supplemental Figure 3.4).

The overall mean enhancement of chlorophyll at the front in May 2019 was driven by chlorophyll enhancement on the periphery of Eddy B, supporting the hypothesis that frontal eddies can enhance chlorophyll at the front. As noted previously, neither of the eddies we observed were unique (Figure 3.7). Previous studies have observed both similar eddies (*e.g.,* Eddy A: Garvine *et al.*, 1988; Eddy B: Flagg *et al.*, 1997) and similar chlorophyll patches (*e.g.,* May 1980, 1984, (both from Figure 2 of Ryan *et al*., 1999a) and 1997 (Plate 1 of Ryan *et al*., 1999b)), indicating that the frontal eddies such as observed during May 2019 are common and may be important to biological communities near the front.

### *3.4.1 Climatological Comparison*

April 2018 mean frontal position and structure were most similar to winter climatological means (Zhang *et al.*, 2011) (Figure 3.3, upper left). Nutrient and chlorophyll distributions most closely matched the general pattern of winter climatological distributions (Zhang *et al.*, 2013), in that nutrients were available throughout our transect and chlorophyll was much higher inshore.

Later individual transect crossings in April 2018 (*e.g.,* year-days 116, 118) showed nutrients and chlorophyll distributions that were more similar to spring climatological conditions (Zhang *et al.*, 2013).

May 2019 mean frontal position and structure were most similar to spring climatological means (Zhang *et al.*, 2011) (Figure 3.3 middle column). Mean May chlorophyll and nutrient distributions (Figure 3.2, top middle) were similar to climatological distributions (Zhang *et al.*, 2013), indicating that the features observed in this study reflect typical conditions. Climatological surface nutrients in the spring were depleted except at the front (Figure 5b in Zhang *et al.*, 2013), coinciding with where we saw Eddies A and B and where nitrate was enhanced (Figure 3.2, middle column, fourth row). Climatological chlorophyll was highest at the front (Figure 5f in Zhang *et al.*, 2013), similar to what was seen in our mean May measurements as well.

July 2019 mean frontal position and structure did not match summer climatological means (Zhang *et al*., 2011), due to the presence of the shelf water streamer and the Gulf Stream intrusion (Figure 3.3 upper right). The offshore deep chlorophyll maxima observed were stronger than in the climatological means (Zhang *et al*., 2013) due to the influence of Gulf Stream water intrusions. Nitrate measurements and inshore chlorophyll measurements were consistent with climatological mean distributions (Zhang *et al*., 2013).

Enhancement of diatoms and copepods on the shelf in both May and July 2019 was located within regions of climatological chlorophyll enhancements inshore (Zhang *et al*., 2013), indicating that our observed abundance of diatom and small copepod may be a typical feature for this region.

## 3.5 Conclusion

The MAB shelf-break front is a highly dynamic environment heavily influenced by a variety of forcings, internal and external, both biological and physical. Confluence of these forcings complicates diagnosis of causative mechanisms underlying the observed distributions. In April 2018, chlorophyll enhancement at the front was highly transient, typically lasting on the order of days. Movement of the front obscured this enhancement within Eulerian means, but not when averaging over a frontally-aligned coordinate system. In contrast, enhancement caused by Eddy B in May 2019 was sufficient to affect the mean fields of not only chlorophyll but also diatoms and small copepods. These features had a significant effect on mean observations partially due to limited duration of sampling – it is plausible that sampling on scales longer than 2-weeks per cruise may be necessary to isolate upwelling trends within the highly variable frontal environment. However, the involvement of frontal eddies and upstream influences throughout all three cruises highlights the need for future studies to consider frontal processes in three dimensions, especially since few of the 23 transect crossings presented herein were free of any features affecting the front itself, such as rings, streamers, intrusions, etc. All three cruises presented in this study departed from the main transect line to conduct 3-D synoptic sampling of the some of the features discussed herein, *e.g.,* the *P. pouchetii* bloom in April 2018 (Smith *et al.,* 2021), the streamer (Zhang *et al*, in press) and Gulf Stream intrusions observed in July 2019 (Oliver *et al.*, 2021), and both eddies discussed in May 2019. In the following chapter, further analysis of the May 2019 cruise will investigate transient features associated with these 3-D processes.

## 3.6 Figures

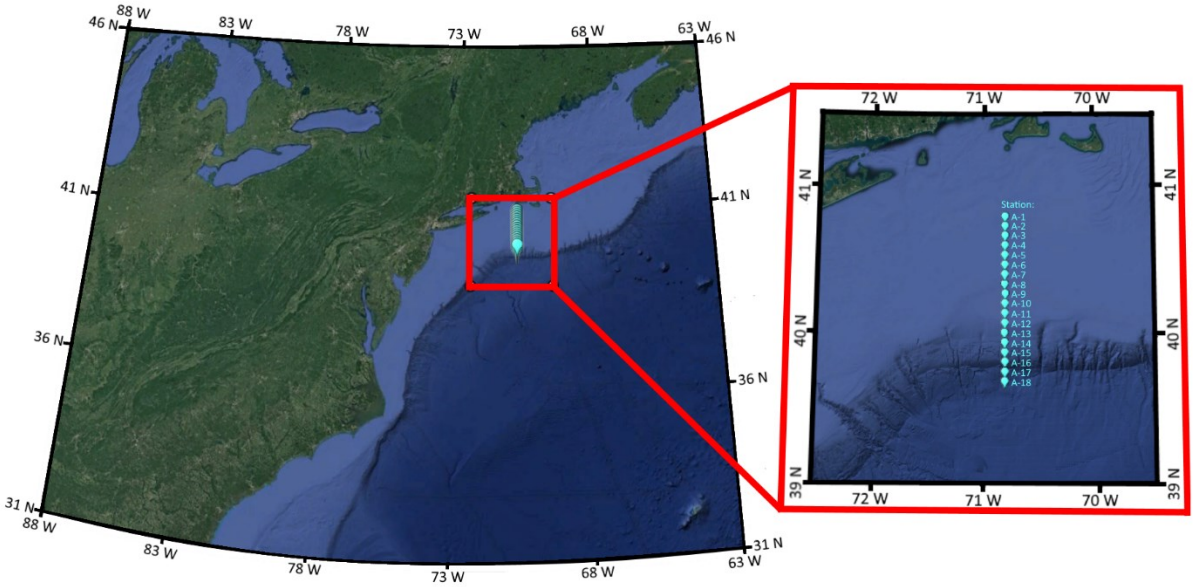


Figure 3.1: General Transect Location. Station A-1 is located at 40.7 N, 70.8 W. Station A-18 is located at 39.6 N, 70.8 W. Stations are ~7 km apart along the 70.8 W meridian. The 100m isobath is located at Station A-7. Background imagery is from Google Earth.

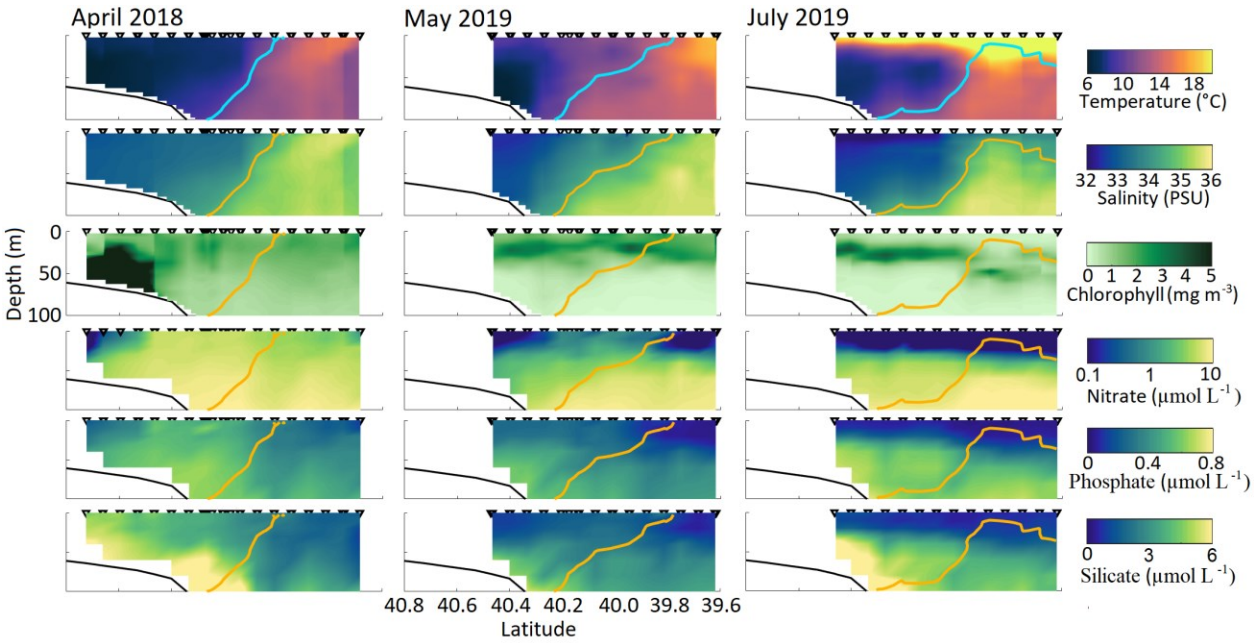


Figure 3.2: Eulerian mean transects for each of the three cruises. Nitrate concentration is plotted on a nonlinear scale to highlight changes in surface concentration. The locations of the 34.5 isohaline are denoted by the teal (temperature plots) and orange lines (all other plots). Station locations are denoted by the black triangles above the transect, though not all stations were sampled for each transect. The 34.5 isohaline extends offshore in July 2019 due to a streamer caused by a Gulf Stream warm core ring. The waters most characteristic of offshore waters in this cruise are located 39.8 - 40° N, where the 34.5 isohaline is closest to the surface. Plots of the individual transects that were used to calculate Eulerian means are shown elsewhere (Top three rows: May 2019 – Figure 3.6, April 2018 and July 2019 – Supplemental Figures 3.1-3.2; Bottom three rows: Supplemental Figures 3.3-3.5).

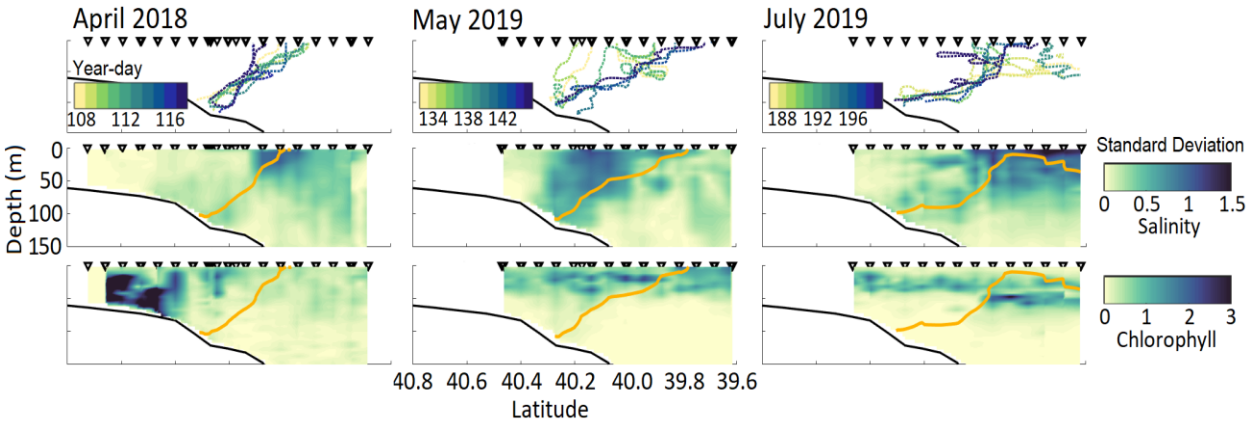


Figure 3.3: Top row) location of the 34.5 isohaline for all transects used to compute mean transects for each cruise. Colors indicate transect date, with yellow being the start of each cruise. Lower two rows) standard deviation of the same values used to compute mean observations, over the same depth/distance bins, for both salinity and chlorophyll. Triangles above the means represent stations used. The orange line represents the mean location of the 34.5 isohaline for each cruise.

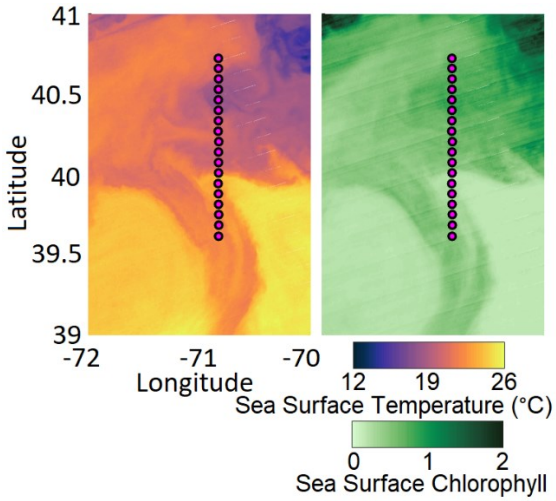


Figure 3.4: Satellite snapshot of the streamer observed on year-day 191 in July 2019. To the left of the streamer is the Gulf Stream warm core ring causing the streamer. The location of the front was at approximately 40° N.

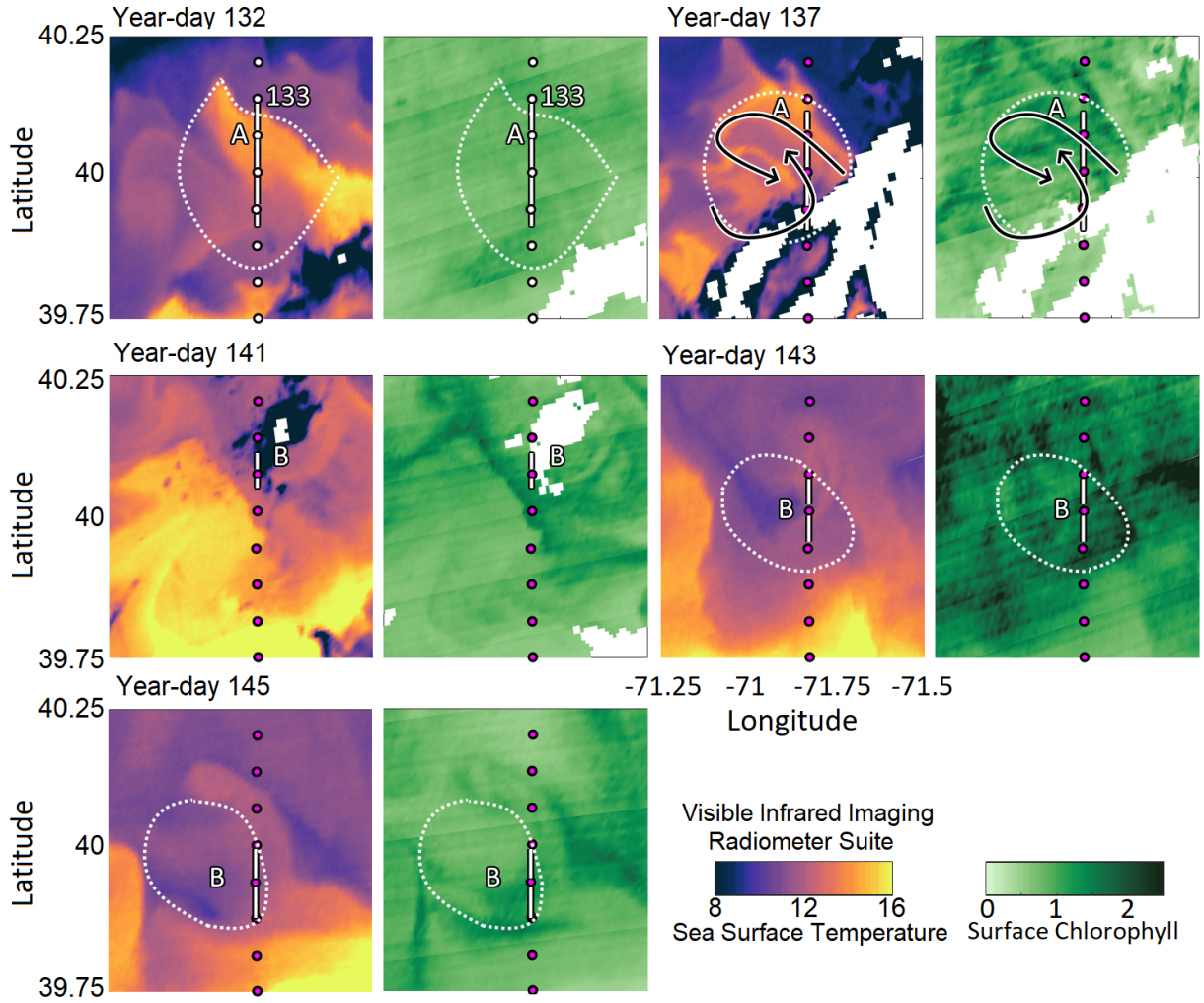


Figure 3.5: Satellite snapshots of features A and B during May 2019, along with temperature transects of each feature. Features in satellite snapshots are roughly outlined by circles and marked by letters within transect plots. The shelf-break front was located south of both features, at approximately 40° N. Station locations are marked by magenta or white dots in satellite images based on whether the transect was or was not sampled respectively on that year-day. White lines represent the location of each feature within transect plots (Figure 3.6), with letters denoting each feature. White dotted lines show the approximate border of features. The transect for year-day 133 was used as reference for the satellite image of year-day 132. Black arrows on year-day 137 represent the slope and shelf water filaments.

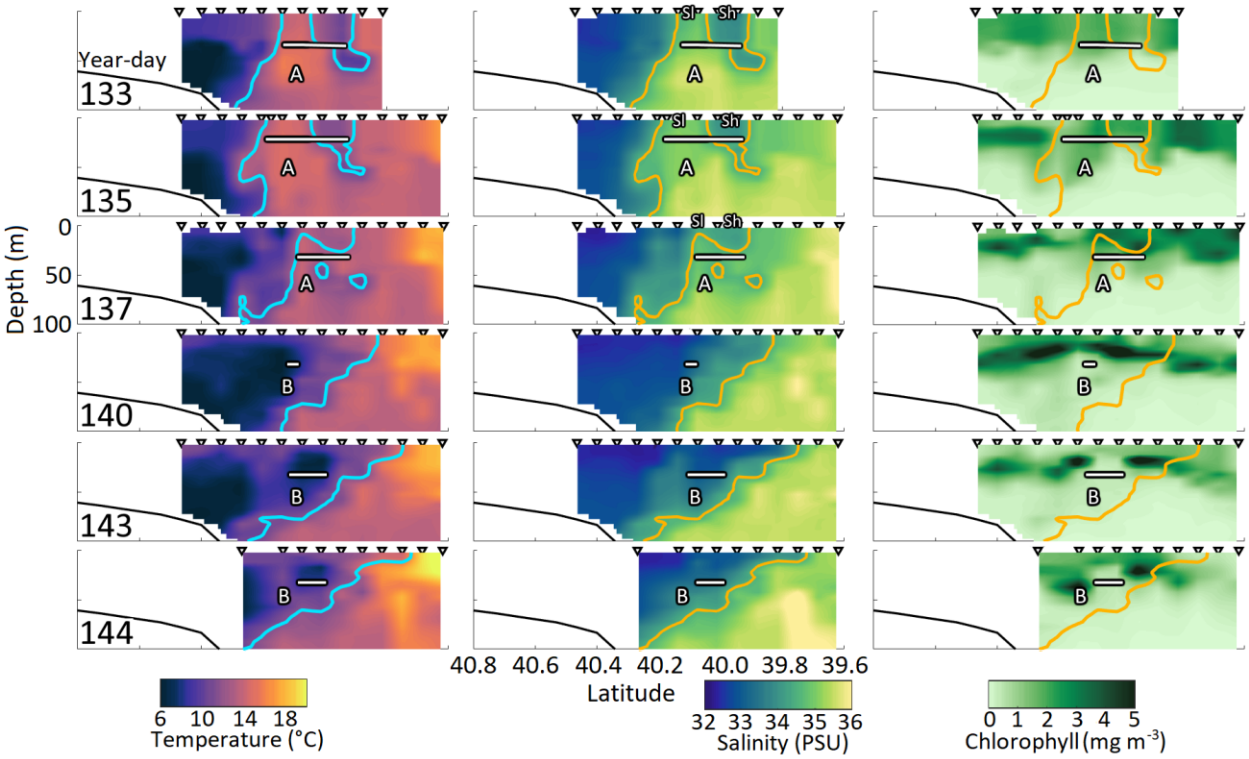


Figure 3.6: All individual transects used to create Eulerian mean plots (Figure 3.2) for May 2019. Stations sampled are denoted by triangles above plots. The 34.5 isohaline is represented by the teal and orange lines. Letters approximate the centers for frontal features A and B. The white lines at the bottom of each plot mark the extent of each feature within the transects. Letters denote which feature was observed during that transect. The letters “Sl” and “Sh” on salinity plots denote the slope and shelf water filaments respectively.

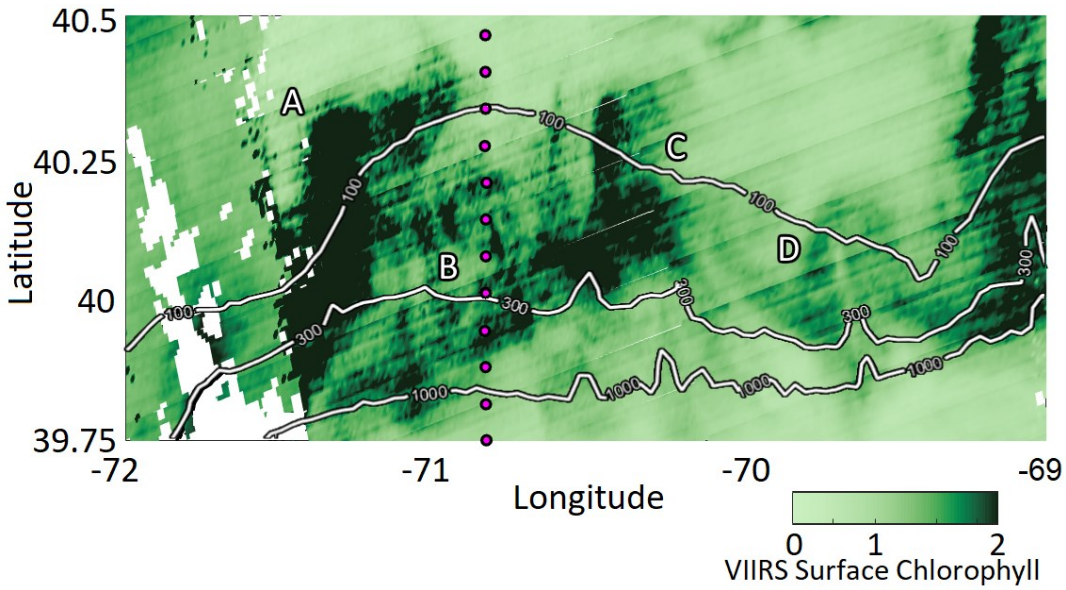


Figure 3.7: Surface chlorophyll for year-day 142. Transect stations are shown as magenta circles. Letters represent the approximate locations of features A and B, as well as two other features (C and D). White lines represent the 100, 300, and 1000m isobaths. The foot of the front is typically near the 100m isobath. Note the logarithmic spacing of the chlorophyll values in the color bar to better illustrate structure at lower chlorophyll concentrations.

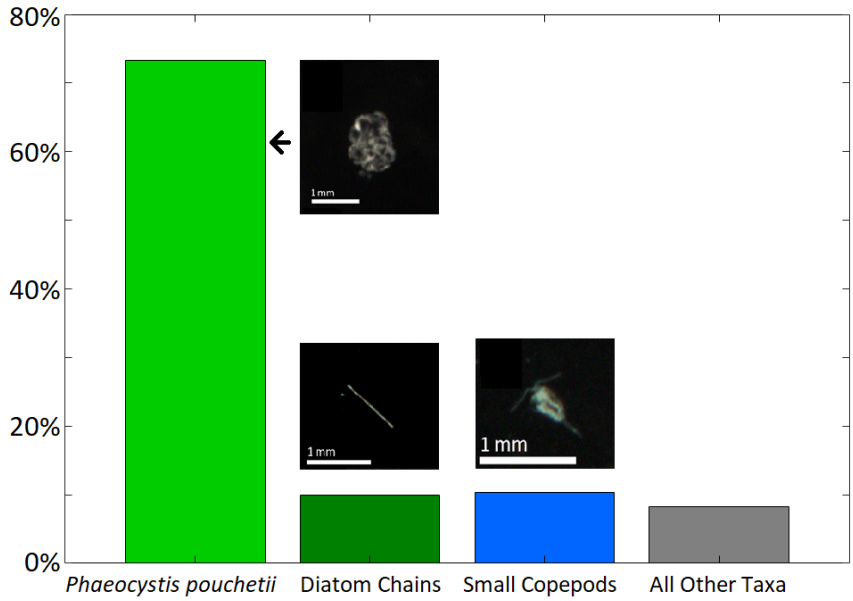


Figure 3.8: The relative proportion of ROIs from all three cruises that were classified as a given category. The rightmost, gray bar contains the combined number of ROIs that were classified as other categories. ROIs displayed are sample ROIs for each of the three predominant categories.

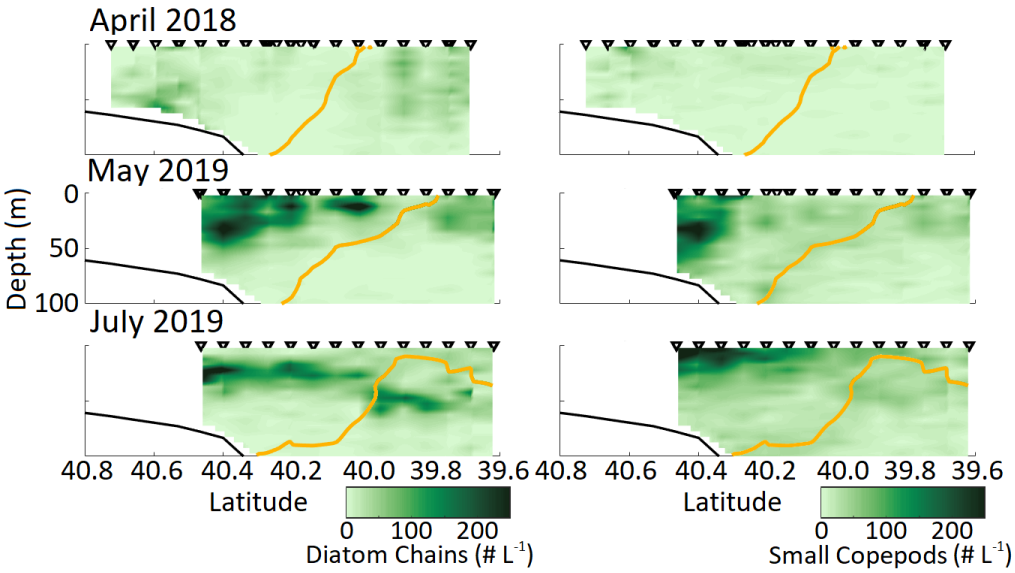


Figure 3.9: Eulerian means of the diatoms and small copepods for each of the three cruises. The orange line is the 34.5 isohaline. Station locations are denoted by the black triangles above the transect, though not all stations were sampled for each transect. Plots of the individual transects that were used to calculate Eulerian means are included as Supplemental Figures 3.6-3.8.

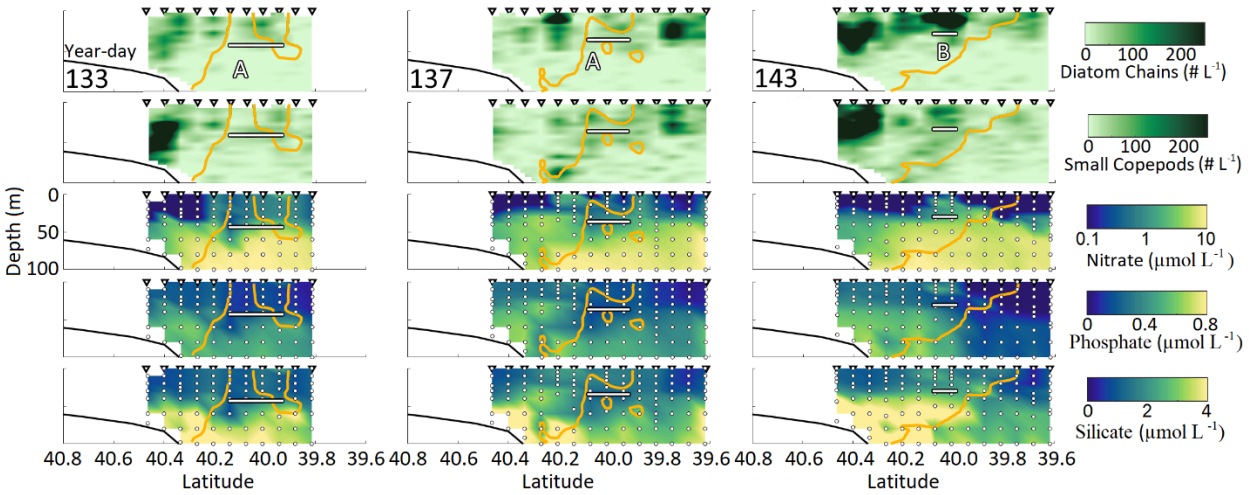


Figure 3.10: Individual transects for half of the transects for May 2019. Nitrate concentration is plotted on a nonlinear scale to highlight changes in surface concentration. The orange line is the 34.5 isohaline. Station locations are denoted by the black triangles above the transect. White dots represent the depths for which nutrient bottles were sampled, with the colors on nutrient plots being the interpolated depths as calculated for constructing Eulerian mean transect plots. The white lines at the bottom of each plot mark the extent of each feature within the transects. Letters denote which feature was observed during that transect.

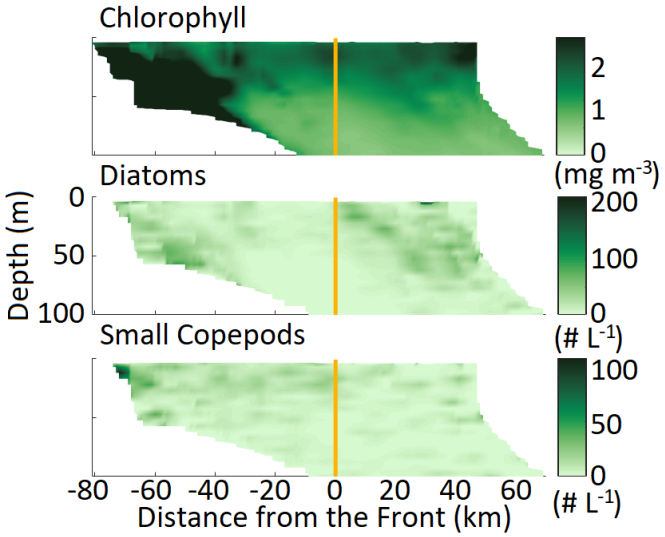


Figure 3.11: Frontal alignment means for April 2018 for chlorophyll, diatoms, and small copepods. The orange line represents the location of the 34.5 isohaline, which is identically zero.

## 3.7 Supplemental Figures

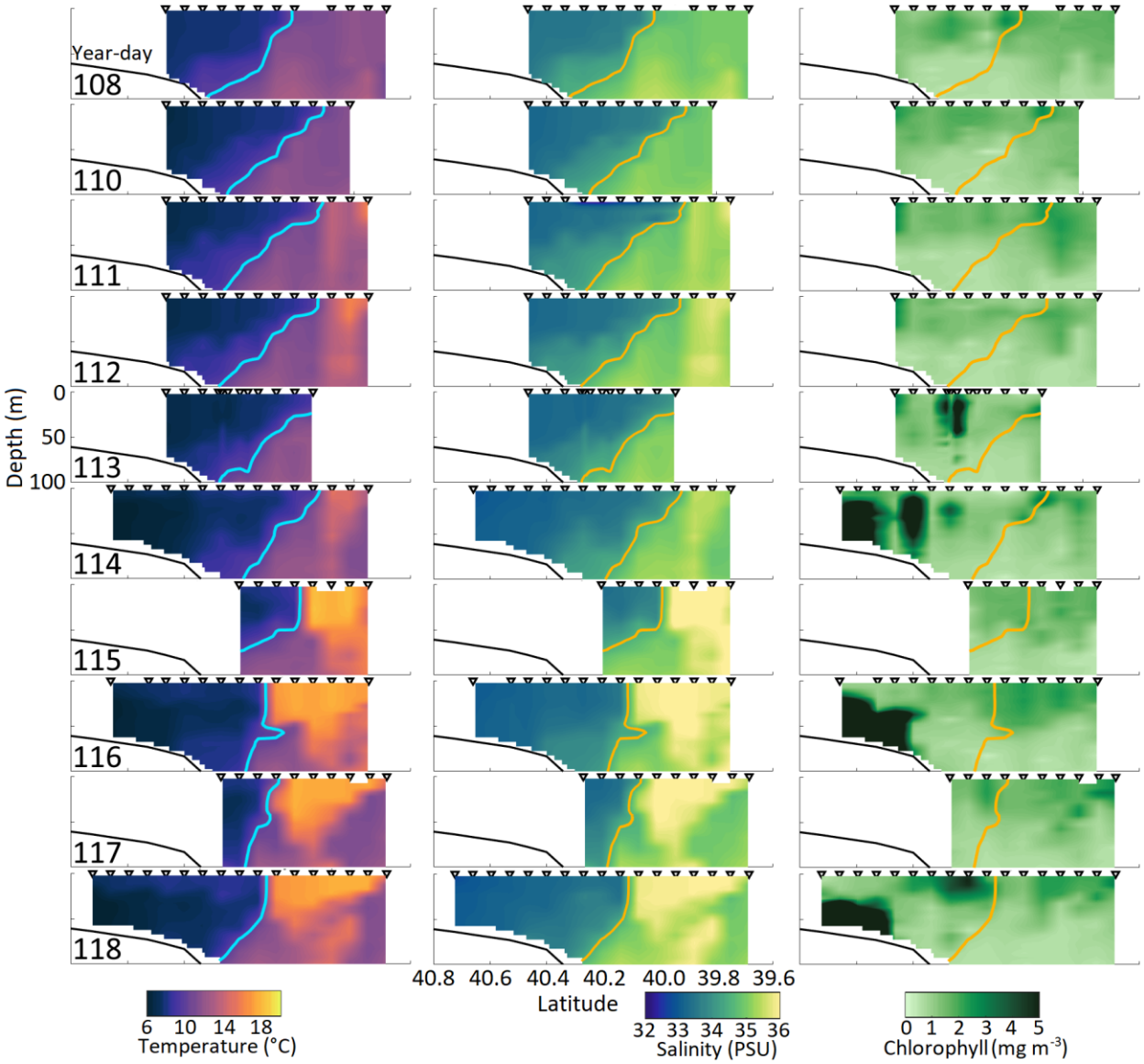


Supplemental Figure 3.1: All individual transects used to create Eulerian mean plots (Figure 3.2) for April 2018. The teal and orange line represents the 34.5 isohaline. Triangles above the transects represent stations sampled during that transect.

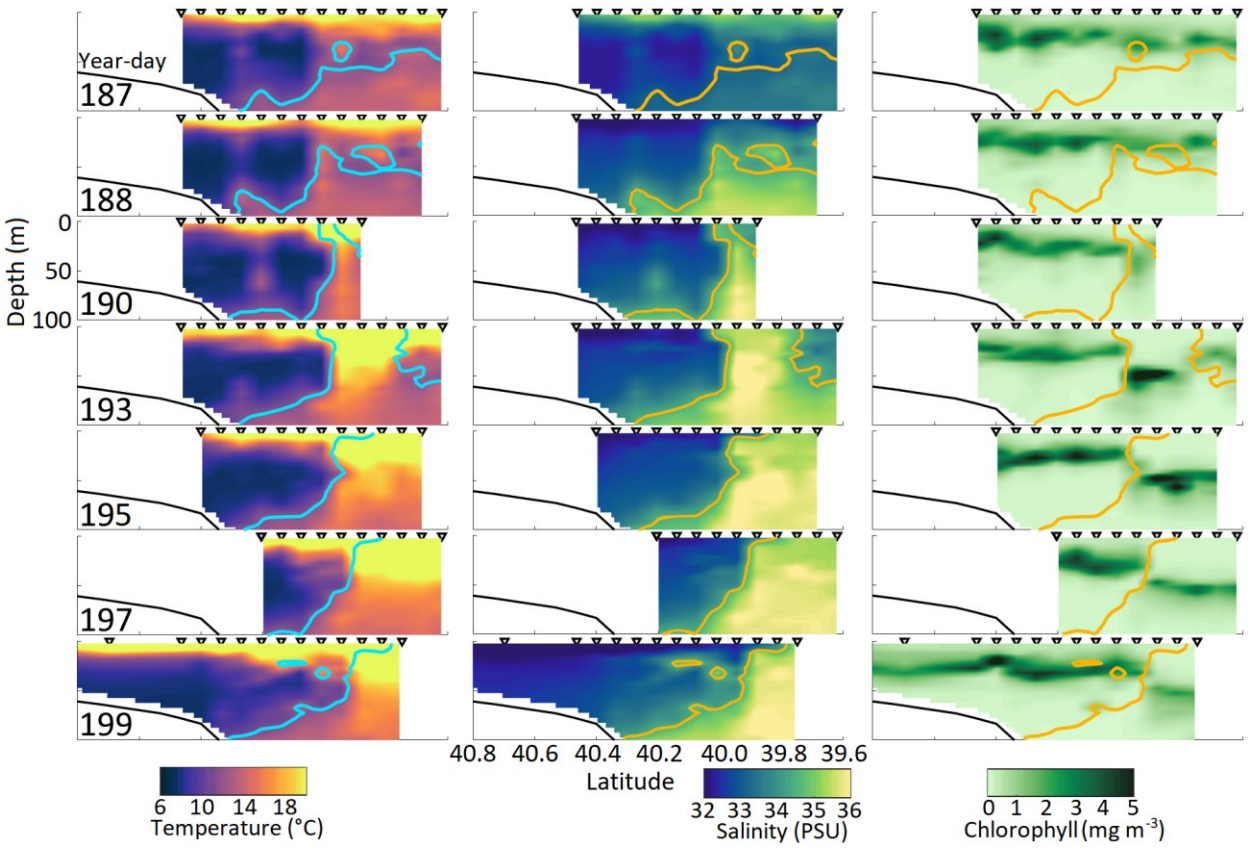


Supplemental Figure 3.2: All individual transects used to create Eulerian mean plots (Figure 3.2) for July 2019. The teal and orange line represents the 34.5 isohaline. Triangles above the transects represent stations sampled during that transect. The farthest north stations in Year-day 199 were not included in Eulerian means but are shown when in the domain of this study for completeness.

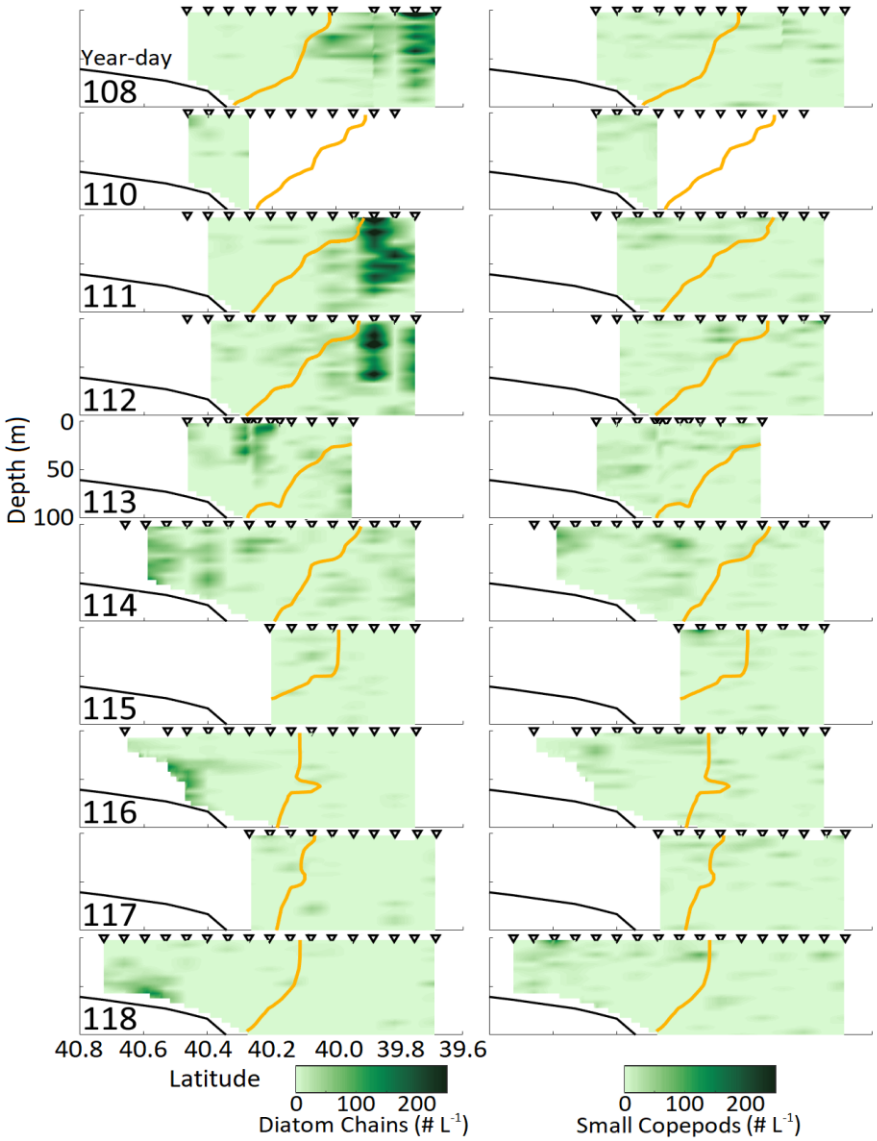


Supplemental Figure 3.3: All individual transects used to create Eulerian mean plots (Figure 3.9) for April 2018. The orange line represents the 34.5 isohaline. Triangles above the transects represent CTD stations sampled during that transect. Casts with triangles and no data indicate that the VPR did not sample during that cast.

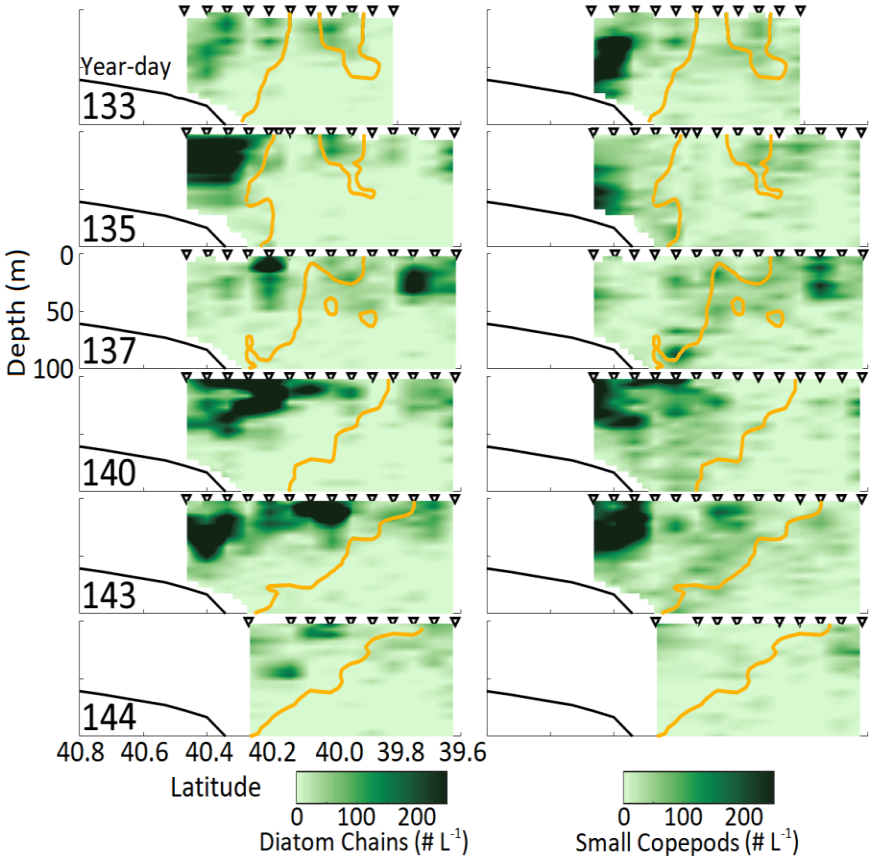


Supplemental Figure 3.4: All individual transects used to create Eulerian mean plots (Figure 3.9) for May 2019. The orange line represents the 34.5 isohaline. Triangles above the transects represent CTD stations sampled during that transect. Casts with triangles and no data indicate that the VPR did not sample during that cast.

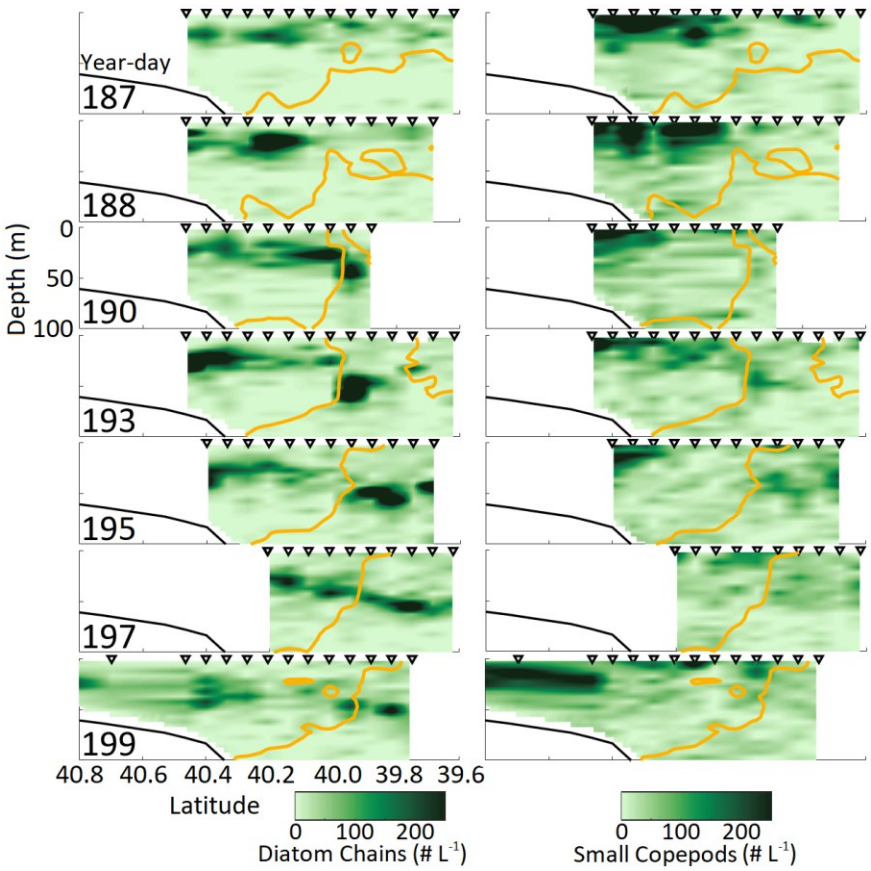


Supplemental Figure 3.5: All individual transects used to create Eulerian mean plots (Figure 3.9) for July 2019. The orange line represents the 34.5 isohaline. Triangles above the transects represent CTD stations sampled during that transect. Casts with triangles and no data indicate that the VPR did not sample during that cast. The farthest north stations in year-day 199 were not included in Eulerian means but are shown when in the domain of this study for completeness.

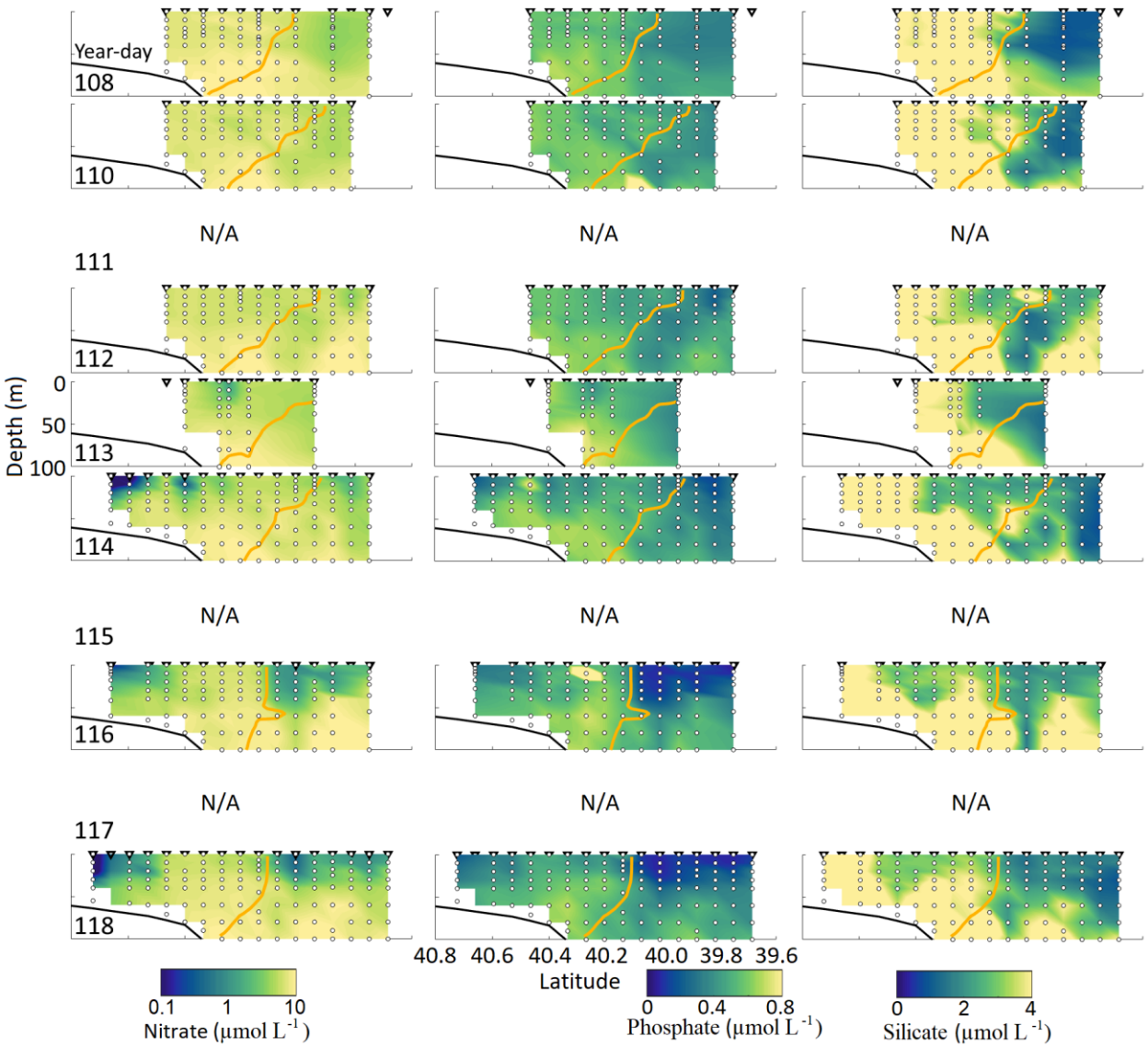


Supplemental Figure 3.6: All individual transects used to create Eulerian mean plots (Figure 3.2) for April 2018. Nitrate concentration is plotted on a nonlinear scale to highlight changes in surface concentration. The orange line is the 34.5 isohaline. Station locations are denoted by the black triangles above the transect. White dots represent the depths for which nutrient bottles were sampled, with the colors on nutrient plots being the interpolated depths as calculated for constructing Eulerian mean transect plots. Transects where nutrient data was not collected are labelled 'N/A'.

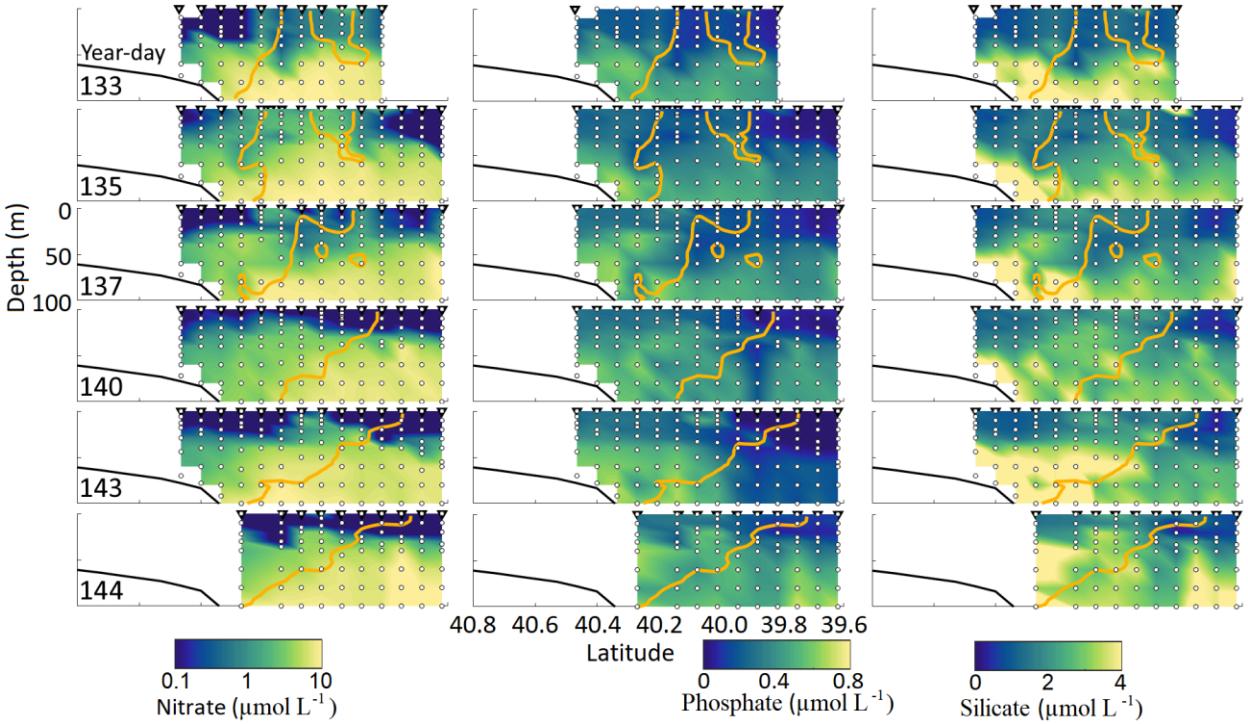


Supplemental Figure 3.7: All individual transects used to create Eulerian mean plots (Figure 3.2) for May 2019. Nitrate concentration is plotted on a nonlinear scale to highlight changes in surface concentration. The orange line is the 34.5 isohaline. Station locations are denoted by the black triangles above the transect. White dots represent the depths for which nutrient bottles were sampled, with the colors on nutrient plots being the interpolated depths as calculated for constructing Eulerian mean transect plots.

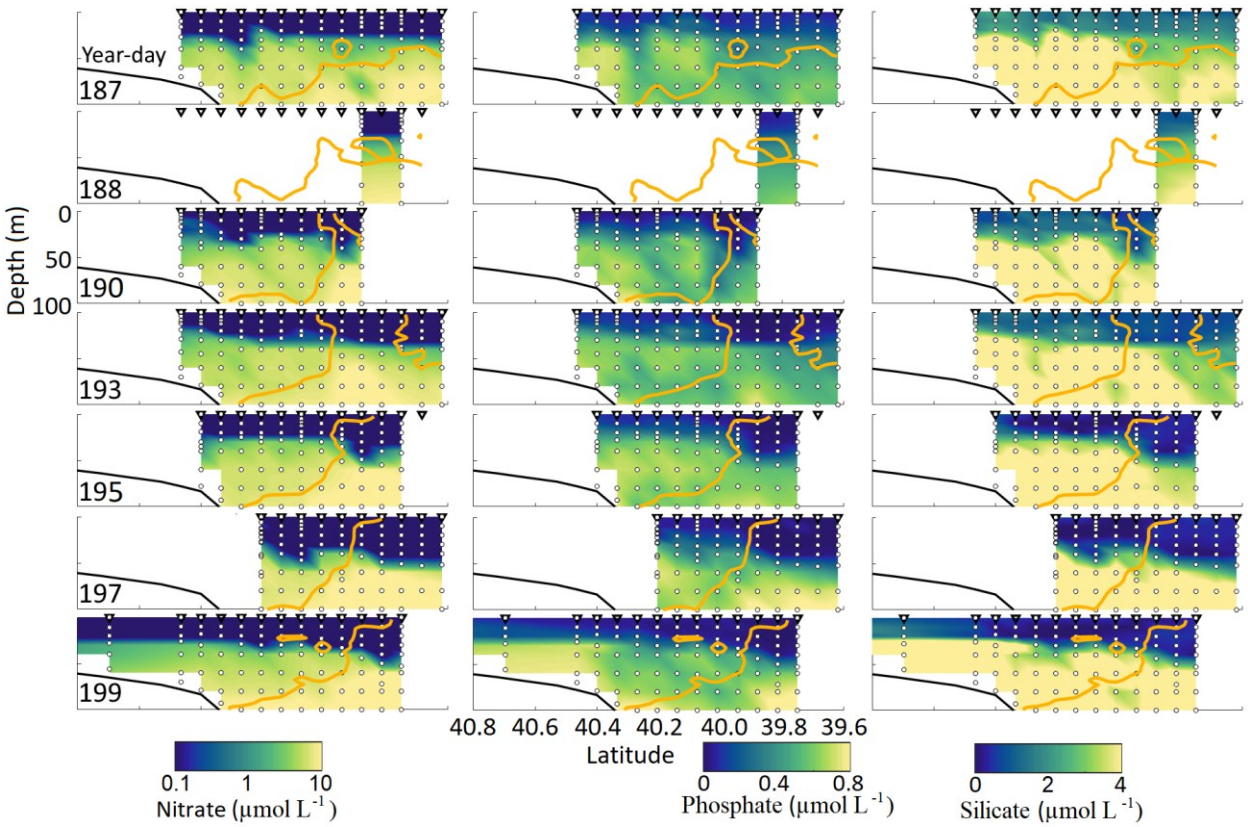


Supplemental Figure 3.8: All individual transects used to create Eulerian mean plots (Figure 3.2) for July 2019. Nitrate concentration is plotted on a nonlinear scale to highlight changes in surface concentration. The orange line is the 34.5 isohaline. Station locations are denoted by the black triangles above the transect. White dots represent the depths for which nutrient bottles were sampled, with the colors on nutrient plots being the interpolated depths as calculated for constructing Eulerian mean transect plots. The farthest north stations in Year-day 199 were not included in Eulerian means but are shown when in the domain of this study for completeness.

# Chapter 4

# Upwelling in Cyclonic and Anticyclonic Eddies at the Middle Atlantic Bight Shelf-Break Front

## 4.0 Abstract

This study investigates two types of frontal eddies, both observationally and with a model, to determine their kinematics and potential impact on biological processes. During May 2019, two eddies were observed *in situ* at the Mid-Atlantic Bight shelf-break front, which separates shelf water onshore from slope water offshore. The first was a cyclonic eddy, which contained a surface spiral of shelf and slope waters during formation. The second was an anticyclonic eddy characterized by a core of cold pool waters from the shelf side. Despite rotating in opposite directions, observations showed that both eddies had enhanced surface nutrients and chlorophyll. Eddy formation and upwelling were investigated with an idealized model. Modelled cyclonic eddies form as shelf waters are advected offshore and slope waters are advected shoreward. They form two filaments that spiral inward, with the size of the eddy increasing as the filaments are entrained. Rising isohalines and upwelled slope water dye tracer within the model suggest that upwelling coincided with eddy formation and persisted for the duration of the eddy. Modelled anticyclonic eddies form within troughs of the meandering shelf-break front, with amplified frontal meanders creating recirculating flow. Upwelling of subsurface shelf water occurs in the form of detached cold pool waters during the formation of the anticyclonic eddies. Our observations and model results indicate that both eddy types may persist for more than a month and upwelling in both eddy types may have significant impacts on biological productivity of the shelf break.

## 4.1 Introduction

The Middle Atlantic Bight (MAB) shelf-break front is characterized by its variability, with its physical, biological, and chemical attributes varying significantly in both time and space (Linder and Gawarkiewicz, 1998; Loder *et al.,* 2001; Zhang *et al.,* 2011). The front separates two water masses: cold, fresh shelf water inshore and warm, salty Slope Sea water offshore. In warm seasons (late spring to fall), a prominent body of near-bottom cold water – the cold pool – resides on the shelf side of the front and is bounded above by the seasonal thermocline (Lentz, 2017). Like many other oceanic frontal regions (*e.g.*, Munk *et al.*, 2000), eddies are common at the MAB shelf-break front. Satellite imagery frequently shows eddies arrayed across the extent of the shelf-break front, *e.g*., on May 1982 (Garvine *et al.*, 1988, Figure 1), May 1980 and 1984 (Ryan *et al*., 1999a, Figure 2), and May 1997 (Ryan *et al*., 1999b, Plate 1). These frontal eddies may be formed through frontal instabilities (Garvine *et al.*, 1988; Houghton *et al*., 1986) or generated by external forcing, such as Gulf Stream warm-core rings (*e.g.,* Kennelly *et al.,* 1985). Successive frontal meander troughs and crests may have completely different hydrodynamic balances (Pickart, 1999), which can result in mesoscale and submesoscale patches of high vorticity on either side of the shelf-break front (Zhang and Gawarkiewicz, 2015). These differing characteristics means that frontal meandering can lead to formation of eddies of varying rotational direction or water mass characteristics.

However, despite the ubiquity of eddies at the shelf-break front, direct observations of frontal eddies at the MAB shelf-break front are historically sparse, particularly when not influenced by Gulf Steam warm-core rings. Garvine *et al*. (1988) described two cyclonic slope water eddies, along with a possible offshore anticyclonic slope water eddy. Both of the cyclonic eddies were observed drawing shelf water offshore, across the front. Houghton *et al.* (1986) also

observed a shelf water filament being drawn offshore, which instead formed an anticyclonic shelf water eddy seaward of the front. Gawarkiewicz *et al*. (2001) observed an anticyclonic slope water eddy, which was estimated to contain variable upwelling and downwelling. Flagg *et al.* (1997) observed a series of anticyclonic "cold pool" eddies, which were associated with increased chlorophyll. Frontal eddies have long been recognized as an important vector for cross-frontal water exchange, during which they may also upwell nutrients and impact local productivity.

This study investigates two types of frontal eddies: a cyclonic eddy and an anticyclonic eddy originating on opposite sides of the front. Satellite imagery and *in situ* observations are used to track the eddies over time. Model results are then used to investigate the morphological evolution of the eddies and then upwelling within the eddies, with the intent of determining the possible impact of frontal eddies on biological processes.

## 4.2 Methodology

Direct observations of two eddies occurred during a two-week cruise in May of 2019 (*NOAAS Ronald H. Brown* voyage RB19-04, May 12-25). Sampling was primarily along a cross-shelf transect south of Cape Cod, MA. Additional measurements were collected during departures from the transect line to track the eddies. The 34.5 isohaline was used to identify the location of the shelf-break front, following the convention of previous studies (*e.g.,* Linder and Gawarkiewicz, 1998).

Station profiles were measured by a Seabird SBE 911+ (conductivity, temperature, and pressure) and a WetLabs FLNTURTD fluorometer (chlorophyll fluorescence) mounted upon a rosette. Seawater samples were taken at discrete depths with 24 10L Niskin bottles mounted on

the rosette. Nitrate, phosphate, and silicate concentration in samples were processed in the Woods Hole Oceanographic Institution Nutrient Analytical Facility. Plankton were imaged with a Digital Auto Video Plankton Recorder (DAVPR, from SeaScan Inc.) mounted upon the CTD rosette. The DAVPR included a Seabird Electronics Inc. CTD (SBE 49 FastCat), fluorometer (FLNTURTD-4620), and synchronized video camera and xenon strobe (Davis *et al*., 2004). Both CTD and DAVPR measurements were averaged into 1 m depth bins. DAVPR video frame frequency and dimensions were 20 Hz and 1392 x 1040 pixels (~10 x 7 x 25 mm volume imaged) respectively. Higher resolution physical and biological parameters were sampled with a towed Video Plankton Recorder II (VPRII, from SeaScan Inc.). The VPRII consists of a towed body, containing a Seabird Electronics Inc. CTD (SBE 49 FastCat), oxygen sensor (SBE 43), fluorometer (ECO FLNTU-4050), ECO Triplet (ECO BBFL2-123), PAR (photosynthetically active radiation; Biospherical Instruments Inc. QCP-200L), and synchronized video camera and xenon strobe (Davis *et al*., 2005). The VPRII was towed at 10 knots (5.1 m $s^{-1}$), undulating between depths of 5m and 100m approximately every 6 minutes. Plankton video frames for the DAVPR and VPRII were captured at 20 Hz and 30 Hz respectively. DAVPR video frame dimensions were 1392 x 1040 pixels (~10 x 7 x 25 mm volume imaged) and VPRII video frame dimensions were 1380 x 1034 pixels (~20 mm x 15mm x 23 mm volume imaged). Individual video frames from both instruments were passed through object identification software to identify "regions of interest" (ROIs), which were then saved to disk with a time-stamp naming convention (Davis *et al*., 2004). ROIs were manually annotated to the highest level of taxonomic identification possible based on imagery alone. Herein we focus our analysis on the most abundant categories (*i.e.,* diatom chains, small copepods). Manually annotated DAVPR ROIs are used for all diatom and copepod results presented in the figures of the main body of this chapter.

VPRII planktonic results are only shown in supplemental material (*i.e.,* Supplemental Figure 4.5). VPRII ROIs were classified using a convolutional neural network, described in more detail in Chapter 2.

### *4.2.1 Model Description*

This study used an idealized 3-dimensional frontal model developed by Zhang and Gawarkiewicz (2015) to provide insight into the behavior of both types of frontal eddies. Briefly, the model was based on the Regional Ocean Modeling System (Shchepetkin and McWilliams, 2008). The model domain was rectangular, with the span of 2010 and 479 km in the along-shelf (x) and cross-shelf (y) directions, respectively. Bathymetry was uniform in the along-shelf direction and varied only in the cross-shelf direction. The model had a horizontal resolution of 500 m and 60 vertical layers. Temperature and salinity were initialized based on wintertime climatological conditions in the New England shelf-break region. The initial velocity field was thermal-wind balanced with zero bottom velocity. This yielded a shelf-break front with strong gradients in both temperature and salinity, as well as a westward frontal jet in the model initial condition (Figure 4.1). This climatology was persisted along the upstream (eastern) boundary. Throughout the integration, the eastern 700 km of the model domain was nudged to these same climatological conditions in order to maintain a steady inflow. The western, downstream boundary was left open, which, combined with a 156-km-wide offshore deep-sea region acting as a sponge layer, acted to prevent wave reflection. Results were analyzed in a 250x60 km interior subdomain, far enough removed from the boundaries for the solution to evolve freely.

Meteorological conditions observed at the New England shelf break in April to May 2018 were used to perturb the front and were applied in a spatially uniform manner. Air temperatures

below 10°C were increased by 10°C in order to remove surface-cooling-induced convective mixing that did not occur in the ocean during our cruise period. Two subsurface dyes were introduced within the model domain at the beginning of the simulation, one inshore and one offshore of the shelf-break front, to represent shelf and slope waters respectively (Figure 4.1). To examine frontal upwelling, dye concentrations in the top 100 m were initialized to be the same values as the depth, *i.e.,* concentrations increased linearly from 0 at the surface to 100 at 100 m. Below 100 m, dye concentrations were initialized at 100. During model evolution, vertical mixing of the dyes was turned off. Because the numerical mixing is negligible during the short-term simulation, changes in modelled dye distribution were caused mostly by horizontal and vertical advection. Therefore, upwelling and downwelling were indicated at any locations where a dye concentration was greater or lesser than the initial value at a specified depth respectively. Shelf dye and slope dye were separated by the 34.5 isohaline. To avoid sharp gradients in the dye concentrations, the frontal transitions of both dyes were smoothened within a cross-shelf distance of 10 km.

## 4.3 Results

Two frontal eddies were evident in our *in situ* observations: Eddy A, a cyclonic eddy that was located seaward of the shelf-break front, and Eddy B, an anticyclonic eddy that was located shoreward of the front (Table 4.1, Figure 4.2). Eddy A was characterized by a surface spiral pattern, formed of two filaments, one originating from shelf waters and one from slope waters (Figure 4.2 left column, Supplemental Figure 4.1). The filament of warm and salty slope water originated from the southeast of our transect (Figure 4.3, year-days 129 and 131). This slope water filament extended northwestward to the north of a cold and fresh shelf filament extending

southeastward from shelf waters. Both of these filaments extended to roughly 50m in depth and were located above deeper slope waters (Figure 4.2, Figure 4.4). When last sampled (Figure 4.5), both filaments had coalesced. Coalesced waters were relatively cooler and fresher at the surface and became warmer and saltier with depth. This coalescence, combined with frequent cloud cover, prevented distinguishing of Eddy A from surrounding slope waters in subsequent satellite observations. Satellite SST showed approximately 10 days passed between when the slope filament began to extend inshore and when the shelf and slope filaments coalesced (Figure 4.3). Velocities in the eddy region were strongest in the east-west direction, with weaker north-south velocities while forming (Figure 4.4 third and fourth rows) and after the cyclonic eddy had formed (Figure 4.5). Nutrient enhancement was observed in the surface layer of the eddy compared to surrounding waters for nitrate (Figure 4.2, 4.4), phosphate, and silicate (Supplemental Figure 4.4), implying upwelling. The nitracline within the slope filament is depressed compared to surrounding waters, which may reflect either mid-depth downwelling in the slope filament, or simply variation in the vertical distributions of nutrients in the different water masses. Surface nitrate declined after coalescence, but was still elevated relative to surrounding waters (Figure 4.5). Chlorophyll inside the eddy was similar to surrounding concentrations initially, but was enhanced within both filaments by year-day 137 (Figure 4.4 fifth row). Chlorophyll was highest within the eddy once the filaments had coalesced (Figure 4.5). Diatom chains measured with the VPR were primarily associated with shelf waters, *i.e.,* the shelf filament (*e.g.,* year-day 135) (Figure 4.4 seventh row, Supplemental Figure 4.5 first column) and surface waters after coalescence (Figure 4.5). Small copepod abundance was more variable, but roughly mirrored diatom distributions and was enhanced within eddy center after coalescence (Figure 4.4 last row, Supplemental Figure 4.5 second column).

Eddy B was primarily characterized by a core of cold pool waters surrounded by relatively warmer, saltier shelf waters more characteristic of waters typically found closer to the shelf-break front (Figure 4.2 right column, Figure 4.6). A thin lens (~10m) of warmer waters at the surface covered the deeper, colder waters in all transects. Eddy B had little surface expression in satellite imagery as a result (Figure 3), but could be delineated to the east by a relatively warm filament of near-frontal warmer and saltier shelf waters intruding into the surrounding cooler shelf waters. This filament began extending westward from year-day 141 along the northern boundary of Eddy B until it was last distinguishable in satellite imagery on year-day 144 (Figure 4.3, Supplemental Figure 4.1). Slope waters bounded Eddy B to the west. To the south, Eddy B was bordered by warmer, saltier shelf waters, which extended roughly 10-20km southward before reaching the front for the duration that Eddy B was observed (Figures 4.2, 4.6; Supplemental Figure 4.2). The warm and salty shelf waters to the south of the eddy were roughly 30m in depth, overlaying slope waters and located between the cold pool core of Eddy B and the front. The vertical extent of these waters declined to roughly 15m depth by year-day 144 (Figure 4.6) as these waters moved west (Figure 4.3). Like Eddy A, east-west velocities associated with Eddy B were larger than the north-south component (Figure 4.6 third and fourth rows). A VPRII survey of Eddy B on year-day 143 revealed a longitudinal extent of over 20km, with a latitudinal extent of roughly 10 km (Figure 4.7). Like Eddy A, Eddy B contained enhanced nutrients in its center (Figure 4.6 sixth row). Unlike Eddy A, chlorophyll was highest within the periphery of Eddy B (Figure 4.6 fifth row), in the warmer and saltier shelf waters present both to the north and to the south of eddy center. Diatoms and copepods measured by the VPR were both highest within the center of Eddy B (Figure 4.6 last two rows, year-days 143-144).

Both eddies appeared to have formed at the front. Neither eddy crossed the shelf-break front while observed *in situ* or through satellite imagery. Both eddies stayed near the front for the duration of the cruise.

### *4.3.1 Model Output and Interpretation*

The simulation was able to replicate features similar to those of Eddy A and Eddy B (Figure 4.8). Four eddies similar to Eddy A and three eddies similar to Eddy B (Eddies A1-A4 and B1-B3 respectively) were identified and followed over time. Model eddies of each type were qualitatively similar, and so only one model eddy of each type (A2 and B2) will be discussed in detail herein. Formation of a shallow mixed layer, composed of primarily shelf waters over slope waters, occurred during the initial slumping of the shelf-break front (prior to model day 10) due to offshore Ekman transport driven by eastward winds. This change does not appear to influence formation of either type of eddy or surface spiral patterns similar to those observed in Eddy A. The primary impact of this layer is that surface salinities are lower than would be expected, such that what we refer to as a "slope water filament" has salinities of less than 34.5 within the mixed layer. For ease of interpretation, we will primarily focus on interpretation of model output below this mixed layer (*i.e.*, at 30m in depth).

The model Eddy A2 develops similarly to that of our observed Eddy A (Figures 4.8, 4.9, 4.10, Supplemental Figure 4.6). Eddy A2 begins forming after frontal meanders have formed (Figure 4.9 first row, Figure 4.10 column 1). Increased frontal meander amplitude causes the front to roll over, advecting slope water onshore and advecting shelf water offshore (Figure 4.9 second row, Figure 4.10 column 2). As time passes, the front continues to roll up, causing both filaments to continue spiraling inward (Figure 4.10 column 3). As more shelf and slope waters

spiral inward, the two filaments get increasingly thin and increase the size of the eddy with the entrained fluid (Figure 4.9 third row, Figure 4.10 column 4). Eddy A2 continues to be visible for the duration of the simulation (60 days) and forms subsequent spirals. Spiral creation time is approximately equal to that of observations, with the first two sets of spirals forming and evolving over the course of 12 model days and 10 model days respectively.

Upwelling of slope water dye starts at the front to the west of Eddy A2 (model day 10, Figure 4.10 third row, Supplemental Figure 4.6 second row). Shelf water is entrained from the western side of the eddy and slope water is entrained from the eastern side, developing into a clear spiral pattern (Figure 4.10, model days 16-22). Slope dye concentrations within the eddy increase over time indicating that deeper slope waters are entrained with the movement of shelf waters. The upwelling flow intensifies as the frontal meander increases in magnitude. Isohalines at eddy center rise and stay domed throughout the spiral and eddy formation (Figure 4.10, fourth row). Shelf water dye is not elevated within shelf filaments or the eddy beyond concentrations expected by horizontal advection (not shown), indicating that upwelling is predominately of deeper slope waters within Eddy A2 (Figure 4.10, last row). For a fixed volume, continuity would imply that inward-spiraling filaments should yield downwelling within eddy center, but we saw no evidence of systematic downwelling in the eddy (Supplemental Figure 4.6). Instead, the size of Eddy A2 increases as upwelled fluid is entrained, and that appears to counterbalance any downwelling implied by an inward spiral.

Model eddies A1 A3, and A4 mostly vary from Eddy A2 in terms of quantity of shelf water advected, which then alters the shapes of the developing spirals and eddies (Figure 4.8). Little is affected regarding the occurrence, date, or duration of formation of either the initial spiral patterns or later formation of the cyclonic eddies. Subsequent spirals were observed

forming associated with meander crests – during the one instance where an eddy departed from the meander crest (Figure 4.8, Eddy A3, model day 19), the eddy resulting from the previous spiral was entrained by the newly forming spiral pattern (model day 22). After this, Eddy A3 remained within the meander crest and formed subsequent spirals, similar to Eddies A1, A2, and A4.

The model Eddy B2 is similar to what we observed for Eddy B, in that it is an anticyclonic eddy with upwelling flows and a core of cold pool waters (Figures 4.8, 4.9, and 4.11). Eddy B2 formation begins within the frontal trough between Eddies A2 and A3 (Figure 4.9 first row, Figure 4.11 first row). As the meanders increase in amplitude (Figure 4.11 column 4.2), irregularities within the front result in the frontal jet travelling more northward (Figure 11 column 3), which later results in shelf waters traveling to the east (Figure 4.9 second row, Figure 4.11 column 4). Velocities are initially variable in depth and intensity. Over time, a more coherent flow develops, creating an anticyclonic eddy, with velocities extending throughout the upper 100-150m of the water column (Figure 4.9 third row, Figure 4.11 column 5). Once this has occurred, Eddy B2 decouples from surrounding eddies (*i.e.,* leaves the trough between cyclonic eddies) and travels along the front. Eddy B2 travels westward more rapidly than model eddies A1-A4, and is to the immediate north of Eddy A2 on model day 39 (Figure 4.8 last row, Figure 4.11 column 5). Unlike Eddy A2, upwelling was not continuous during and after eddy formation. Instead, a parcel of cold pool water rises along the front into the developing meander, which is then separated from inshore shelf waters as Eddy B2 forms (Figure 4.9 right column, Figure 4.11 last row). Once the parcel of cold pool water detaches from its origin, the encircling warmer and saltier waters prevent replenishment or further enhancement.

Model features similar to Eddy B did not all persist on the same side of the shelf-break front as they formed, unlike Eddy A (Figure 4.8). Modelled Eddy B2, described above, is the most similar to the observed Eddy B, in that it remained near to the front and seaward of the front. Modelled Eddy B1 also formed a persisting anticyclonic eddy with detached cold pool waters in its core, but it travels across the front post-formation. Eddy B1 then proceeds farther south into the Slope Sea, possibly as a result of Eddy A2 being in close proximity to the immediate east of Eddy B1. The salinity is also higher within Eddy B1 compared to Eddy B2. Eddy B3 never intensifies into a full eddy, nor do its core cold pool waters fully detach from inshore waters. This incomplete formation is likely due to both forming in a shallower frontal trough and the presence of a cyclonic shelf water eddy nearby. The end result is that Eddy B3 is transient, unlike the other model eddies.

## 4.4 Discussion

### *4.4.1 Eddy A*

Our model eddies A1-A4 replicated surface spiral patterns that developed similarly to those observed in SST observations and replicated cross-shelf profiles similar to those measured *in situ* for Eddy A. Both the simulation and observations also contained evidence of upwelling. Simulation isohaline doming and upwelling of slope water dye coincided with formation of a visible spiral pattern (Figure 4.10 first and second columns). Because slope water dye distributions were unaffected by explicit mixing, the presence of elevated slope water dye concentrations within the upper 30m indicates upwelling. Nitrate, phosphate, and silicate were elevated in surface waters within Eddy A relative to surrounding waters when first measured on year-day 133 (Figure 4.4, Supplemental Figure 4.4), which is consistent with upwelling.

Isohaline doming was observed after both filaments had coalesced, on year-day 138 (Figure 4.5), indicating that upwelling was occurring within Eddy A. Spiral formation had already begun by year-day 131 (Figure 4.3). Provided that Eddy A followed a similar timeline as our simulation, between 2-8 days of upwelling had occurred prior to our first transect, increasing the likelihood that the elevated surface nutrients observed in Eddy A were due to upwelling.

Chlorophyll was initially equal throughout both filaments of Eddy A when first observed on year-day 133 (Figure 4.4 fifth row). Chlorophyll concentrations increased with time, with elevated chlorophyll within the shelf water filament on year-day 137 and above eddy center on year-day 138 (Figure 4.5). Diatom and copepod abundance were initially higher within the shelf water filament than the slope water filament, likely due to being advected from inshore shelf populations (Figure 4.4, last two rows). Both diatom and copepod abundance were highest on year-day 138, within the center of Eddy A (Figure 4.5). Surface nitrate, phosphate, and silicate concentrations were lower within the center of Eddy A on year-day 138 compared to previous transects (Figure 4, Figure 5, Supplemental Figure 4.4), coinciding with the increase in chlorophyll, diatoms, and copepods. Combined with the doming isohalines and earlier surface nutrient enhancement during Eddy A formation, it is plausible that we observed upwelling-caused nutrient enhancement, followed by a biological response.

The subduction of shelf filament waters observed *in situ* (Figure 4.2, 4.4, and Supplemental Figure 4.2) were not evident in our model results. The subduction of shelf waters was observed on our transect on year-days 133 through 137 (Figure 4.4). A deep lens of cool, fresh water surrounded by slope waters was seen as late as year-day 139, after contact with the surface had ended (Supplemental Figure 4.2). Our simulation does not resolve the subduction, which may have been caused by the presence of the surface mixed layer or the relatively low

vertical resolution in the model. The model vertical layers at the observed depth range of the subducted shelf water have a thickness of 7-8m, which is similar to the thickness of the subduction layer. Observed subducted waters persisted after Eddy A migrated westward and covered relatively large areas (Supplemental Figure 4.2 year-day 139). The subducted shelf waters were not mixed with slope waters, unlike the shelf and slope filaments which constituted Eddy A's spiral and which coalesced within Eddy A. Since both observed Eddy A and model Eddy A1-A4 remained close to the front without crossing the front, it seems that subduction of shelf waters may be important for cross-shelf exchange.

Garvine *et al*. (1988) observed two cyclonic slope water eddies similar to that of Eddy A. Each cyclonic slope eddy was bordered by a shelf filament to west and south. Both eddies were adjacent to each other, similar to those in our model. The horizontal and vertical extent of both eddies and accompanying shelf filaments were comparable to those observed in this study. The described timeline of their features matched our own, with their transects and SST observations showing similar patterns to our transects for year-days 133 and 135 (Figures 4.3, 4.4). Garvine *et al*. (1988) noted that the region of the shelf-break front to the east of their study region contained no eddies, but did contain frontal meanders. As the front travelled westward, meanders increased in amplitude, culminating in the observed shelf filaments. Garvine *et al*. (1988) concluded that formation of the shelf filaments contributed to the formation of the cyclonic slope water eddies, in that shelf water was moving offshore and wrapping around slope water. This conclusion is similar to that which we have observed and modelled with no major discrepancies. No full spiral or mixing was observed *in situ*, but their regional satellite imagery (Garvine *et al.,* 1988 – Figure 1) show a few spiral-like features within the MAB. Therefore, frontal eddies similar to Eddy A have been observed in the past at the MAB shelf break. In a broader sense, Eddy A is similar to

those observed in frontal spiral eddies elsewhere (*e.g.*, Munk *et al*., 2000), following a general pattern of shear instability and baroclinic processes within fronts creating spiral eddies.

Houghton *et al.* (1986) also observed formation of a frontal slope water eddy with a spiral pattern. However, their eddy was anticyclonic, different from Eddy A observed in this study and those in Garvine *et al.* (1988). Formation of the eddy based on satellite imagery (Houghton *et al.,* 1986 – Figure 5) showed a shelf filament extending offshore and westward. They argued that frontal baroclinic instability was responsible for the formation of the eddy. However, Houghton *et al.* (1986) noted that a Gulf Stream warm-core ring had recently passed through the region, which may have resulted in the formation of the anticyclonic eddy through instability of the remnant westward flow within the Slope Sea.

Another anticyclonic slope water eddy was observed by Gawarkiewicz *et al*. (2001). Gawarkiewicz *et al*. (2001) did not observe any spiral pattern in the eddy, but did observe the eddy remaining close to the shelf-break front. Both frontal eddies observed during our cruise and the majority of simulated frontal eddies within this study exhibited this behavior.

### *4.4.2 Eddy B*

Our modelled eddies B1-B3 qualitatively reproduce formation of anticyclonic flow around a center of cold pool water as measured in Eddy B. Both observed Eddy B and modelled Eddy B1-B3 showed evidence of upwelling of cold pool waters. Upwelling within model eddy B2 is shown by a mass of detached cold pool water (Figure 4.9 right column, Figure 4.11 bottom row). Upwelled shelf dye is originally unevenly distributed due to frontal variability, but is later clearly detached from inshore waters and located within the core of the eddy and nearer to the

surface. We observed enhanced surface nitrate, phosphate, and silicate within eddy center of Eddy B, which is consistent with upwelling (Figure 4.6, Supplemental Figure 4.4).

However, we observed a less clear biological response. Chlorophyll was enhanced in the periphery of Eddy B, and VPR-measured diatoms and copepods concentrations were higher within eddy center for the duration of our measurements (Figure 4.6). The lack of elevated chlorophyll in the center of Eddy B may have been caused by sustained high grazing on phytoplankton smaller than the diatom chains resolved by the VPR, as our observation likely occurred during a late stage of the biological response in Eddy B. Other possible reasons for the separation between observed chlorophyll enhancement and elevated diatom abundance within Eddy B include that the diatoms imaged by the VPR (>100μm in diameter) were a small percentage of overall chlorophyll and that the diatoms observed had higher carbon:chlorophyll ratios compared to phytoplankton in the periphery. Observations also showed higher abundance of diatoms and copepods further inshore than in the center of Eddy B. Therefore, both may be more abundant in the center of Eddy B as a result of advection from inshore. Another possible explanation for the higher copepod abundance within the center of Eddy B is due to aggregation.

The closest literature example of eddies similar to our observed Eddy B is from Flagg *et al*. (1997). Multiple cold pool-associated anticyclonic eddies were observed further south in the MAB compared to our study site, near Cape Hatteras. These eddies contained a layer of cold pool waters in the upper 50m of the water column, with additional deeper anticyclonic velocities. Flagg *et al.* (1997) noted that such eddies could not be formed locally, due to constraints in local bathymetry and hydrographic characteristics, and so must have travelled a significant distance from the north. Both higher chlorophyll-normalized primary productivity and higher oxygen saturation were measured within one of the eddies compared to surrounding shelf waters, with

Flagg *et al.* (1997) hypothesizing that a nutrient-enhanced bloom had occurred 1-2 weeks prior to observation. Chlorophyll was locally high on the periphery of the observed eddy, similar to what we observed in Eddy B. While much farther south than our study location, the characteristics of their eddies match our own. We have described herein a method for forming similar eddies with upwelled nutrients, which may persist for significant periods of time. The eddies observed by Flagg *et al.* (1997) did not cross the front, but did serve as a mechanism for southward movement of cold pool water. This could have implications for the eventual fate of such eddies, perhaps as a mechanism to preserve upstream water characteristics while the frontal eddies move downstream along the front. Additionally, the eddies observed by Flagg *et al.* (1997) were highly productive, indicating that our observed anticyclonic eddies could be similarly productive.

Historic satellite imagery of our section of the MAB (Garvine *et al*., 1988 – Figure 1) shows at least one feature that appears to have a filament of warmer waters (frontal or slope in origin) wrapping anticyclonically around shelf water, similar to that of our model Eddy B2. Our model results, as well as the observations of repeated anticyclonic cold pool eddies by Flagg *et al.* (1997), imply that features similar to Eddy B should be relatively common along the shelf-break front. Model Eddy B1 crossed the front into the Slope Sea and model Eddy B2 drew near-frontal water inshore away from the front, indicating that eddies similar to Eddy B may contribute in multiple fashions to cross-frontal water exchange.

### *4.4.3 Relation to Frontal Instabilities*

Formation of Eddy A and Eddy B are related to frontal instabilities. This study has primarily focused upon descriptive analysis of observations and model results rather than the

mechanisms generating frontal instabilities and the specific conditions necessary for frontal instabilities to develop into the features presented herein. Frontal meanders within the MAB shelf-break front are known to generate frontal instabilities with patches of high and low vorticity on either side of the front (Zhang and Gawarkiewicz, 2015), causing both upwelling and downwelling near the front. Nutrient-rich water upwelled by frontal meanders could potentially increase nutrient availability during eddy formation. Model eddies similar to Eddy B showed patchy shelf water dye distributions prior to eddy formation as a result of frontal variability (Figure 4.11), which upwelled shelf water dye prior to detachment of cold pool waters. However, the connections between those submesoscale processes and enhancement of nutrients on the scale of eddies are not known. Determining the precise impact and mechanisms of frontal instabilities on the eddies presented in this study are left for future work.

## 4.5 Conclusion

Frontal eddies have long been observed in satellite imagery near the MAB shelf-break front, but relatively few have been observed *in situ*. Their frequent occurrence indicates that frontal eddies may impact biological communities. In this study, we investigated two eddies, a cyclonic spiral eddy located seaward of the front and an anticyclonic eddy shoreward of the front. Despite having differing rotational directions, both eddies showed evidence of upwelling and nutrient enhancement. The cyclonic eddy contained locally-driven upwelling that occurred for the duration of the feature. The anticyclonic eddy was formed by cold pool water upwelling along the front, detaching from its parent water mass. Surface nutrient enhancement occurred only during eddy formation and was not replenished during the life of the eddy. Chlorophyll, diatom, and copepod enhancements occurred within both eddies, indicating possible biological

responses to upwelled nutrients. Satellite imagery suggests that frontal eddies similar to those observed herein are abundant within the MAB shelf-break frontal region. Both our observations and model results indicate that both eddy types may persist for more than a month, indicating that both eddy types may have significant impacts on biological communities near the front.

## 4.6 Tables

Table 4.1: Key differences between Eddy A and Eddy B, along with citations of any similar features.

| | Core Water Mass: | Rotation: | Position Relative to the Front: | Upwelled Water Mass: | Similar Eddies Observed Previously: |
|---|---|---|---|---|---|
| Eddy A | Slope | Cyclonic | Seaward | Slope | Garvine *et al.,* 1988 |
| Eddy B | Shelf | Anticyclonic | Shoreward | Cold Pool | Flagg *et al.,* 1997 |

## 4.7 Figures

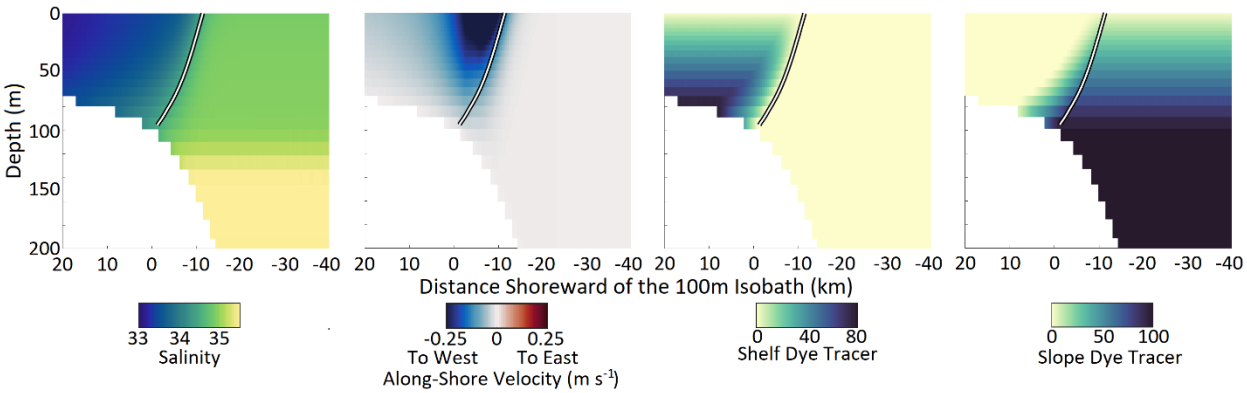


Figure 4.1: Initial modelled salinity, along-shore velocity, and dye concentrations along a transect in the cross-shelf direction. All variables are initially uniform in the along-shelf direction. The white and black contour denotes the 34.5 isohaline.

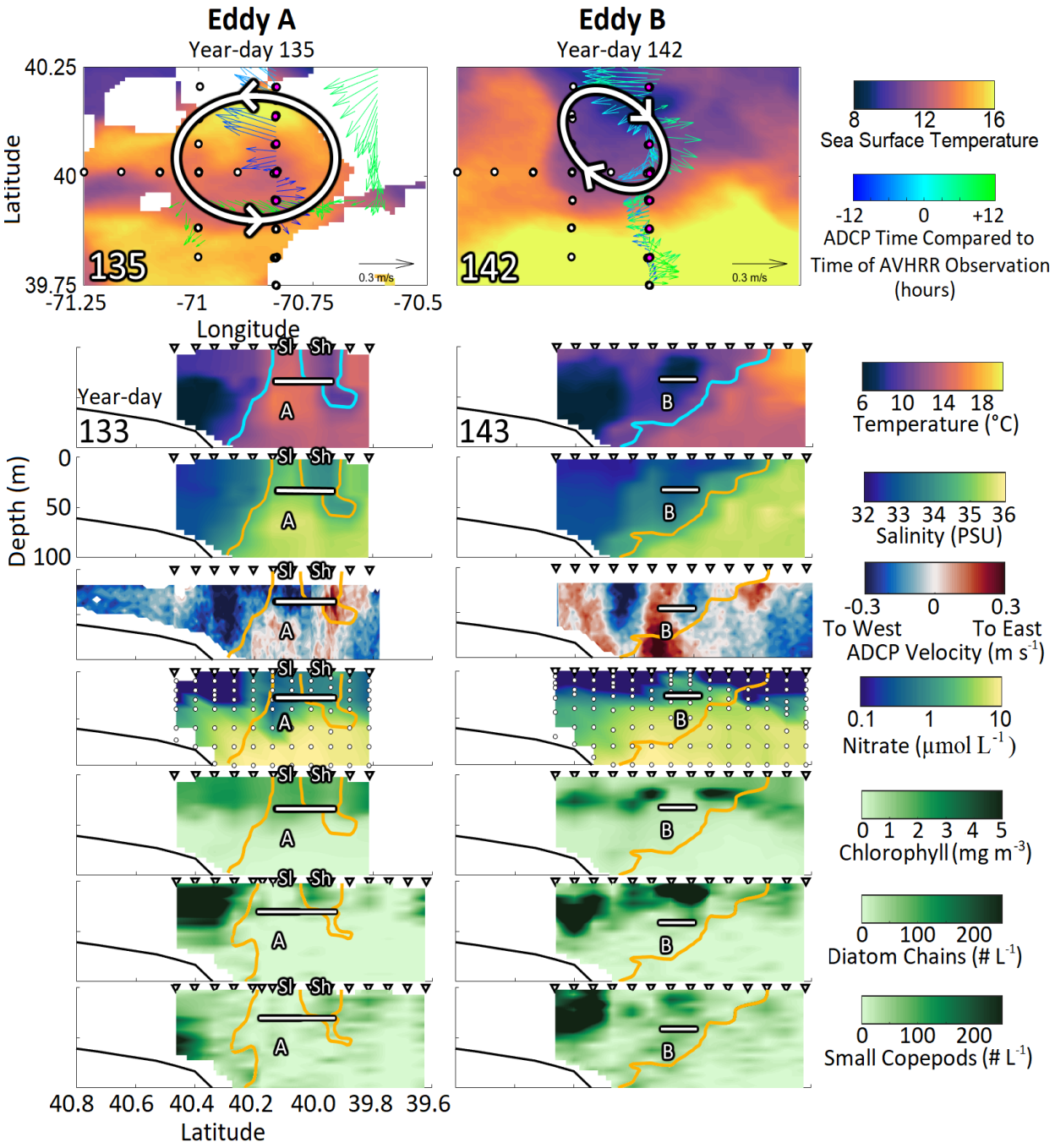


Figure 4.2: Sea surface temperature and transect observations of Eddy A and Eddy B. The first row shows AVHRR sea surface temperature, with stations locations (white and magenta dots) overlaid. Magenta dots represent CTD stations sampled within 12 hours (before or after) of the SST image. Detided ADCP data, averaged from 17-49m, collected within 12 hours (before and after) of the SST image are overlaid. The lower 3 rows are CTD north-south transects for temperature, salinity, and east-west ADCP velocity. Transect station locations are marked by triangles. Teal and orange lines denote the 34.5 isohaline. In all plots, the approximate locations of eddies A or B are shown by white lines. “Sl” and “Sh” denote the locations of the slope and shelf water filaments respectively for Eddy A (left column).

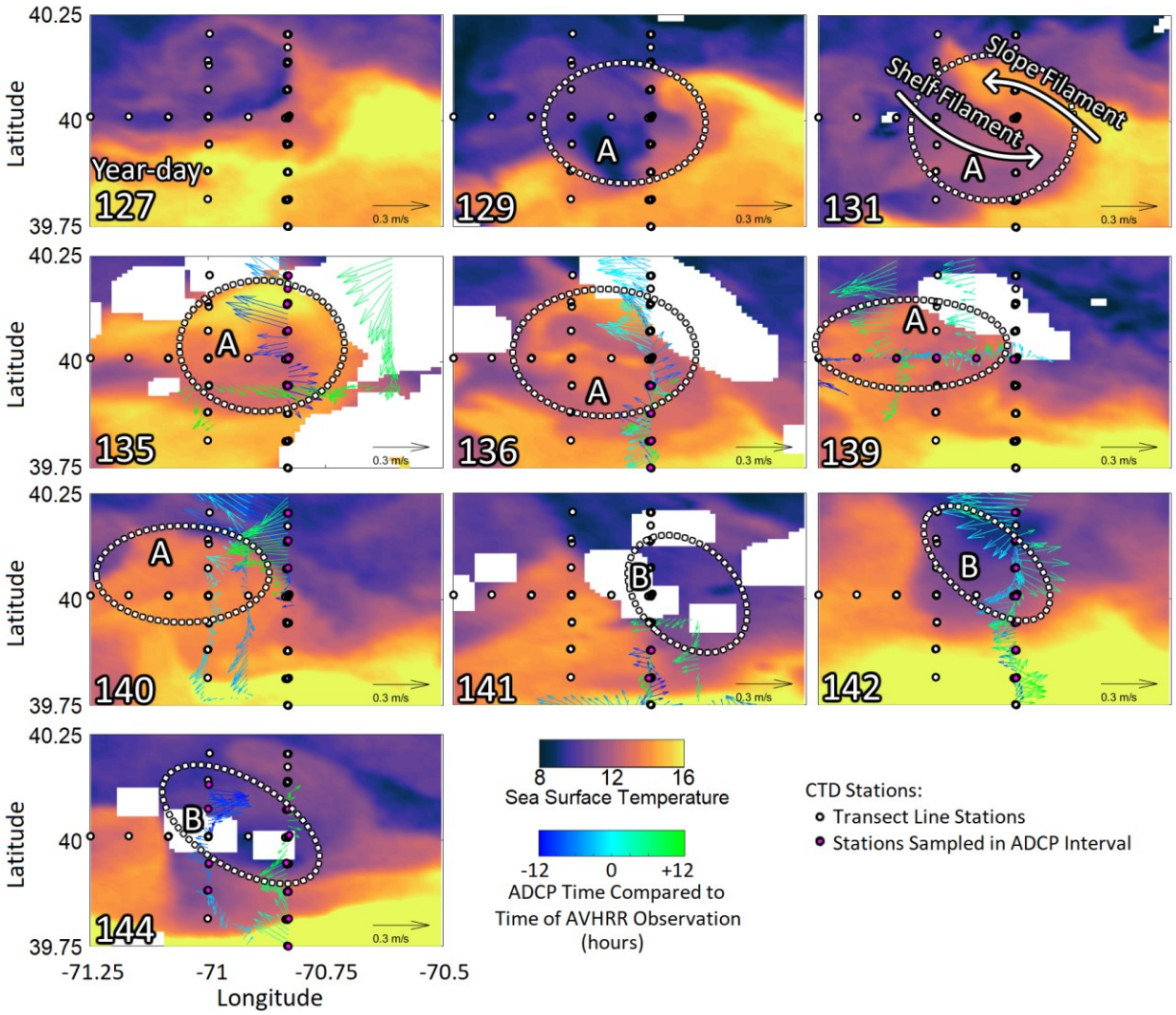


Figure 4.3: AVHRR sea surface temperature, with stations (white and magenta dots) overlaid. Magenta dots represent CTD stations sampled within 12 hours (before or after) of the SST image. Overlaid are detided ADCP velocities, averaged over the depth range of 17-49m, collected within 12 hours (before and after) of the SST image. Circles denote approximate borders of eddies A and B. Arrows in the upper right panel show the shelf and slope water filaments.

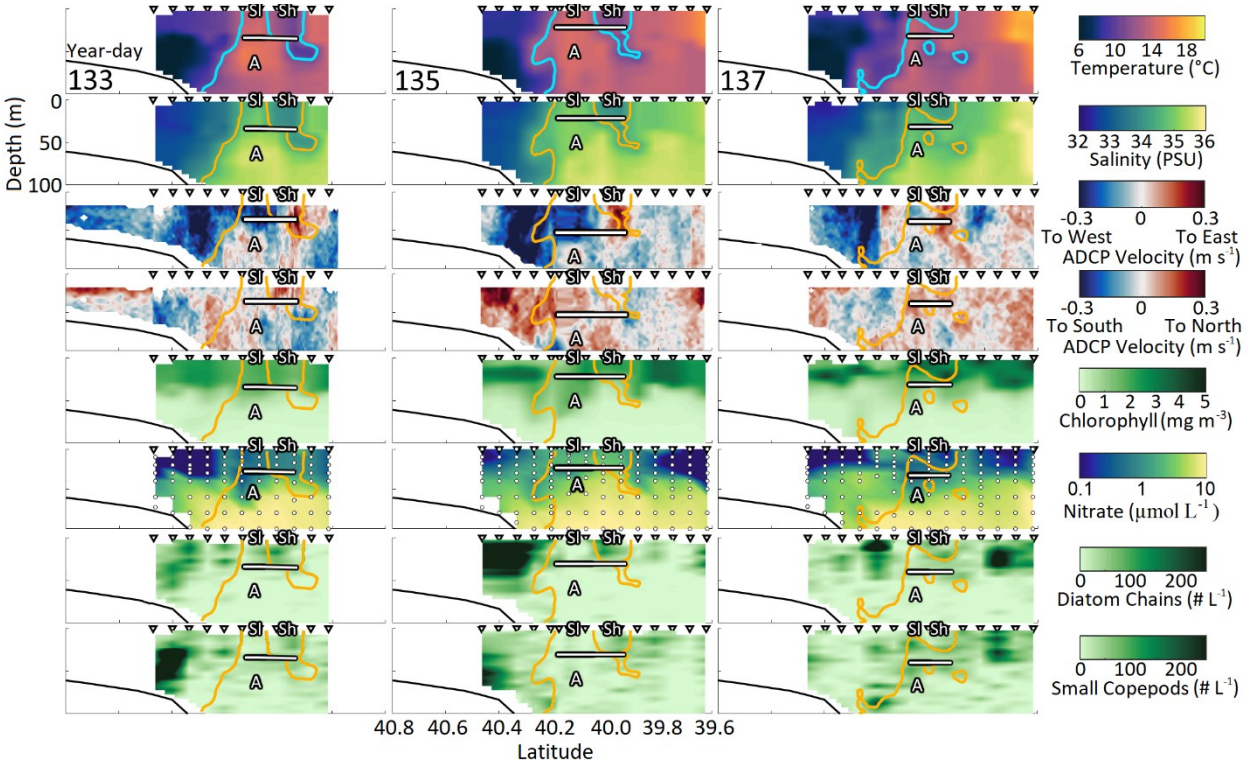


Figure 4.4: All north-south transects for Eddy A. Location of the eddy is denoted by white lines. "Sl" and "Sh" denote the locations of the slope and shelf water filaments respectively. Teal (first row) and orange (all other rows) contours indicate the location of the 34.5 isohaline. Black triangles show the locations of sampled stations. ADCP data was sampled continuously while underway. White circles represent bottle sample depths and locations.

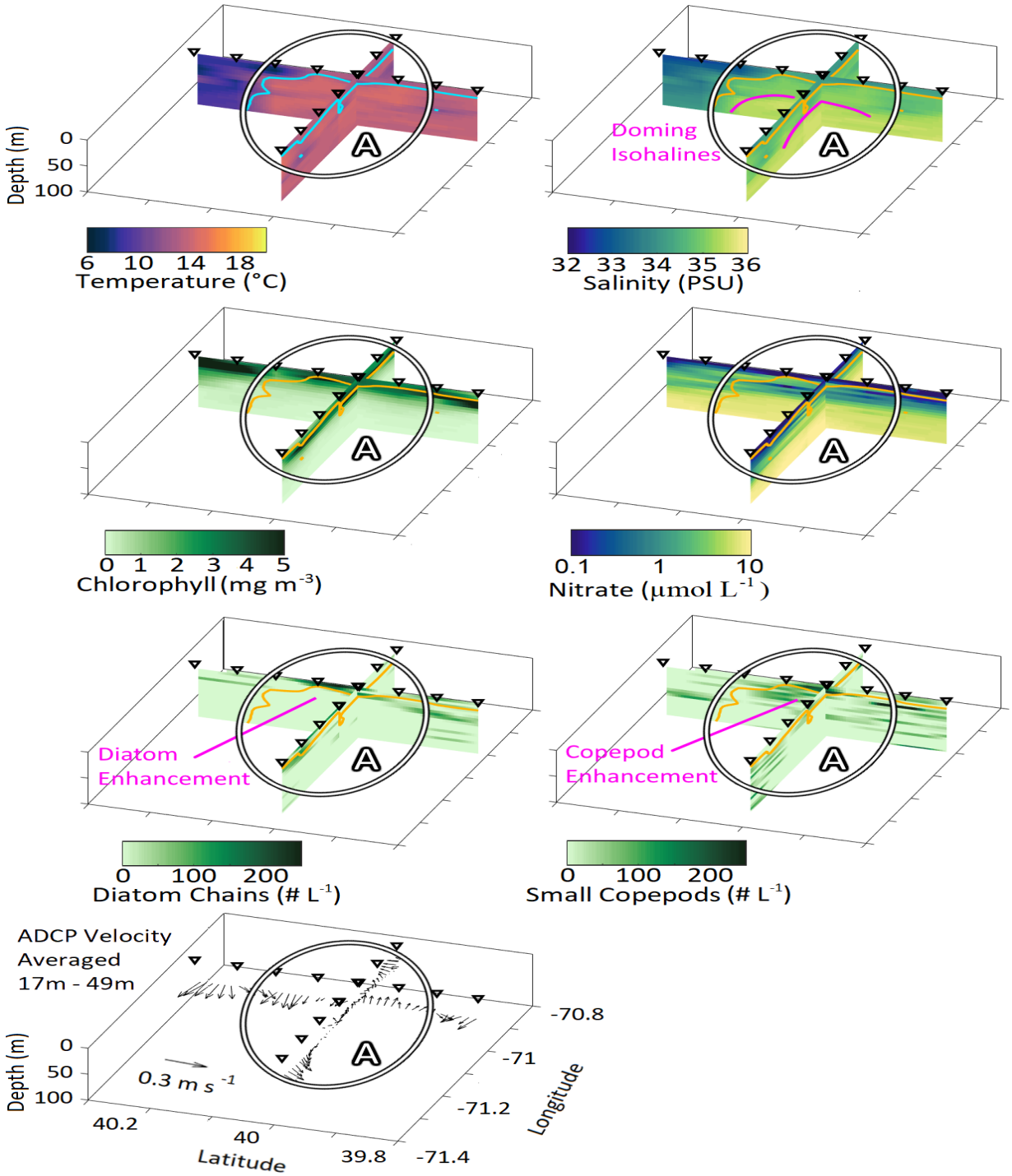


Figure 4.5: Eddy A adaptive sampling looking down from SW transects of Eddy A on year-day 138. White circles delineate the approximate borders of Eddy A. Teal (first plot) and orange (all others) contours indicate the location of the 34.5 isohaline. Black triangles show the locations of sampled stations. ADCP measurements are averaged over the depth range of 17-49m and plotted at a depth of 40m. Magenta labels highlight some of the eddy characteristics mentioned within the text.

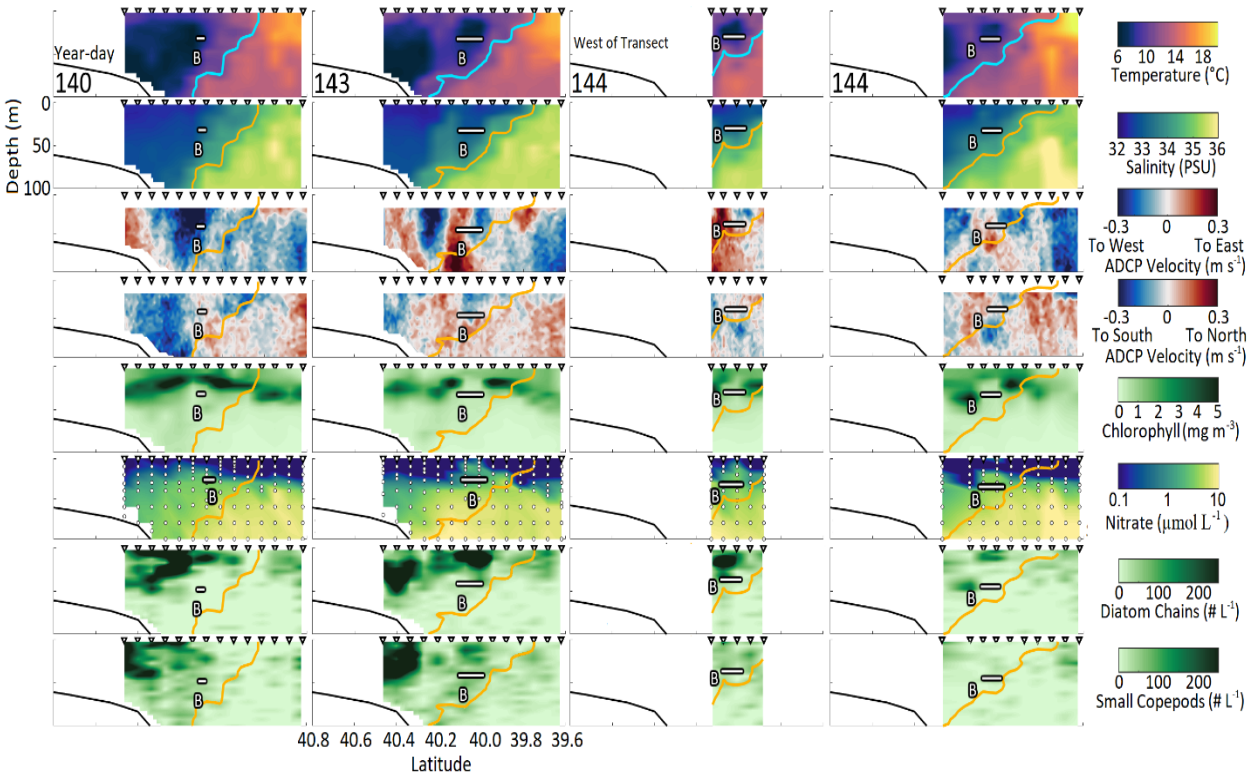


Figure 4.6: All north-south transects for Eddy B. The first, second, and fourth columns were taken along the same longitude, while the third column was located to the west. Location of the eddy is denoted by white lines. Teal (first row) and orange (all other rows) contours indicate the location of the 34.5 isohaline. Black triangles show the locations of sampled stations. ADCP data was sampled continuously while underway. White circles represent bottle sample depths and locations.

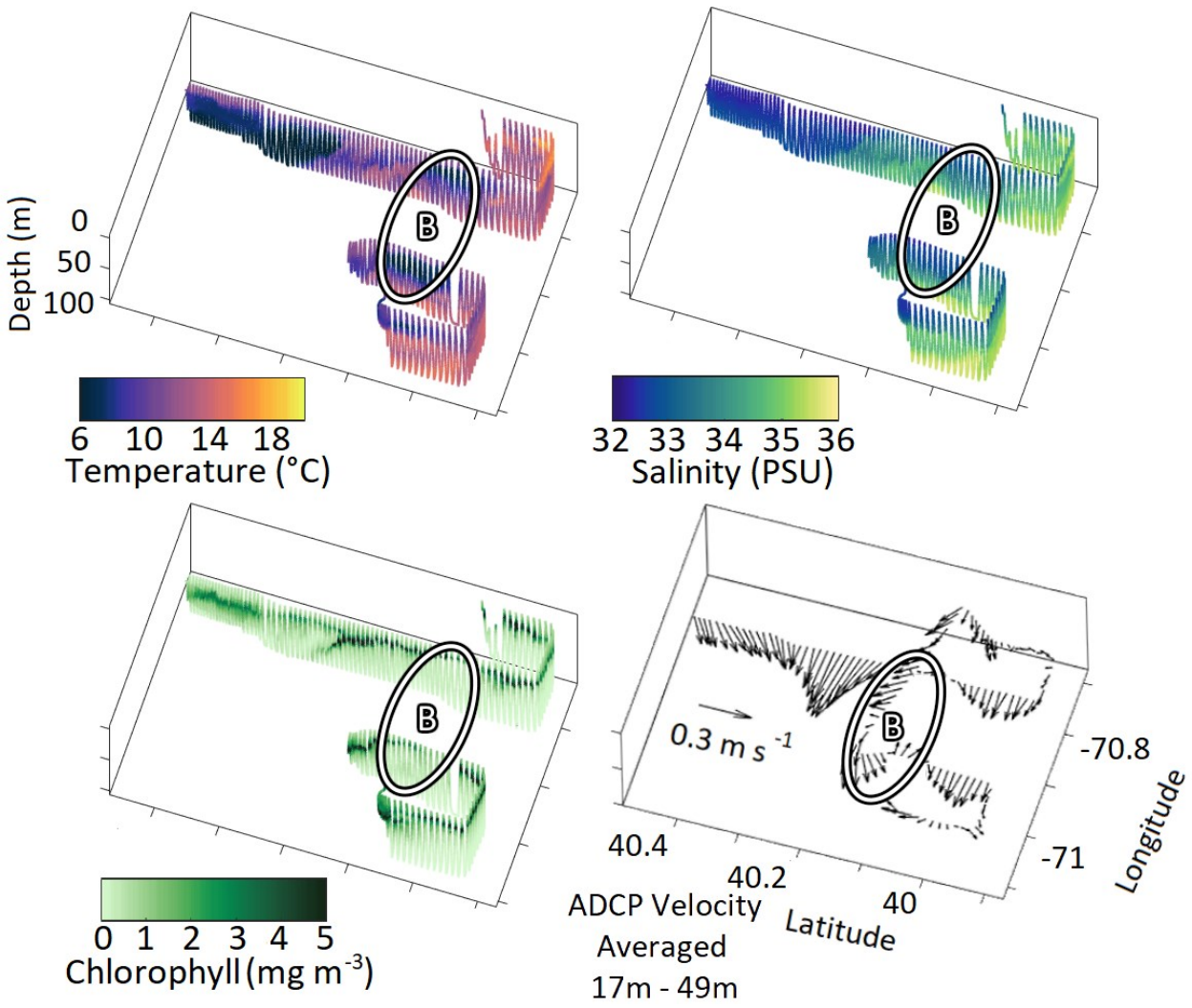


Figure 4.7: Two VPRII tows on year-day 143. White lines show the extent of Eddy B. ADCP measurements are averaged over the depth range of 17-49m and plotted at a depth of 40m.

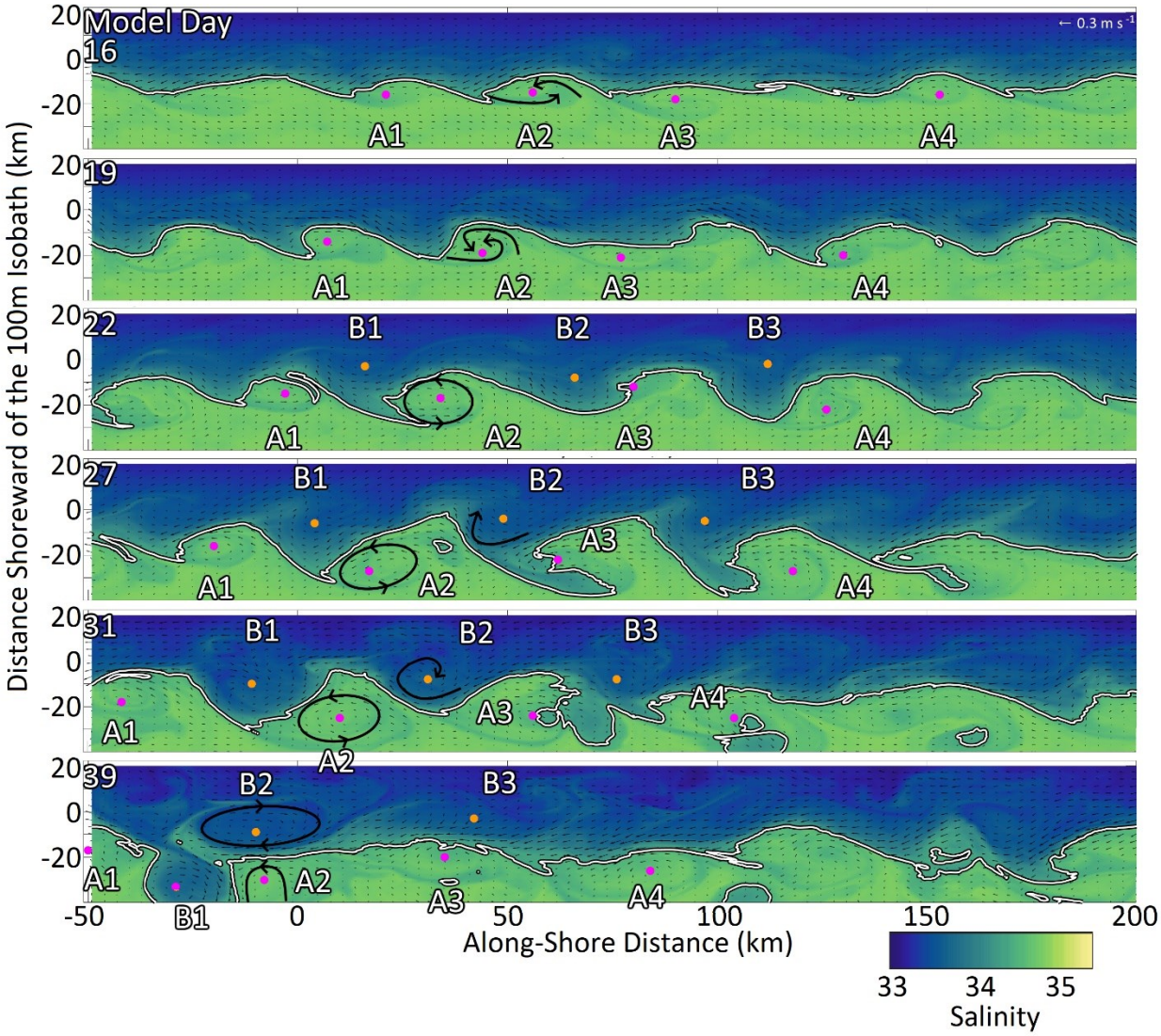


Figure 4.8: Modelled salinity (color) and horizontal velocity (vectors with scale in upper right of top plot) at 30m depth. Four Eddy A-like features (A1-A4, centers marked in magenta) and three Eddy B-like features (B1-B3, centers marked in orange) were tracked over time in this study. Centers are marked based on full water column analysis, not just the presented depth slice. The features described in detail herein are Eddies A2 and B2. Overlaid in black is the flow pattern described within the text and depicted in greater detail in Figures 4.10 and 4.11. The shelf-break front is represented by the 34.5 isohaline (white contours).

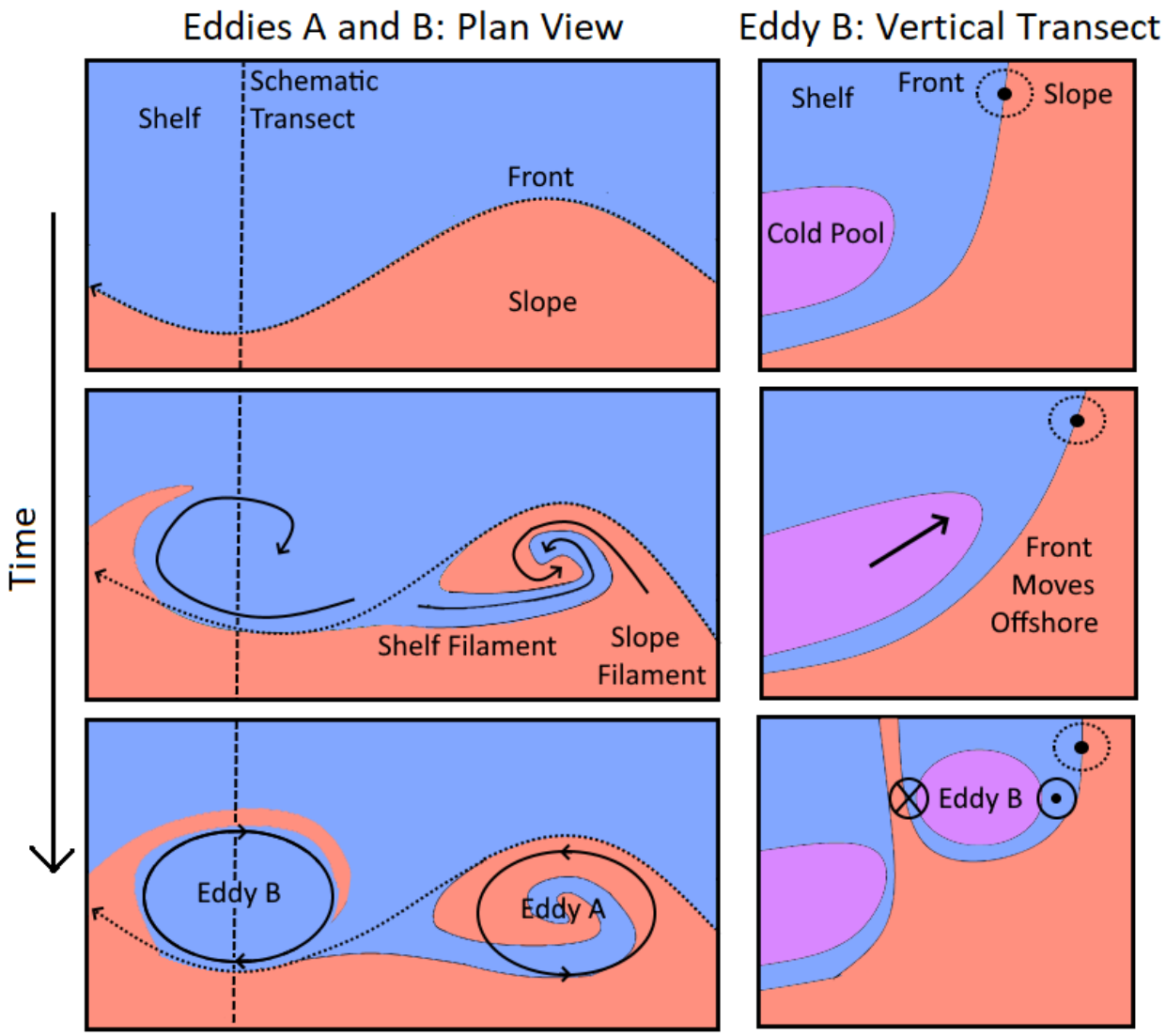


Figure 4.9: A simplified schematic showing the formation mechanisms of Eddy A and B. Though presented side-by-side for the sake of comparison, Eddy B formation occurs later than Eddy A formation within our simulation. The left panel shows a top view of the formation process. The right column shows the upwelling process at the interior of Eddy B. The dotted line in the left column is represents the transect shown on the right.

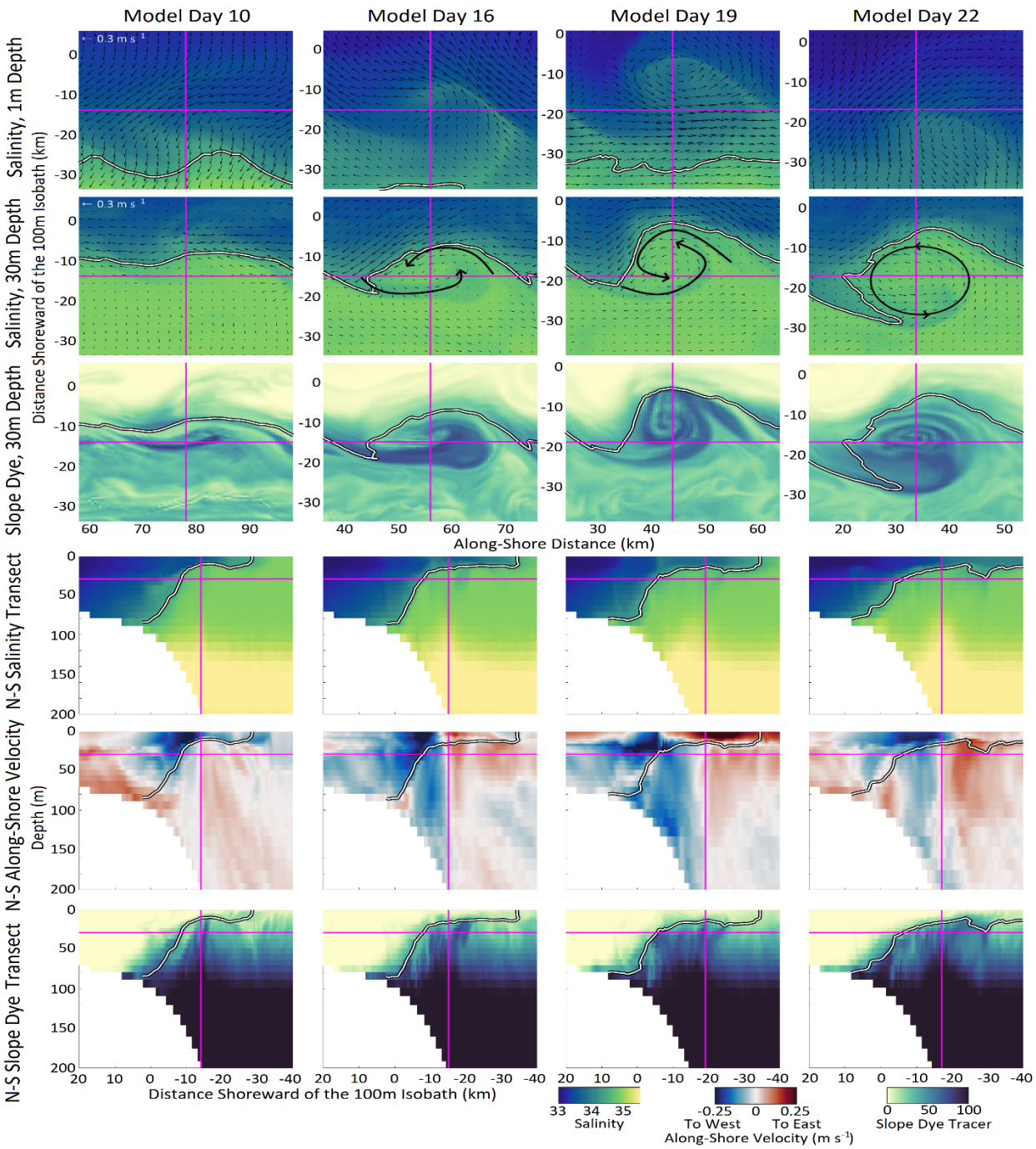


Figure 4.10: Magnified model results centered on Eddy A2. The first three rows are horizontal z-slices of fixed depth (first row: 1m, second and third rows: 30m), with a 40km x 40km subdomain centered on the eddy center. Horizontal velocity is overlaid on salinity in the first two rows (velocity scale in leftmost plots). The latter three rows are cross-shelf transects along the vertical magenta line shown in the first three rows, with expanded inshore and offshore coverage. The vertical magenta lines in the latter three rows marks the location of the horizontal magenta line in the first three rows. The horizontal magenta lines in the latter plots represent 30m depth. Overlaid on the second row in black is the Eddy A formation process described within the text. White contours are the 34.5 isohaline, representing the shelf-break front.

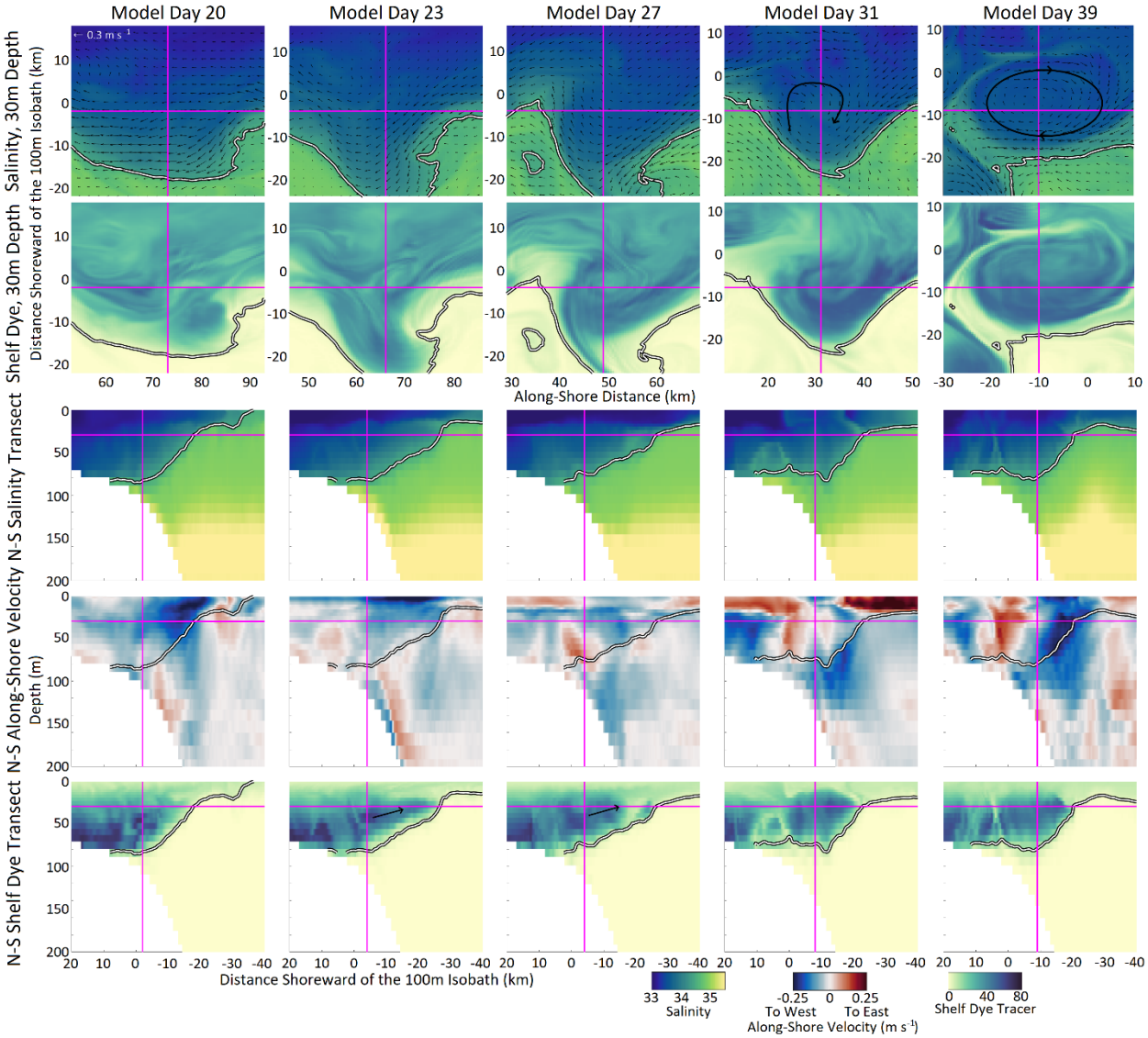


Figure 4.11: Magnified model results centered on Eddy B2. The first three rows are horizontal z-slices at 30m depth, with a 40km x 40km subdomain centered on the eddy center. Horizontal velocity is overlaid on salinity in the first rows (velocity scale in leftmost plots). The latter three rows are cross-shelf transects along the vertical magenta line shown in the first two rows, with expanded inshore and offshore coverage. The vertical magenta lines in the latter three rows marks the location of the horizontal magenta line in the first three rows. The horizontal magenta lines in the latter plots represent 30m depth. Overlaid on the second row in black is the Eddy B formation process described within the text. White contours are the 34.5 isohaline, representing the shelf-break front.

## 4.8 Supplemental Figures

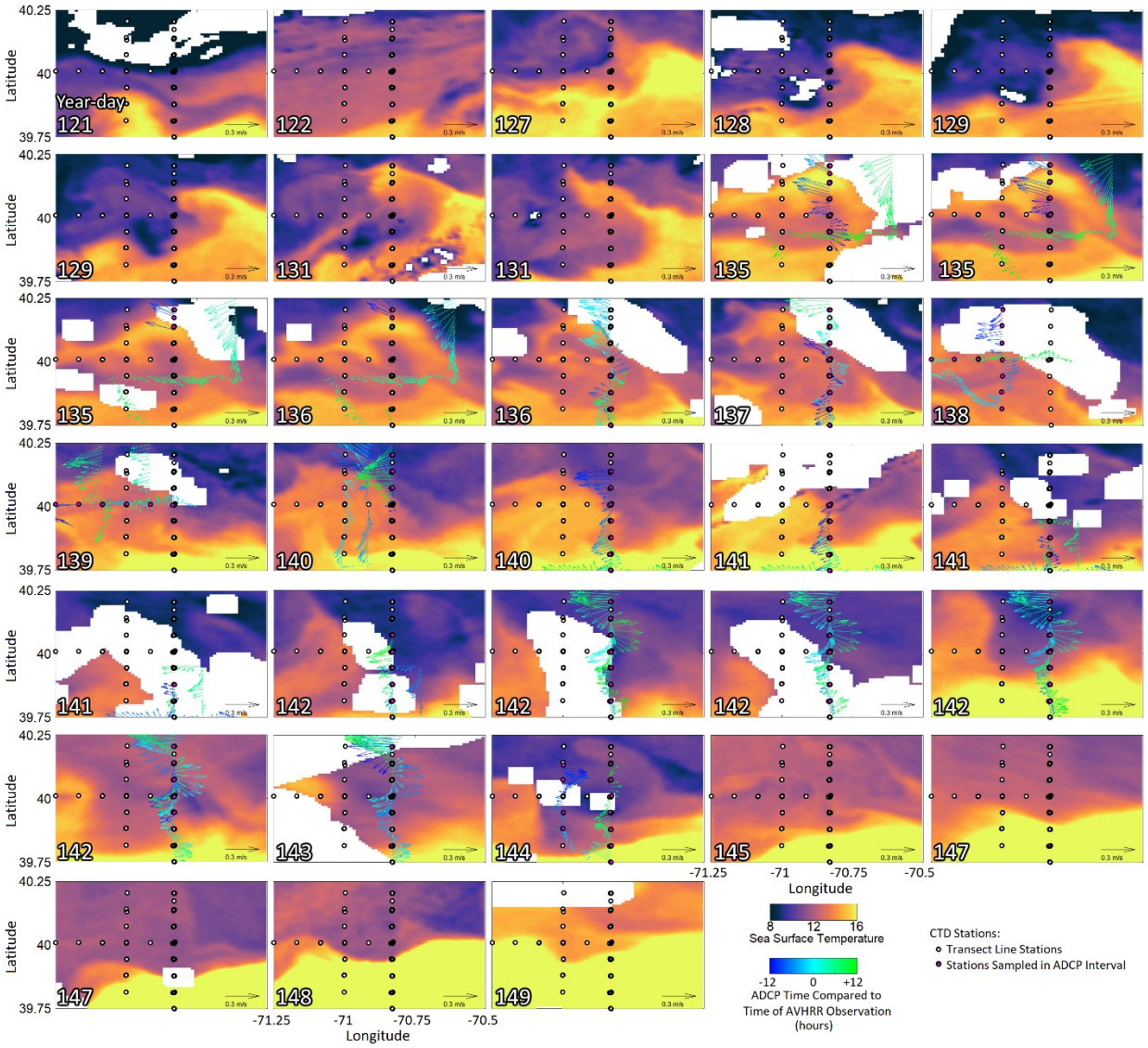


Supplemental Figure 4.1: AVHRR sea surface temperature at selected times during the cruise period. Duplicated year-days represent multiple measurements during the same day. Overlaid are all sampled station locations (white and magenta dots), with magenta dots representing CTD stations sampled within 12 hours (before or after) of the SST image. Overlaid are detided ADCP velocities, averaged over the depth range of 17-49m, collected within 12 hours (before and after) of the SST image. Circles denote approximate borders of eddies A and B.

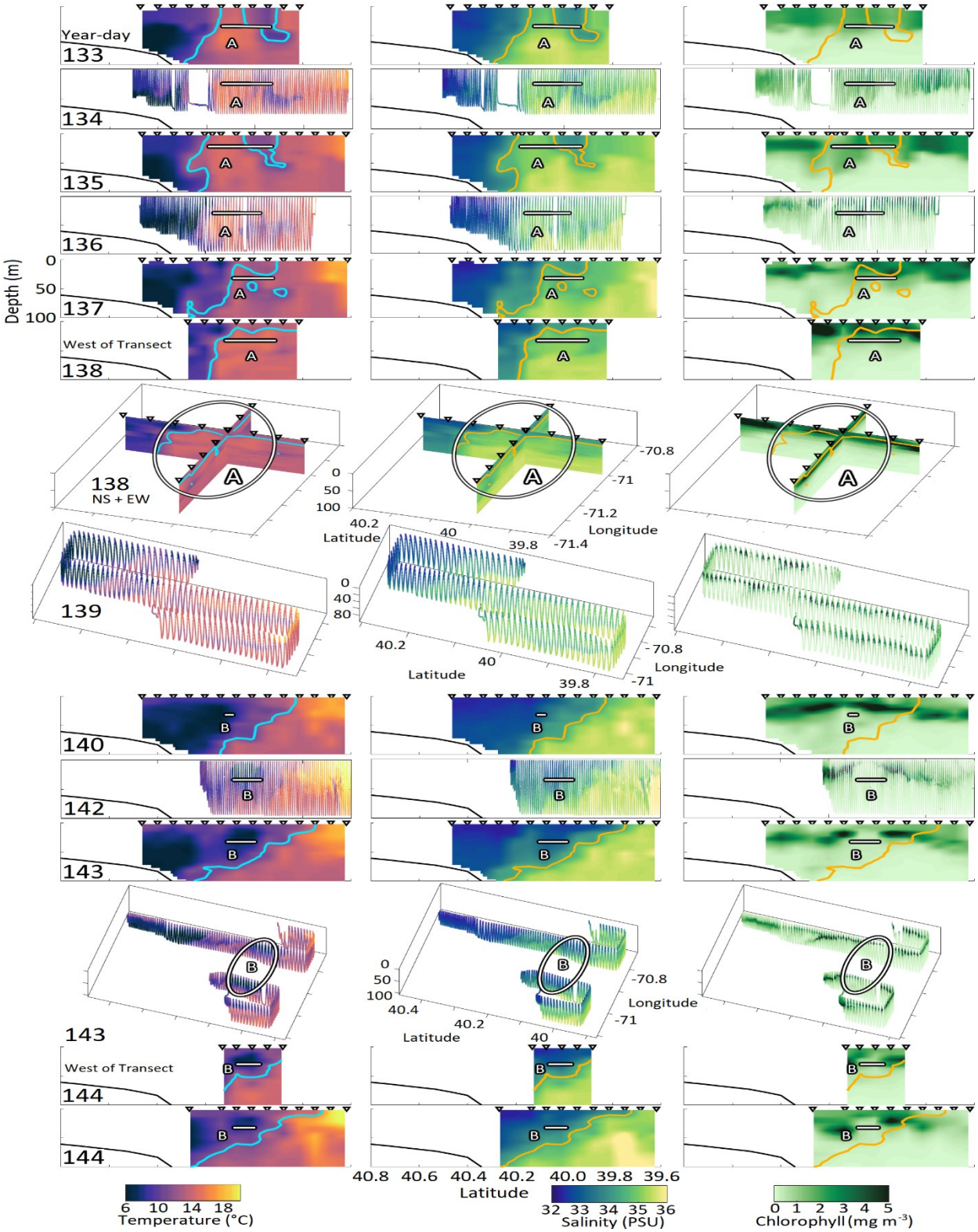


Supplemental Figure 4.2: A complete atlas of transects in May 2019, for temperature, salinity, and chlorophyll. Location of the eddy is denoted by the white lines. Teal (first row) and orange (all other rows) contours indicate the location of the 34.5 isohaline. Black triangles show the locations of sampled stations.

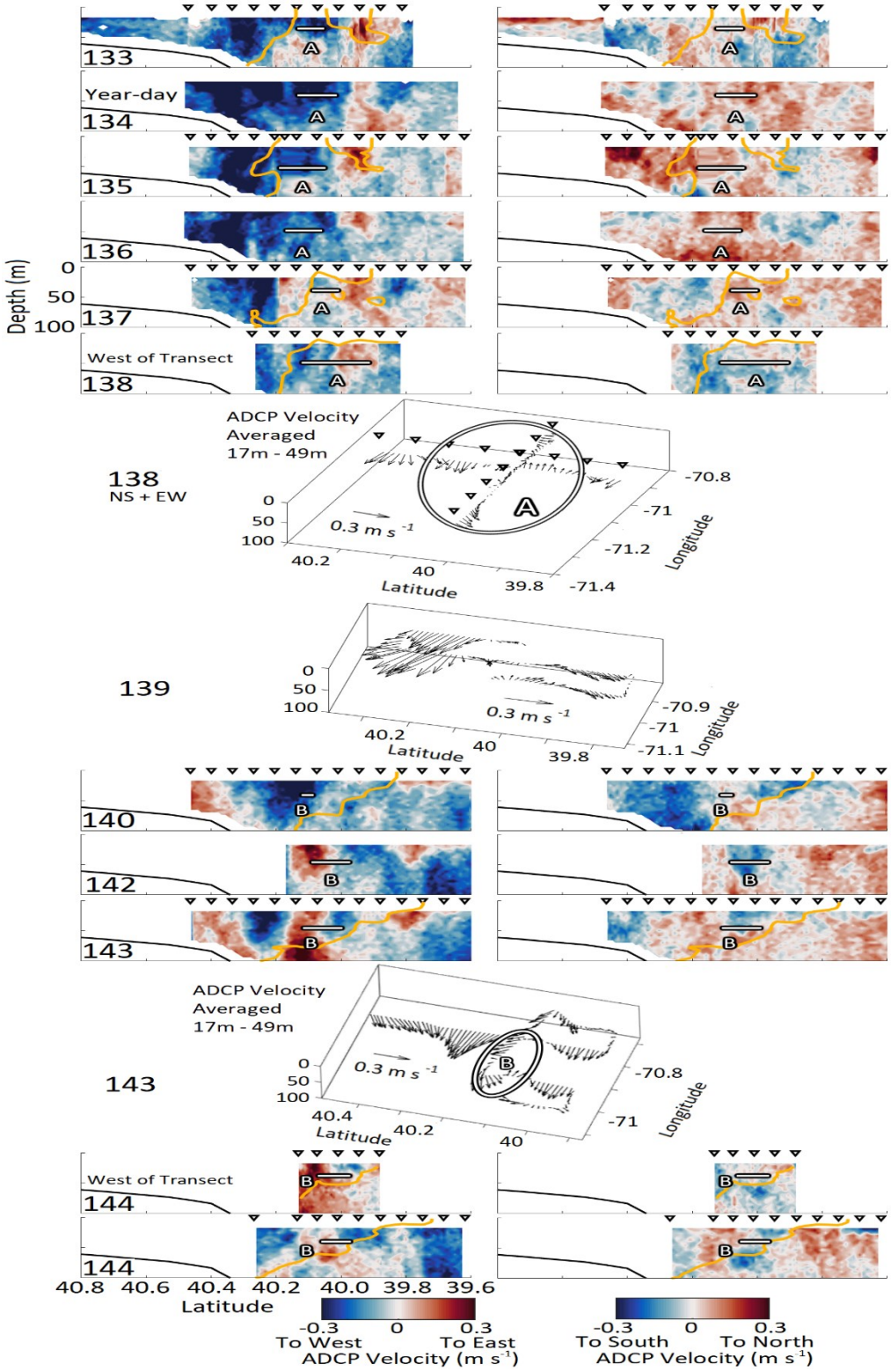


Supplemental Figure 4.3: A complete atlas of transects in May 2019, for ADCP velocities. Location of the eddy is denoted by the white lines. Orange contours indicate the location of the 34.5 isohaline. Black triangles show the locations of sampled stations. 3D ADCP measurements are averaged over the depth range of 17-49m and plotted at a depth of 40m.

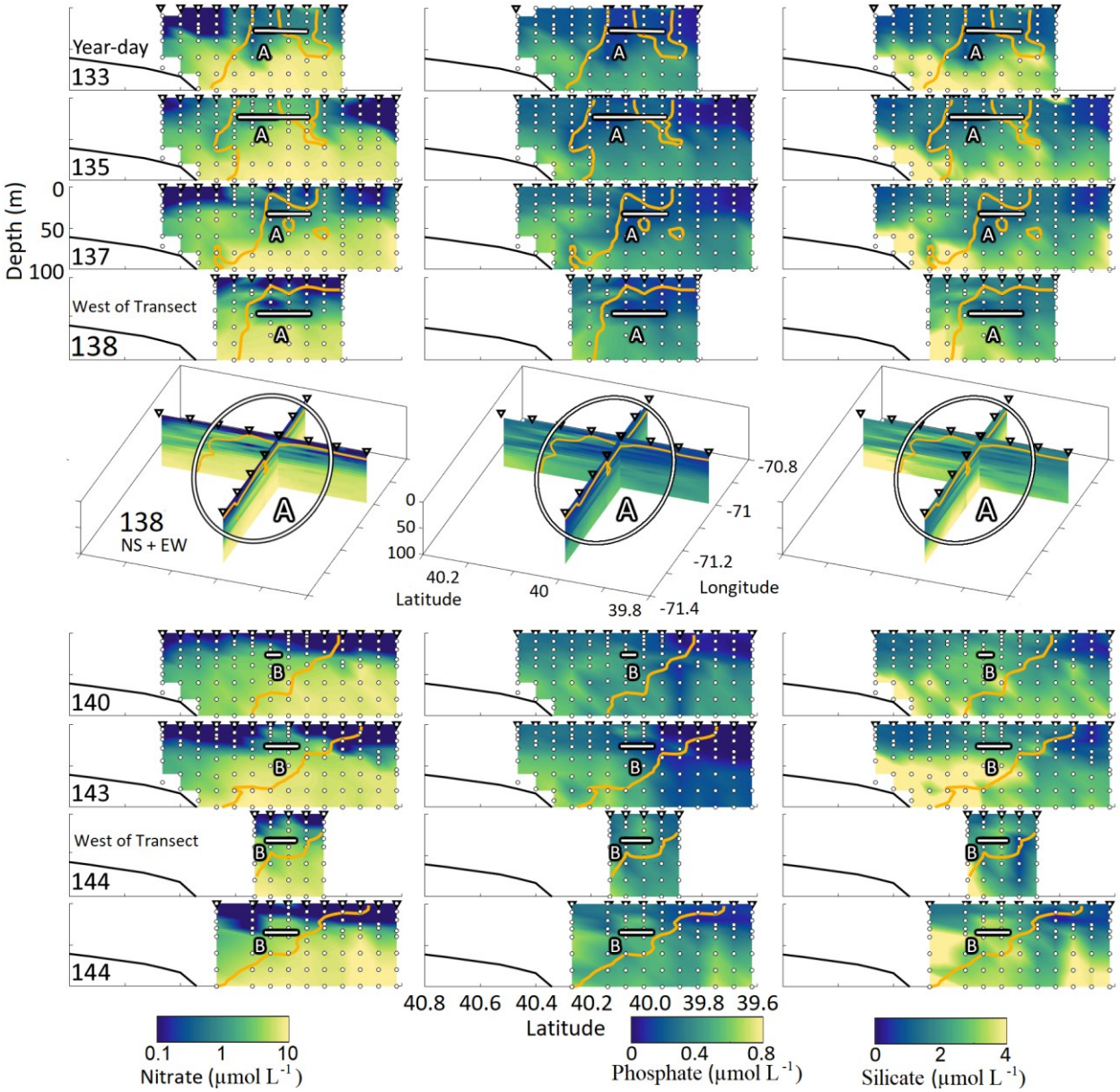


Supplemental Figure 4.4: A complete atlas of transects in May 2019, for bottle nutrients. Location of the eddy is denoted by the white lines. Orange contours indicate the location of the 34.5 isohaline. Black triangles show the locations of sampled stations. White circles represent bottle sample depths and locations.

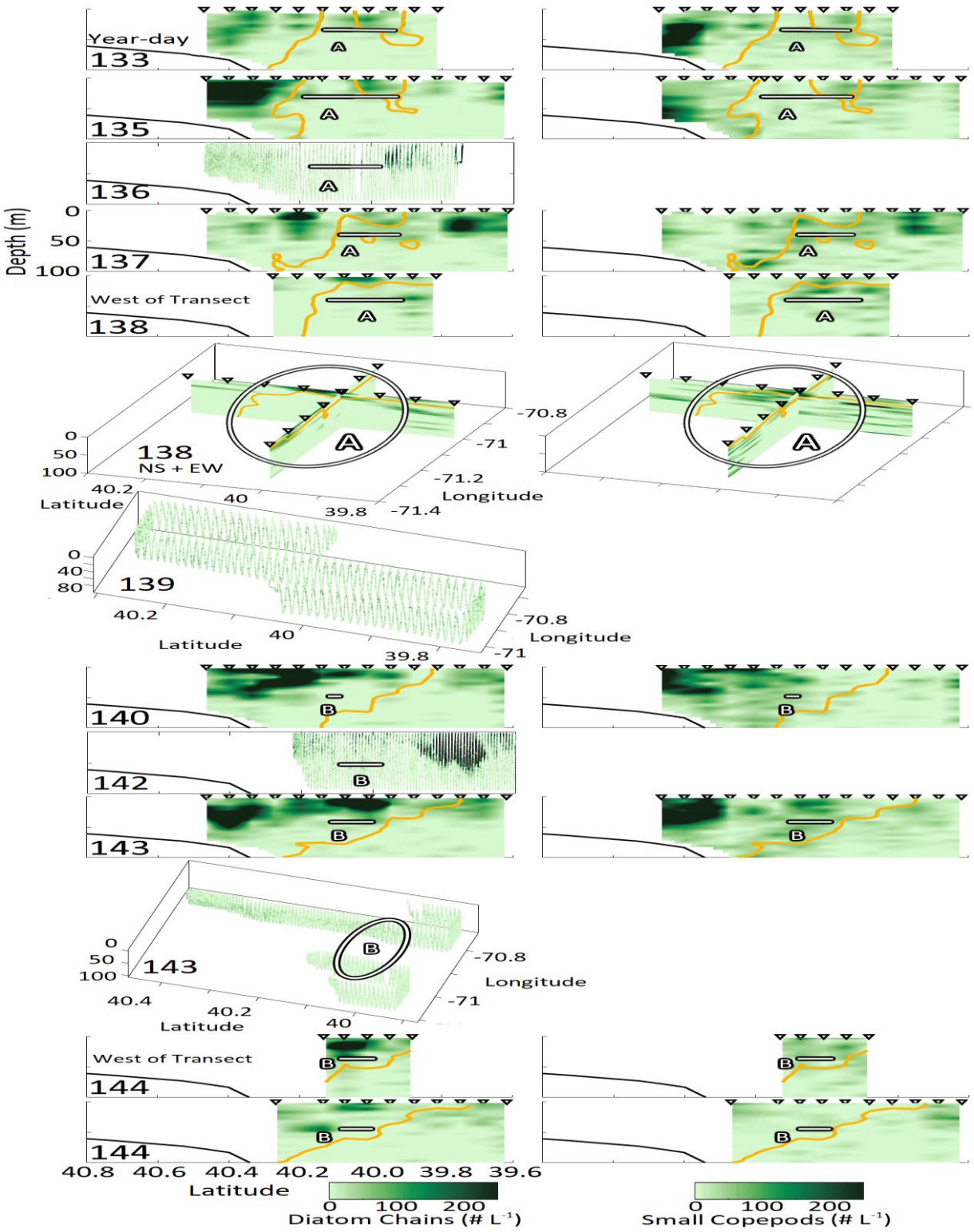


Supplemental Figure 4.5: A complete atlas of transects in May 2019, for VPR diatoms and copepods. Location of the eddy is denoted by the white lines. Orange contours indicate the location of the 34.5 isohaline. Black triangles show the locations of sampled stations. Year-day 139 and year-day 143 (3-D plot) contain VPRII ROIs. All other plots use manually annotated DAVPR ROIs.

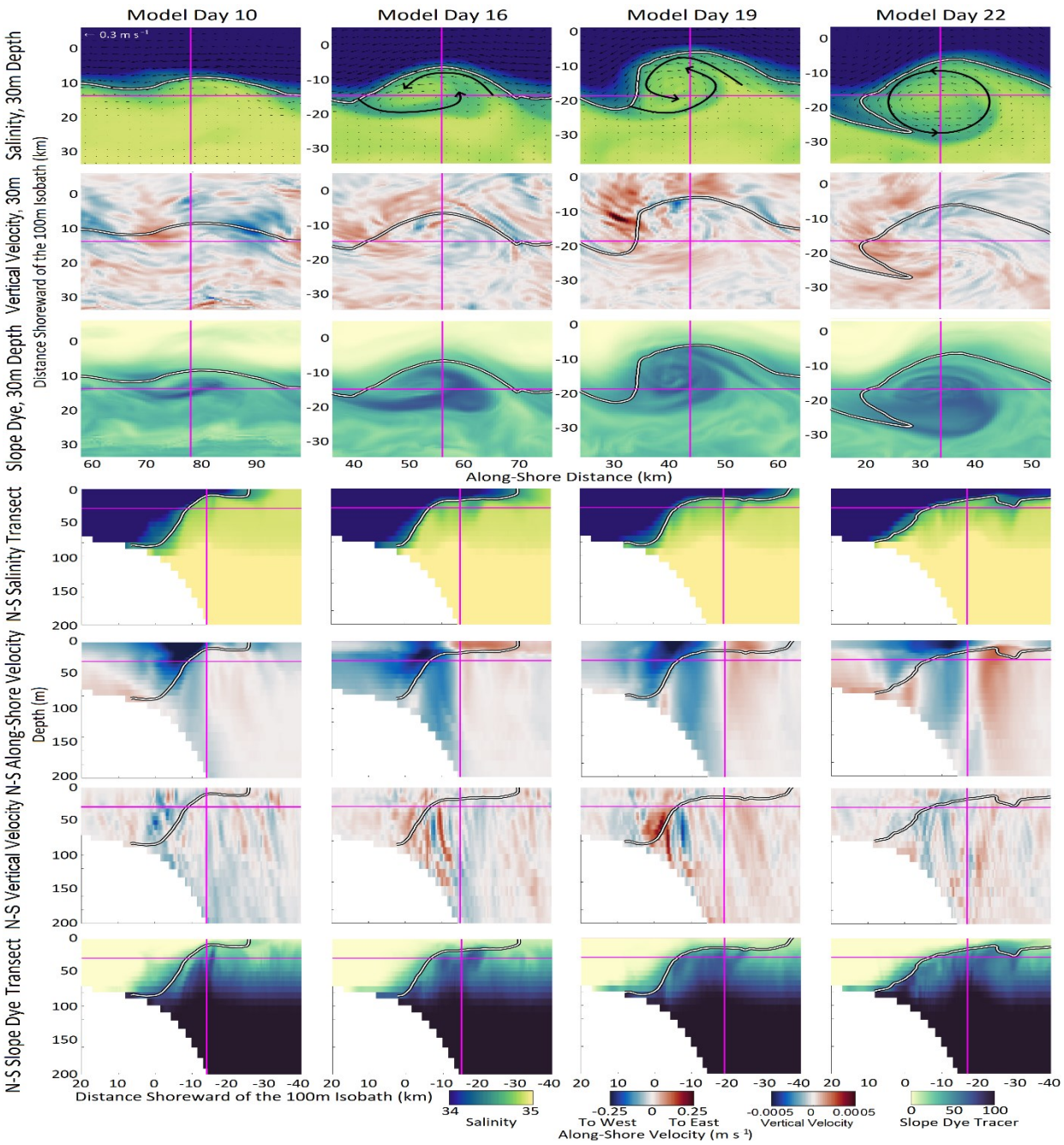


Supplemental Figure 4.6: Magnified model results centered on Eddy A2 that have been averaged over one model day, to enhance trends in vertical velocity. The first three rows are horizontal z-slices at a depth of 30 m, with a 40km x 40km subdomain centered on the eddy center. Horizontal velocity is overlaid on salinity in the first row (velocity scale in leftmost plot). The latter four rows are cross-shelf transects along the vertical magenta line shown in the first three rows, with expanded inshore and offshore coverage. The vertical magenta lines in the latter three rows marks the location of the horizontal magenta line in the first three rows. The horizontal magenta lines in the latter plots represent 30m depth. Overlaid on the first row in black is the Eddy A formation process described within the text. White contours are the 34.5 isohaline, representing the shelf-break front.

# Chapter 5

## Conclusions

In this thesis, I have focused on answering a specific question: how does the shelf-break front affect biological populations? Each of my chapters has approached this question from a different perspective. My second chapter explored a novel method of processing towed Video Plankton Recorder (VPR) images to facilitate processing of the large volumes of data collected by that instrument, enabling high-resolution depiction of planktonic organisms together with their physical environment. While not used within Chapter 3, the classifier was used in Chapter 4 and a related study (Oliver *et al.*, 2021). My third chapter approached this question directly using transect crossings from three separate cruises in April 2018, May 2019, and July 2019. Changes in physical and biological quantities were assessed through repeated occupations of the same transect line, at fixed stations. These crossings were then averaged within an Eulerian coordinate system and within a frontally-aligned coordinate system. My fourth chapter explored the impacts of two frontal eddies observed in May 2019. Observations include transect data described in Chapter 3, as well as adaptive sampling of the eddies that required measurements away from the main transect. Nutrients were enhanced within the eddies, motivating use of an idealized model to determine whether upwelling was occurring within the two eddies. Each of these techniques provided an additional perspective to exploring the biological impact of the shelf-break front.

Upwelling was of particular interest due to its potential for enhancing plankton populations at the front. Chapter 4 documented nutrient enhancement within two frontal eddies A and B, despite rotating in opposite directions from each other. Modelled eddies showed that the nutrient enhancement was occurring as the result of upwelling. In modelled Eddy A, upwelling was persistent and occurred for the life of the eddy, while in modelled Eddy B upwelling

occurred during eddy formation. The Eulerian mean of nutrient concentrations for May 2019 displayed nutrient enhancement at the front (Chapter 3), driven by Eddies A and B (Chapter 4). July 2019 had depleted nutrients throughout the surface and no mean nutrient enhancement at the front.

In both April 2018 and May 2019, locations of nutrient enhancement were sites of biological change. Chlorophyll enhancement at the front in April 2018 was transient. On year-day 108, the transient chlorophyll enhancement was the result of Ekman restratification relieving phytoplankton from light limitation, which allowed them to take advantage of abundant nutrients (Oliver *et al.*, 2022). Other ephemeral chlorophyll enhancements occurred on both sides of the front throughout the April 2018 cruise. Chlorophyll enhancement was not seen in Eulerian means, but was seen in frontally-aligned means. Neither VPR-measured diatom chains nor copepods were associated with the transient chlorophyll blooms in April 2018. Instead, nanoplankton were observed within at least one of the enhancements (Oliver *et al.*, 2022). Small copepods were enhanced in mean observations under a frontal coordinate system, but not concurrently to individual chlorophyll enhancements. In May 2019 mean observations, chlorophyll was enhanced at the front. This was due to enhancement associated primarily with Eddy B. Eddy B contained chlorophyll enhancement around the periphery, while diatoms and small copepods were enhanced within eddy center. Nutrient enhancement was also highest within eddy center. The origins of both diatoms and small copepods within eddy center are likely due to either biological response or due to advection from populations further inshore during eddy formation. The biological response to Eddy B was likely still ongoing when last sampled. Eddy A initially had chlorophyll, diatoms, and small copepods at approximately background levels. As the eddy evolved, all three became enhanced within eddy center. In July 2019,

chlorophyll, diatoms, and small copepods were not enhanced at the front, though enhancement of chlorophyll and diatoms was observed in hotspots to the south of the front in the Slope Sea (Oliver *et al.*, 2021). This offshore enhancement in individual transect crossings was associated with Gulf Stream intrusions.

In conclusion, we saw both nutrient enhancement and biological enhancement at the shelf-break front. However, the observed enhancement was highly transient, especially from a fixed Eulerian perspective. The frontal eddies in May 2019 rapidly traversed our study region and the enhancements due to Ekman restratification in April 2018 were highly ephemeral. Our results suggest that the front and related frontal eddies primarily affect biological communities in a localized manner. These localized effects could have an impact on primary production when extrapolated across the entire MAB shelf-break front, and could potentially explain why higher trophic levels (*e.g.* fishery important species) are sometimes seen aggregating at the front (*e.g.*, Podestá *et al.*, 1993). However, most features observed herein were localized not only in space, but also in time. As a result, exploitation of enhanced plankton abundance would require predators with sufficiently high mobility to locate and travel between patches (*e.g.,* pelagic fishes, cetaceans). The enhancements we saw at the front were not significantly greater than enhancements away from the front, particularly in comparison with the persistent inshore enhancements of diatoms and small copepods observed in May and July 2019.

The data presented herein represents the highest resolution systematic surveys of the shelf-break front conducted to date. Adaptive sampling facilitated occupation of all transient features more than once, providing insight into their temporal evolution. Based on all these data, we found that mean chlorophyll, diatoms, and small copepods are not significantly enhanced at the MAB shelf-break front. Although we still cannot rule out undersampling, the more rare that

frontal enhancement processes are, the more extraordinary the enhancement must be in order to shape the mean fields.

# Appendix

## References


Barth J, Bogucki D, Pierce S, Kosro PM (1998). Secondary circulation associated with a shelfbreak front. *Geophys. Res. Lett*., 25.

Basedow SL, Tande KS, Norrbin MF, Kristiansen SA (2013). Capturing quantitative zooplankton information in the sea: performance test of laser optical plankton counter and video plankton recorder in a *Calanus finmarchicus* dominated summer situation. *Prog. Oceanogr.,* 108: 72-80.

Benthuysen J, Thomas LN, Lentz SJ, (2015). Rapid Generation of Upwelling at a Shelf Break Caused by Buoyancy Shutdown. *J. Phys. Oceanogr.*, 45: 294–312.

Bochinski E, Bacha G, Eiselein V, Walles TJW, Nejstgaard JC, Sikora T (2019). Deep Active Learning for *in situ* plankton classification. *ICPR 2018 Workshops*, LNCS 11188.

Brownlee EF, Olson RJ, Sosik HM (2016). Microzooplankton community structure investigated with imaging flow cytometry and automated live-cell staining. *Mar. Ecol. Progr. Ser.,* 550: 65-81.

Campbell RW, Roberts PL, Jaffe J (2020). The Prince William Sound Plankton Camera: a profiling in situ observatory of plankton and particulates, *ICES Journal of Marine Science*, 77(4):1440–1455.

Chapman DC, Lentz SJ (1994). Trapping of a Coastal Density Front by the Bottom Boundary Layer. *J. Phys. Oceanogr*., 24: 1464–1479.

Cheng K, Cheng X, Wang Y, Bi H, Benfield MC (2019). Enhanced convolutional neural network for plankton identification and enumeration. *PLoS One*, 14.

Davis, CS, Gallager SM, Solow AR (1992). Microaggregations of oceanic plankton observed by towed video microscopy. *Science*, 257: 230-232.

Davis CS, Hu Q, Gallager S, Tang X, Ashjian CJ (2004). Real-time observation of taxa-specific plankton distributions: An optical sampling method. *Mar. Ecol. Progr. Ser*., 284, 77-96.

Davis, C.S. and D. J. McGillicuddy. 2006. Transatlantic abundance of the N2-fixing colonial cyanobacterium *Trichodesmium*. Science, 312: 1517-1520, doi:10.1126/science.1123570

Davis CS, Thwaites FT, Gallager SM, Hu W (2005). A three-axis fast-tow digital Video Plankton Recorder for rapid surveys of plankton taxa and hydrography. *Limnol. Oceanogr. Meth*. 3: 59-74.

Flagg CN, Wallace D, Kolber Z (1997). Cold anticyclonic eddies formed from cold pool water in the southern Middle Atlantic Bight. *Cont. Shelf Res.,* 17(15):1839-1867.

Garvine RW, Wong K-C, Gawarkiewicz GG, McCarthy RK (1988). The morphology of shelfbreak eddies. *J. Geophys. Res.*, 93(C12):15593-15607.

Gawarkiewicz G, Chapman DC (1992). The Role of Stratification in the Formation and Maintenance of Shelf-Break Fronts. *J. Phys. Oceanogr*., 22: 753–772.

Gawarkiewicz G, Bahr F, Beardsley RC, Brink KH (2001). Interaction of a Slope Eddy with the Shelfbreak Front in the Middle Atlantic Bight. *J. Phys. Oceanogr*., 31:2783–2796

Gawarkiewicz G, Brink KH, Bahr F, Beardsley RC, Caruso M, Lynch JF, and Chiu C-S (2004), A large-amplitude meander of the shelfbreak front during summer south of New England: Observations from the Shelfbreak PRIMER experiment, *J. Geophys. Res.*, 109.

Gawarkiewicz G, Todd RE, Zhang W, Partida J, Gangopadhyay A, Monim M-U-H, Fratantoni P, Malek Mercer A, Dent M (2018). The changing nature of shelf-break exchange revealed by the OOI Pioneer Array. *Oceanography,* 31(1): 60–70.

González P, Castaño A, Peacock EE, Díez J, Del Coz JJ, Sosik HM (2019). Automatic plankton quantification using deep features. *J. Plankton Res.* 41: 449-463.

Hales B, Vaillancourt R, Prieto L, Marra J, Houghton R, Hebert D (2009a). High-resolution surveys of the biogeochemistry of the New England shelfbreak front during Summer, 2002. *J. Mar. Syst.*, 78: 426-441.

Hales B, Hebert D, Marra J (2009b). Turbulent supply of nutrients to phytoplankton at the New England shelf break front. *J. Geophys. Res*., 114.

Houghton RW, Hebert D, Prater M (2006). Circulation and mixing at the New England shelfbreak front: Results of purposeful tracer experiments. *Prog. Oceanogr*., 70: 289-312.

Houghton RW, Olson DB, Celone PJ (1986). Observation of an anticyclonic eddy near the continental shelf break south of New England. *J. Phys. Oceanogr.,* 16:60-71.

Houghton RW, Visbeck M (1998). Upwelling and convergence in the Middle Atlantic Bight shelfbreak front. *Geophys. Res. Lett*., 25: 2765–2768.

Hu Q, Davis C (2005). Automatic plankton image recognition with co-occurrence matrices and Support Vector Machine. *Mar. Ecol. Progr. Ser*., 295: 21-31.

Kennelly MA, Evans RH, Joyce TM (1985). Small-scale cyclones on the periphery of a Gulf Stream warm-core ring. *J. Geophys. Res.,* 90(C5):8845-8857.

Krizhevsky A, Sutskever I, Hinton GE (2012). ImageNet classification with deep convolutional neural networks. Adv. Neural Inf. Process. Syst., 1097–1105.

Lee H, Park M, Kim J (2016). Plankton classification on imbalanced large scale database via convolutional neural networks with transfer learning. *Proc. Int. Conf. Image Process*. ICIP 3713-3717.

Lentz SJ (2017). Seasonal warming of the Middle Atlantic Bight cold pool. *J. Geophy. Res.: Oceans,* 122: 941–954.

Lévy M, Klein P, Treguier A-M (2001). Impact of sub-mesoscale physics on production and subduction of phytoplankton in an oligotrophic regime. *J. Mar. Res.,* 59: 535-565.

Linder CA, Gawarkiewicz G (1998). A climatology of the shelfbreak front in the Middle Atlantic Bight. *J. Geophys. Res*., 103: 18,405–18,423.

Loder J, Shore J, Hannah C, Petrie BD (2001). Decadal-scale hydrographic and circulation variability in the Scotia–Maine region. *Deep-Sea Res. Pt. II*, 48: 3-35.

Lumini A, Nanni L (2019). Deep learning and transfer learning features for plankton classification. *Ecol. Inform*., 51:33-43.

Luo JY, Irisson J-O, Graham B, Guigand C, Sarafraz A, Mader C, Cowen RK (2018). Automated plankton image analysis using convolutional neural networks. *Limnol. Oceanogr. Meth*., 16: 814-827.

MacNeil L, Missan S, Luo J, Trappenberg T, LaRoche J (2021). Plankton classification with high-throughput submersible holographic microscopy and transfer learning. *BMC Ecol.* Evo. 21:123.

Mahadevan A, Archer D (2000). Modeling the impact of fronts and mesoscale circulation on the nutrient supply and biogeochemistry of the upper ocean. *J. Geophys. Res*., 105: 1209-1225.

Marra J, Houghton RW, Garside C (1990). Phytoplankton growth at the shelf-break front in the Middle Atlantic Bight. *J. Mar. Res*., 48: 851–868.

Munk W, Armi L, Fischer K, Zachariasen F (2000). Spirals on the sea. *Proc. R. Soc. Lond. A*, 456:1217-1280

Norrbin MF, Davis CS, Gallager SM (1996). Differences in fine-scale structure and composition of zooplankton between mixed and stratified regions of Georges Bank. *Deep Sea Res. II*, 43: 1905–1924.

Oliver H, Zhang WG, Smith WO, Alatalo P, Chappell PD, Hirzel AJ, and others (2021). Diatom hotspots driven by western boundary current instability. *Geophys. Res. Lett.* 48(11).

Oliver H, Zhang WG, Archibald KM, Hirzel AJ, Smith WO, and others (2022). Ephemeral surface chlorophyll enhancement at the New England shelf break driven by Ekman restratification. *J. Geophys. Res. Oceans* 127(1).

Olson RJ, Sosik HM (2007). A submersible imaging-in-flow instrument to analyze nano- and microplankton: Imaging FlowCytobot. *Limnol. Oceanogr. Methods* 5:195-203.

O'Reilly JE, Bush DA (1984). Phytoplankton primary production on the northwestern Atlantic shelf. *Rapp. P-V. Reun. Cons. Int. Explor. Mer*., 183: 255–268.

Orenstein EC, Beijbom O, Peacock EE, Sosik HM (2015). WHOI-plankton – a large scale fine grained visual recognition benchmark dataset for plankton classification. *CVPR 2015*.

Pei Y, Huang Y, Zou Q, Zhang X, Wang S (2019). Effects of image degradation and degradation removal to CNN-based image classification. I*EEE Transactions on Pattern Analysis and Machine Intelligence* 43(4):1239-1253.

Pickart RS, Torres D, McKee TK, Caruso M, Przystup JE (1999). Diagnosing a meander of the shelf break current in the Middle Atlantic Bight. *J. Geophys. Res.,* 104.

Pickart RS (2000). Bottom boundary layer structure and detachment in the shelfbreak jet of the Middle Atlantic Bight. *J. Phys. Oceanogr*., 30(11): 2668–2686.

Podestá GP, Browder JA, Hoey JJ (1993). Exploring the association between swordfish catch rates and thermal fronts on U.S. longline grounds in the western North Atlantic. *Cont. Shelf Res.,* 13(2-3): 253-277.

Ryan JP, Yoder JA, Cornillon PC (1999a). Enhanced chlorophyll at the shelfbreak of the Mid-Atlantic Bight and Georges Bank during the spring transition. *Limnol. Oceanogr*., 44(1): 1–11.

Ryan JP, Yoder JA, Barth JA, Cornillon PC (1999b). Chlorophyll enhancement and mixing associated with meanders of the shelf break front in the Mid-Atlantic Bight. *J. Geophys. Res.,* 104(C10):23479-23493.

Ryan JP, Yoder JA, Townsend DW (2001). Influence of a Gulf Stream warm-core ring on water mass and chlorophyll distributions along the southern flank of Georges Bank. *Deep-Sea Res. Pt. II,* 48: 159-178.

Saba VS, Hyde KJW, Rebuck ND, Friedland KD, Hare JA, Kahru M, Fogarty MJ (2015). Physical associations to spring phytoplankton biomass interannual variability in the U.S. Northeast Continental Shelf. *J. Geophys. Res. Biogeosci.,* 120: 205–220.

Shchepetkin AF, McWilliams JC (2008). Computational kernel algorithms for fine-scale, multiprocess, long-term oceanic simulations. *Handbook of Numerical Analysis. XIV: Computational Methods for the Atmosphere and the Ocean*, Ciarlet PG, Temam R, Tribbia J (eds.), *Elsevier*, 121–183.

Sherman K, Jaworski NA, Smayda TJ (1996). The Northeast Shelf Ecosystem: Assessment, Sustainability and Management, Blackwell Science, Cambridge, Massachusetts, USA.

Smith WO, McGillicuddy DJ, Olson EB, Kosnyrev V, Peacock EE, Sosik HM (2017). Mesoscale variability in intact and ghost colonies of *Phaeocystis antarctica* in the Ross Sea: distribution and abundance. *J. Mar. Syst*. 166: 97-107.

Smith WO, Zhang WG, Hirzel A, Stanley RM, Meyer MG, and others (2021). A regional, early spring bloom of Phaeocystis pouchetii on the New England continental shelf. *J. Geophys. Res. Oceans* 126(2).

Szegedy C, Vanhoucke V, Io0ffe S, Shlens J, Wojna Z (2016). Rethinking the inception architecture for computer vision. Proc. *IEEE Comput. Soc. Conf. Comput. Vis. Pattern Recogn*. 2818-2826.

Zhang WG, Alatalo P, Crockford T, Hirzel AJ, Meyer MG, and others (in press). Cross-shelf exchange associated with a shelf-water streamer at the Mid-Atlantic Bight shelf edge. *Prog. Oceanogr.*, doi:

Zhang WG, Gawarkiewicz GG, McGillicuddy DJ, Wilkin JL (2011). Climatological Mean Circulation at the New England Shelf Break. *J. Phys. Oceanogr*., 41: 1874–1893.

Zhang WG, Gawarkiewicz G (2015). Length scale of the finite-amplitude meanders of shelfbreak fronts. *J. Phys. Oceanogr*., 45:2598-2620.

Zhang, WG, McGillicuddy DJ, Gawarkiewicz GG (2013), Is biological productivity enhanced at the New England shelfbreak front? *J. Geophys. Res. Oceans*, 118: 517–535